# LABORATORY FOR SOLID STATE PHYSICS

Annual Report 2012

www.solid.phys.ethz.ch/documents
Department of Physics

ETH Zurich

# ANNUAL REPORT
# 2012

Solid State Physics Laboratory (LFKP)
ETH Zurich

## Cover page:

Ultrasensitive scanning force microscope, built in the Degen laboratory. The microscope is capable of detecting minute magnetic forces from nuclear spins in nanomaterials and biomolecules.

This annual report was edited by: Philip Moll

# PREFACE

The Laboratory for Solid State Physics at ETH Zurich is pleased to present the Annual Report for 2012. This report displays our diverse foci in research, which lead to numerous publications in high-ranking journals and presentations at international conferences. The members of the Laboratory are also committed to all aspects of teaching. They strive at conveying the fascination of physics in general and in particular of state-of-the-art solid state physics at all levels. Bachelor and Master level courses were offered for physics students as well as for students of other departments. As recognition for his outstanding achievements in teaching, the Golden Owl - a yearly prize awarded to faculty members of ETH Zurich by the students- -was presented to Leonardo Degiorgi in 2012.

The portfolio of research directions carried out at LFKP covers a rather wide range including the application and development of novel instruments, the synthesis of highest-quality materials and the fabrication of nanoscale quantum devices as summarized below.

The Pescia's group has continued the work on developing a novel electron microscope based on the topographiner (or Near Field Emission) principle. The lateral resolution achieved with this new instrument is comparable to the one known in Scanning Tunneling Microscopy. In addition, the group was able to demonstrate the feasibility of energy analysis in the topographiner mode. The collaboration with the group of Andreas Vaterlaus on time resolved experiments at the FLASH facility in Hamburg continues. Prof. Erbudak, a consultant of the group, has been elected as a member of the Academy of Sciences of Turkey.

The Vaterlaus group has successfully conducted a second round of experiments at the free electron laser FLASH at DESY in Hamburg addressing the dynamics of magnetic systems. During these experiments the dynamics of laser excited electronic states was followed on a femtosecond time scale. In physics education the group pursues a project in formative assessment. Diagnostic tests were developed and tested under real "in class" conditions.

The group of Joël Mesot studied the effects of disorder, frustration and magnetic fields on the properties of spin-chain and spin-ladder systems. High-field $^{31}$P NMR was used to investigate field-induced order (FIO) in the frustrated 2-leg ladder compound $BiCu_2PO_6$. The data and results of DMRG calculations indicate the formation of a soliton lattice in the ordered phase. The phenomenon of dimensional-crossover, typical of spin-chain compounds, was studied by $^{29}$Si NMR in $BaCu_2Si_2O_7$. A local staggered transverse magnetic field (LTSF) causes the 1D characteristics of the Cu spin chains to persist into the low temperature 3D-ordered state. Previously unexplained spin-reorientation transitions are shown to be caused by the LTSF.

In Andrey Zheludev's group the most spectacular result of 2012 was the first measurements of the complete excitation spectrum of a Heisenberg spin ladder in the field-induced Tomonaga-Luttinger spin liquid phase. The unprecedented level of detail revealed spinon deconfinement and incommensurate correlations, in quantitative agreement with theoretical predictions. A second very important achievement was a proof of microscopically coexisting spin glass and long range antiferromagnetic orders in the isotropic crystalline material $PbFe_{0.5}Nb_{0.5}O_3$. This result was obtained by combining neutron diffraction (momentum-resolved) and Mössbauer spectroscopy (local-probe) techniques.

A joint experimental (Raman) and theoretical study on the model charge density wave (CDW) system $ErTe_3$ allowed the Degiorgi group to establish a relation between the selection rules of the electronic light scattering spectra and the enhanced electron-phonon coupling in the vicinity of band degeneracy points. This leads to the conclusion that an enhanced electron-lattice interaction can contribute to or even determine the selection of the ordering vector. This alternative proposal for CDW formation may be of general relevance for driving phase transitions into other broken-symmetry ground states, particularly in multi-band systems such as the iron based superconductors.

The Quantum Device Lab lead by Andreas Wallraff has explored the interaction of microwave photons with Rydberg atoms and semiconductor quantum dots in novel hybrid quantum systems. This work has been performed in collaboration with the groups of Klaus Ensslin and Frederic Merkt (D-CHAB). In research on quantum information processing, based on superconducting qubits, the lab has demonstrated a teleportation protocol, a three-qubit gate for

error correction, geometric phase gates, and novel efficient quantum process characterization tools. They have also created and characterized entanglement between stationary qubits and propagating microwave photons, which will be essential for realizing future microwave quantum communication schemes.

The spin physics group of Christian Degen, established in the summer of 2011, has consolidated its effort in ultrasensitive scanning probe microscopy. The group has grown to 8 lab members and is now supported by an ERC Starting Grant. Two major results could be obtained: The implementation of a quantum spectrum analyzer using an atom-sized spin qubit in diamond, and the successful fabrication of single-crystal-diamond AFM cantilevers with record high quality factors.

The Ensslin group performed scanning gate experiments on quantum point contacts fabricated on high-mobility electron gases grown by the Wegscheider group. The results clearly show edge state formation in the integer quantum Hall regime, as evidenced by other experiments before. In addition edge state behavior also shows up in the fractional quantum Hall regime, which opens a new arena for experimental investigations of these collective phenomena.

One of the highlights of the Wegscheider group was the direct mapping of the formation of a persistent spin helix. This result was obtained in collaboration with the group of Gian Salis, which carried out the time- and spatially resolved Kerr rotation experiments at IBM Rüschlikon. The Advanced Semiconductor Quantum Materials group at ETHZ provided AlGaAs/GaAs samples hosting two-dimensional electron gases, which were designed to fulfill the special criterion of balanced Rashba and Dresselhaus contributions to spin-orbit interaction (SOI).

In high TC superconductor research the Batlogg group observed the transition from slow Abrikosov to fast moving Josephson vortices in SmFeAs(O,F). This transition is hallmarked by a sharp drop in the critical current and accordingly a jump in the flux-flow voltage in a magnetic field precisely aligned along the FeAs layers, indicative of highly mobile vortices. For fields slightly out-of-plane the vortices are completely immobilized as well-pinned Abrikosov segments are introduced when the vortex crosses the FeAs layers. This vortex dynamics could become technologically relevant as superconducting applications will always operate deep in the Josephson regime.

The experimental research at the laboratory of solid state physics and our teaching activities benefit from the excellent infrastructure provided by ETH Zurich and in particular by the physics department. We thank the involved people for their dedication and solid support especially in all technical and administrative matters. Together with the apprentices the LFKP developed under the supervision of Leonardo Degiorgi new experiments for the Wanderzirkus initiative. One of the highlights there is the levitating train model, based on the Meissner effect.

We very gratefully acknowledge the continuous and substantial support by the Schulleitung of ETH Zurich, but also by the Swiss National Science Foundation, the Commission for Technology and Innovation (KTI), the European Research Council, industrial partners and all other sources.

For preparing this Annual Report, we would like to thank Mrs. Christina Egli and Mr. Ph. Moll for editing the report and Mrs. Heidi Hostettler as well as Mrs. Amanda Eisenhut for the graphical design.

In order to follow the mainstream or rather to avoid producing old-fashioned CDs we will simply print a postcard with a QR-Code on it so that last year's report can be easily downloaded.

Zürich, May 2013

Der Vorsteher

Prof. Dr. W. Wegscheider

# Contents

# Chapter 1

# Physics of New Materials

**Head**
Prof. Dr. B. Batlogg

**Academic Staff**
Balthasar Blülle
Jonathan Hanselmann
Thomas Kreiliger
Tobias Morf
Kristin Willa
Dr. Claudiu Falub
Roger Häusermann
Thomas Mathis
Dr. Yasmine Sassa
Tino Zimmerling
Dr. Alfonso Gonzalez
Jakob Kanter
Dr. Philip Moll
PD Dr. Hans von Känel

**Administrative Staff**
Gabriela Strahm

**Technical Staff**
Kurt Mattenberger

## High Pressure Synthesis

**Head**
Dr. Janusz Karpinski

**Academic Staff**
Dr. Sergiy Katrych
Dr. Nikolai Zhigadlo

**Academic Guests**
Dr. Roman Puzniak, Polish Academy of Sciences, Warsaw (Poland)
Dr. Krzysztof Rogacki, Polish Academy of Sciences, Wroclaw (Poland)

## 1.1 Quantum oscillation measurements of micro-structured samples under high pressures

J. Kanter, P. Moll, S. Friedemann, P. Alireza, F. Ronning, E.D. Bauer, B. Batlogg

Electronic transport measurements under high pressures face several experimental challenges due to confined sample space and high forces acting on contacts and leads. As a result, conventional preparation methods are often limited in the number of possible sample contacts and usually do not allow for sample structuring. Hence transport measurements under high pressures were often limited to four terminal measurements with one sample per anvil cell. Nonetheless, as quantum oscillation measurements are a direct probe of electronic interactions and the Fermi Surface, low noise transport measurements under high pressures are a valuable tool in the field of correlated electron physics. The Focused Ion Beam (FIB) technique allows for contacting and micro-structuring of samples. Enabling complex sample shapes and strain resistent contact leads, the FIB technique is a prime tool for preparing electronic transport measurements under high pressures.

We have applied and optimized the FIB technique for use with high pressure anvil cells. In a first experiment we are investigating the pressure dependence of the effective electron masses in $CePt_2In_7$. In this heavy fermion system an unconventional superconducting phase is induced under pressure with a maximal $T_c$ above a quantum critical point (QPC) around 30 kbar. The magnetic fluctuations connected to the quantum critical point are thought to stabilize the superconducting phase, rendering the investigation of the effective electron masses in $CePt_2In_7$ a very interesting candidate for Shubnikov-de Haas measurements under high pressures.

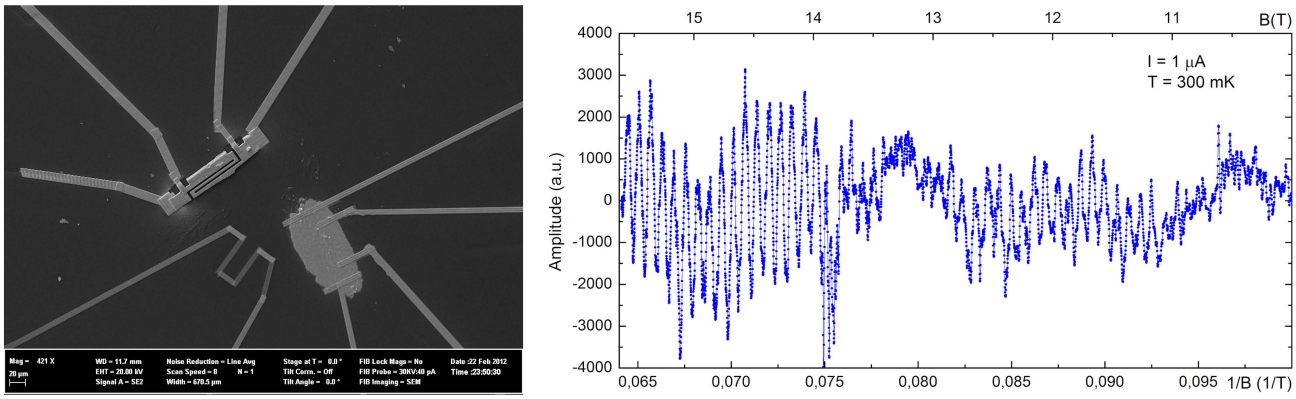


**Figure 1.1:** **Left** FIB-structured and contacted samples. The micro-structuring increases the length over cross section ratio, resulting in high signal to noise ratios, even at low excitaions. **Right** Exemplary measurement data showing quantum oscillations in the resistivity of $CePt_2In_7$.

## 1.2 Critical current oscillations in the hybrid vortex matter of SmFeAs(O,F)

P.J.W. Moll, N.D. Zhigadlo, B. Batlogg

With the discovery of a novel class of high-$T_c$ superconductors such as the iron-pnictides, the two most important questions concern the pairing mechanism mediating Cooper pairing at high temperatures and the materials prospect for future applications, determined by the material parameters $H_{c2}$, $T_c$ and $j_c$, which all reflect on the vortex matter of the system. The observation of disordered vortex lattices and large critical currents $j_c$ in the layered iron-pnictide SmFeAs(O,F) had already shown the material's potential for applications. Thus it is highly desirable to further explore the nature of vortices in these unconventional superconductors and their interaction with the pinning landscape. Given the moderate electronic anisotropy of SmFeAs(O,F) $\gamma = 4 - 6$, one would expect anisotropic scaling theory to fully describe the vortex matter. Yet, we have observed a distinct vortex matter transition upon cooling SmFeAs(O,F) with $T_c \sim 48 - 50K$ below a temperature $T^* \sim 41 - 42K$ in a magnetic field $H$ precisely aligned with the superconducting FeAs layers: Below T* the critical currents drop dramatically and the flux-flow voltage increases accordingly, indicative of highly mobile vortices. We find that $T^*$ coincides with the temperature where the coherence length $\xi_c$ perpendicular to the layers matches half the FeAs-layer spacing. For fields slightly out-of-plane ($> 0.3°$) the vortices are again completely immobilized as they cross the planes and thus are strongly pinned by defects within the FeAs layers. We interpret these unexpected findings as a transition from well-pinned, slow moving Abrikosov vortices at high temperatures to weakly pinned, fast flowing Josephson vortices at low temperatures, indicating the superconducting electrons to be strongly confined to the FeAs layers.

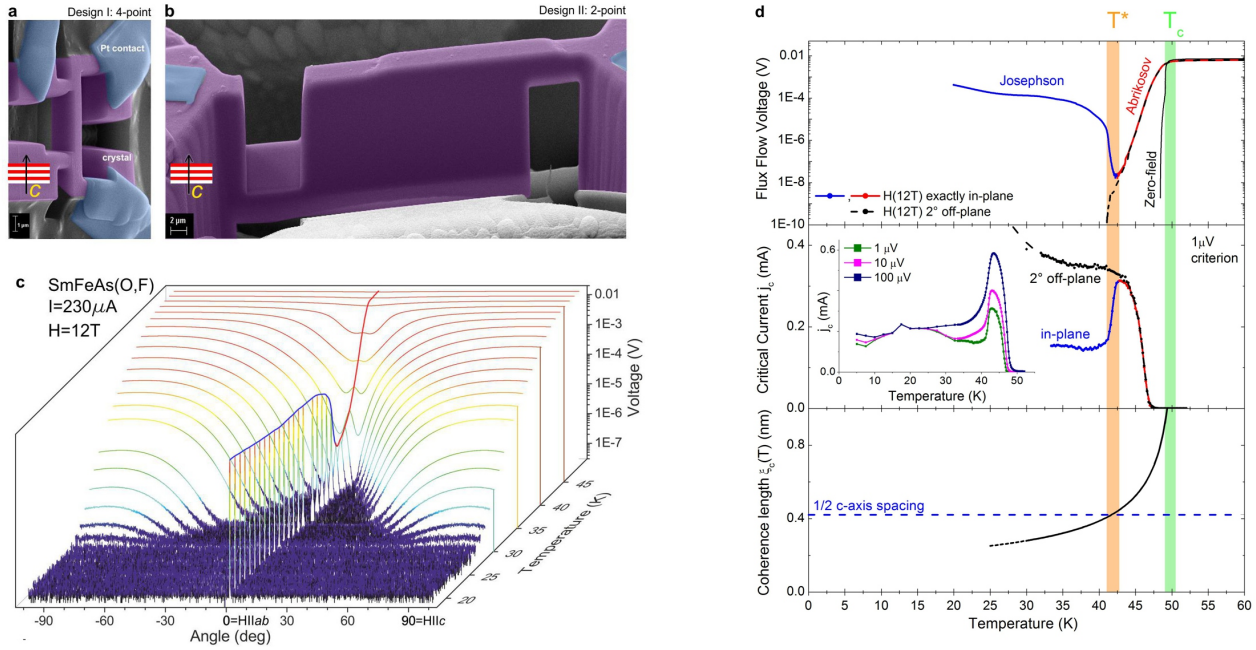


**Figure 1.2:** **a,b** Focused Ion Beam microshaped and contacted single crystals of SmFeAs(O,F) designed for c-axis resistivity measurements. The different two- and four-point geometries used open the possibility to investigate sample size effects. **c** Flux-flow dissipation for varying angles between a magnetic field of fixed strength ($12T$) and the FeAs planes ($0°$) at different fixed temperatures. The main observation is a sharp spike in dissipation for fields well aligned with the FeAs planes, even at temperatures well below $T_c$. The vortex mobility jumps dramatically at $T^*$ and continues to increase upon cooling, indicating Josephson vortex dynamics. **d** Flux Flow voltage and critical currents for field well aligned with the FeAs planes and $2°$ misaligned fields. While the well aligned vortices remain highly mobile at low temperatures, misaligning the field by only $2°$ introduces enough well-pinned pancake vortices to restore Abrikosov behavior. This dramatic change in vortex dynamics is observed at a well-defined temperature $T^*$, which well matches the crossing point of the c-axis coherence length $\xi_c(T)$ with 1/2 of the c-axis unit cell.

## 1.3 From solution processing to single crystal transistors: a quantitative comparison

K. Willa, R. Häusermann, B. Batlogg

To investigate how the charge transport properties vary with the degree of crystalline order, we fabricated single crystal FETs, thermally evaporated and spin-coated thin-film transistors based on the same n-type semiconductor (PDIF-$CN_2$, Polyera Corp.) using various combinations of deposition methods and gate dielectrics (fig. 1.3).
The transfer curves for the PDIF-$CN_2$ single crystals on Cytop reveal excellent transistor performance with a mobility

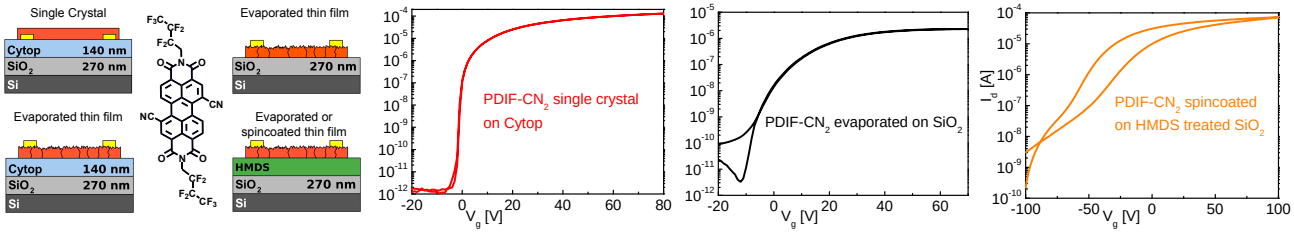


**Figure 1.3:** A representative transfer curve is plotted for the device structures shown on the left. As the same semiconductor PDIF-$CN_2$ is used for all devices, the improvement from the spincoated thin film on the left to the single crystal on the right can be directly associated to the processing conditions.

of up to 6 $cm^2$/Vs, an on/off-ratio exceeding $10^8$ and a subthreshold swing of only 0.45 V/dec. For the evaporated thin film transitor these performance characteristics are reduced, but still, the threshold voltage is close to zero, the on/off-ratio higher than $10^5$ and a mobility around 0.2 $cm^2$/Vs. In the case of the spincoated TFT, the transistor characteristics are barely visible, still, the mobility is nearly as high as for the evaporated ones.

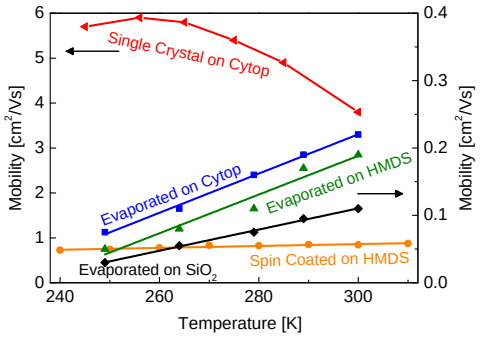


**Figure 1.4:** Temperature dependence of the mobility for all devices.

With all these device configurations the transfer curves where measured at different temperatures. The extracted mobilities at each temperature step are shown in figure 1.4. The single crystal shows an increasing mobility for decreasing temperatures. A sign which is often referred to as "band-like" transport. The mobility for the evaporated TFT's shows a dependence on the gate dielectric used, revealing the importance of the interface between the semiconductor and the dielectric. As often demonstrated before, Cytop again shows the highest performance. Nevertheless, the mobility decreases for all evaporated TFT's with lowering temperature with approximately the same slope. Interestingly the mobility of the spin-coated device stays constant over the measured range.

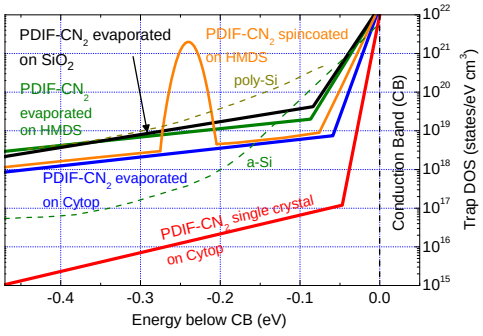


**Figure 1.5:** Density of states for PDIF-$CN_2$

For all devices the DOS was simulated using a computer program developed in this group (figure 1.5). The excellent transistor behaviour of the single crystal on Cytop is also pointed out by the exceptional low trap DOS, as low as for the best p-type materials. The decrease in performance from the single crystal to the evaporated thin films is reflected in the increased trap DOS. Again, the role of the dielectric can be seen in the slightly varying trap DOS among the evaporated films showing the lowest trap DOS for the Cytop dielectric. The spincoated thin film has a surprisingly low trap DOS , but has additional discrete trap states centered around 0.24 eV below the conduction band. These trap states dominate the whole transfer characteristic, leading to the broad turn-on region.
We conclude from this microscopic study that PDIF-$CN_2$ is highly promising for practical applications thanks to its wide choice of processing methods and its excellent intrinsic electronic properties reflected in the exceptionally low trap DOS as low as in the best p-type single crystal FETs.

## 1.4 Scotch taped pentacene TFTs: application in airgap structures

T. Morf, R. Häusermann, A. Pustogow and B. Batlogg

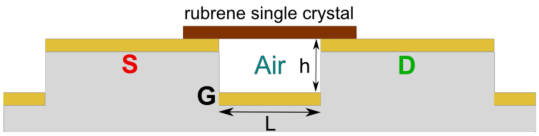


**Figure 1.6:** Airgap FET structure.

Recent research with organic field effect transistors (OFET) showed that mobile charges get trapped in the gate dielectric, such as $SiO_2$, when a gate voltage is applied over a long period. Therefore, OFETs are unstable under long term operation, which is a challenge for commercial applications.
To investigate if charges can also be trapped for longer periods of time in the organic film itself, an air-gap structure was used, where vacuum acts as the dielectric itself. Thus, any signs of charge immobilization would indicate trapping in the organic semiconductor. Therefore, OFETs were constructed out of a thin pentacene film and an air gap. Pentacene thin-films have been evaporated on a $SiO_2$/Cytop substrate and then the film has been removed using a Scotch tape and transferred to another FET structure.

We could show that the Scotch tape transfer method works when the pentacene films have been moved onto another $SiO_2$/Cytop substrate, but the threshold voltage was still too high to be used in airgap structures.By using Rubrene single crystals as the organic semiconductor, it could be shown that the air gap structures are in principle well suited for building OFETs. Additionally, small hysteresis was observed in the transfer characteristics, which indicates that charges get trapped in the rubrene single crystal. Hence, grain boundaries cannot be taken into account and another mechanism of charge immobilization has to be considered.

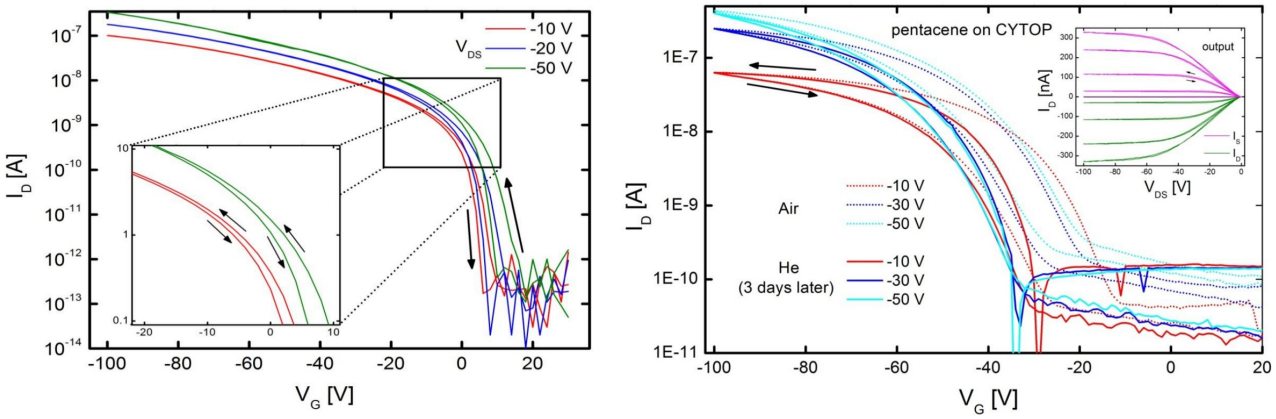


**Figure 1.7:** Left: Transfer characteristics of a rubrene single crystal on top of the air gap structure. The black arrows indicate gate voltage sweep direction.
Right: Transfer characteristics of a pentacene film which has been Scotch tape transferred onto a $SiO_2$/Cytop substrate. The inset shows the output characteristics performed at gate voltages of -10 V to -50 V.

## 1.5 Measuring the charge carrier mobilities in organic solar cells

R. Häusermann, S. Chauvin and B. Batlogg

A field-effect transistor (FET) structure is normally used to determine charge carrier mobilities in organic semiconductors. This comes with the disadvantage of a different morphology, different amount of trap states and a totally different charge carrier density in the FET compared to the device one is interested in. Therefore various methods have been used to measure the mobility directly in an organic light emitting diode or organic solar cell. Here we investigated the charge transport in an organic solar cell. The transient behaviour of organic solar cells, made of a blend of P3HT:PCBM, was studied. The solar cells have been provided by the Laboratory for Functional Polymers at

the EMPA. A set-up using ultra-fast LEDs made it possible to measure the photogenerated current and voltage when the light is turned on and off. The turn-on and turn-off behaviour were observed with a time resolution of 10 ns, and over several orders of magnitude in the measured intensity. Some additional parameters were also varied, such as the voltage applied on the solar cell, or the applied light intensity. For each of these measurements, the charge carrier mobilities was found to be around $\mu_{electron} = 4 \times 10^{-6} cm^2/Vs$ for electrons and $\mu_{hole} = 1 \times 10^{-7} cm^2/Vs$ for holes.

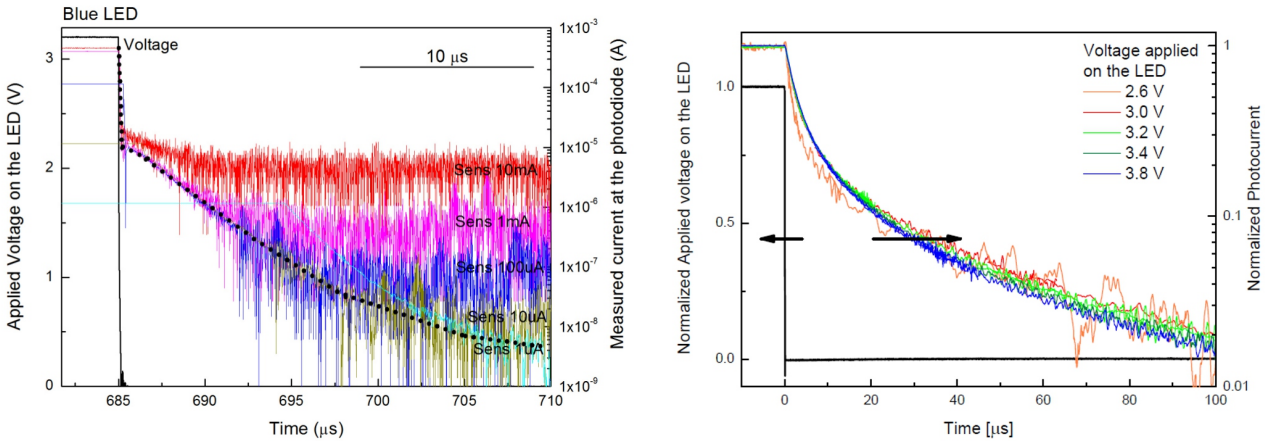


**Figure 1.8:** Left: Semi-logarithmic plot of the raw data of the turn-off behavior of a fast photodiode (Osram SFH 203 P). The transient photocurrent is measured over 5 orders of magnitude. The current has been measured over 25 $\mu$s in 10 ns steps. The influence of the different settings of the sensitivity is shown using different colors. As a guide for the eye, transient photocurrent is shown as the dashed, black line. Right: Semi-logarithmic plot of the turn-off behavior of the P3HT:PCBM solar cell under different illumination intensities. When normalized, the transient photocurrent is independent of the illumination intensity.

## 1.6 P-type transport in the intrinsic n-type material N1100 using $V_2O_5$ as injection layer

R. Häusermann, S. Chauvin and B. Batlogg

N-type organic materials normally have a LUMO-level around 5 eV to stabilize the molecule against oxidation and to facilitate injection from Gold or similar electrode materials. The material called N1100 is normally used with gold electrodes, to inject electrons into the semiconductor. This material has been shown to have high mobilities (up to 6 $cm^2/Vs$ for the saturated mobility) as well as a fast turn-on.
We have used a modified contact to be able to inject holes into N1100. It has been shown that $V_2O_5$ is able to inject holes into low lying HOMO levels . Here we have been able to inject holes into a HOMO level which has an energy of -6.6 eV. With this structure we found the electron mobility to be to $\mu_{sat} = 4.10^{-2}\, cm^2/Vs$. The hole mobility was as high as $\mu_{sat} = 1.10^{-3}\, cm^2/Vs$. For both charge carriers a injection barrier was found in the measured IV-curves. This is the first time that hole injection into an organic molecule with a HOMO level below 6 eV is reported in the literature.

## 1.7 The density of trap states in n- and p-type semiconductors

R. Häusermann, K. Willa, B. Blülle, T. Zimmerling, P. Kerpen, A. Facchetti, Z. Chen, B. Batlogg

It is known that a reduced device performance has its origin in localized charges which have a lower probability of hopping to a neighboring molecule. This localization occurs at so called trap states which are energetically situated

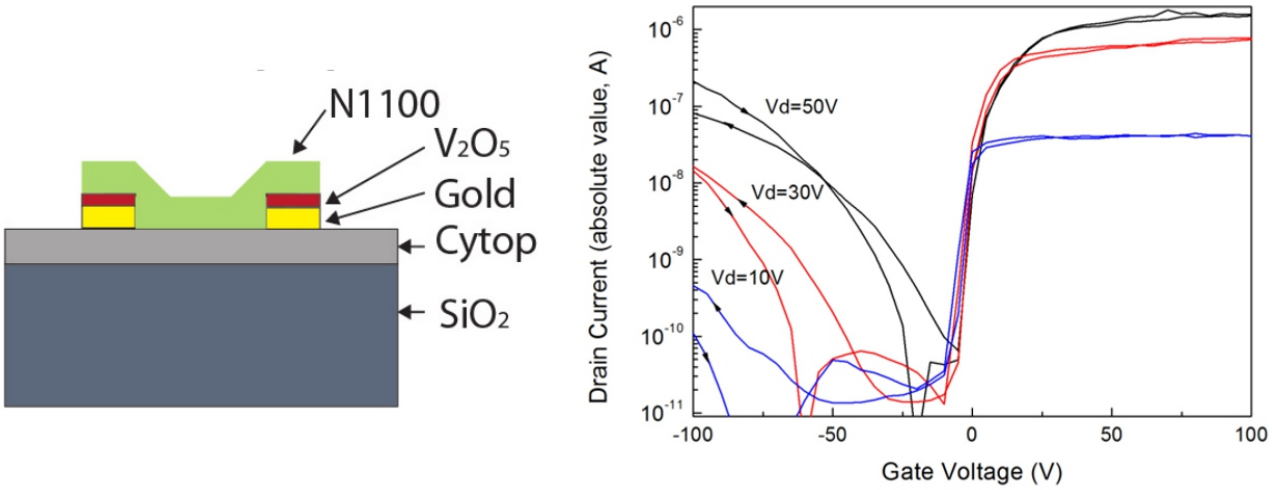


**Figure 1.9:** Left: The transistor structure used to inject charge charge carriers into the HOMO level. Right: Transfer curve, showing ambipolar transport, i.e. conduction at negative as well as positive gate voltage.

in the band-gap between the highest unoccupied molecular orbital (HOMO) and the lowest unoccupied molecular orbital (LUMO).

There has been intense research to understand and quantify the influence trap states on charge transport. Especially p-type materials have been investigated. Still, the various origins of trap states which then lead to charge localization are widely discussed. Therefore knowing as much as possible about the spectral distribution of the density of charge trap states (trap DOS) is essential to widen our knowledge in the field of organic semiconductors and to finally understand their properties.

We compared the transfer curves for various FETs (Fig. 1.10) as a starting point to analyze the trap DOS. This analysis encompasses numerous organic as well as inorganic p- and n-type semiconductors under various processing conditions and therefore a wide range of purity and crystallinity. In conclusion we have seen, that organic materials can have a much lower trap DOS compared to inorganic thin-films and surprisingly the trap DOS for printed organic polymers can be as low as for organic single-crystals.

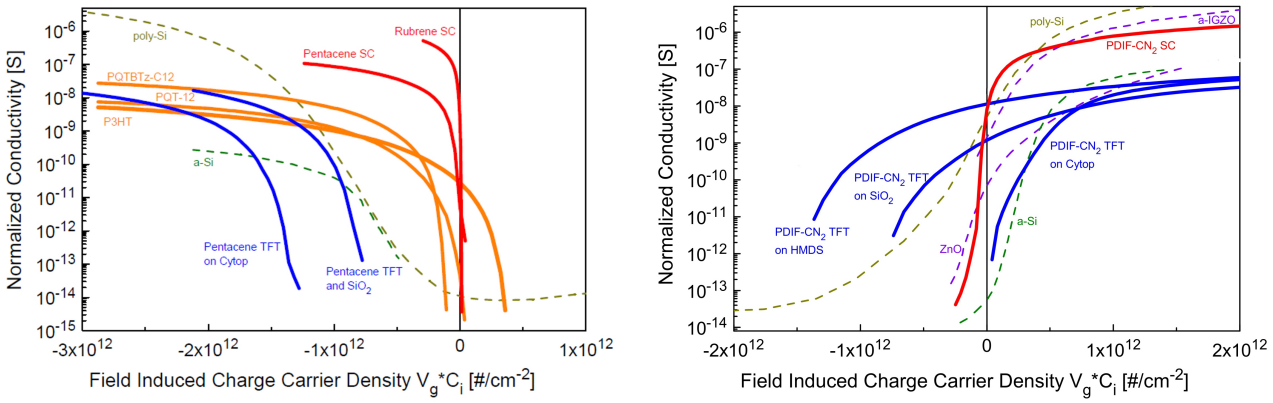


**Figure 1.10:** Transfer curves for the various materials investigated in this study. Left: p-type, right: n-type. The broader the turn on, the more traps are present. The higher the maximum current, the higher the mobility. The three single crystal FETs (Pentacene, Rubrene and PDIF-$CN_2$ shown in red) have the lowest trap density, whereas 2 of the 6 inorganic FETs (dashed lines) have a high mobility, but they all have a broader turn on due to a high trap density.

## 1.8 Atomic layer deposition of $HfO_2$ on organic single crystals as a gate dielectric for FETs

S. Ono, R. Häusermann, B. Batlogg

Normally $SiO_2$ is used as a gate dielectric for organic FETs. To tune the properties of the organic/dielectric interface various methods are used: spin-coating a passivation layer, growing a self assembled monolayer, evaporating an additional dielectric, etc. This nevertheless leaves us with a low capacitance dielectric. To increase charge carrier density in the conduction channel one has to use a different dielectric material.
We have grown $HfO_2$ directly on top of a Rubrene single crystal. This has the additional advantage to insulate the organic material from environmental influences. A careful study of the transport properties shows that the interface between the organic semiconductor and the $HfO_2$ is very good, resulting in only a small gate bias stress effect. Mobilities between 1 and 2 $cm^2$/Vs have been obtained which is an additional hint for the good interface.

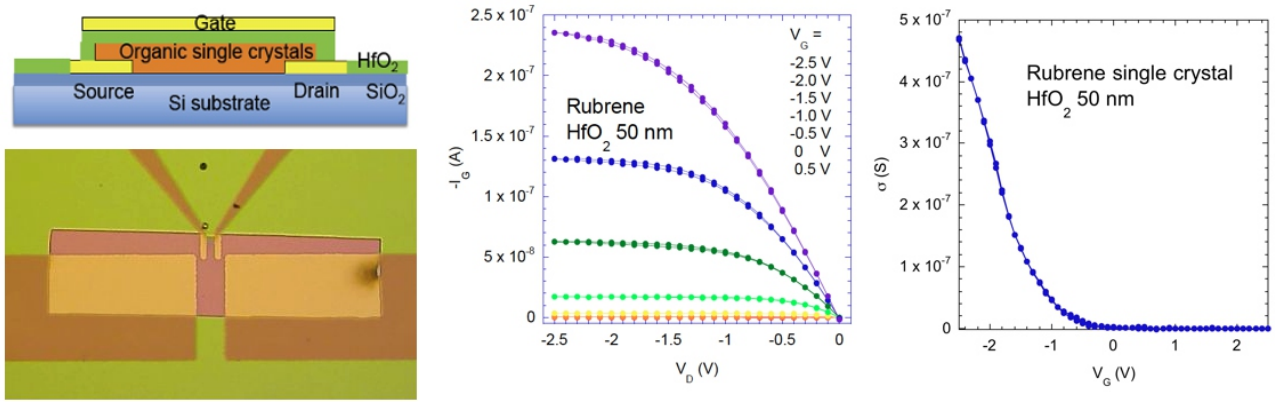


**Figure 1.11:** Left: Schematic cross section of the field-effect transistor and image of an actual device. Middle and right: Transfer and output curves for an $HfO_2$ gated single crystal FET. This shows the good transistor performance using this gate dielectric.

## 1.9 Using short voltage pulses to measure the device impedance

R. Häusermann, B. Batlogg

Measuring the frequency dependent capacitance of semiconducting devices is normally done with an impedance meter. This takes several minutes during which the device under test might change, e.g. due to slow charge trapping. Therefore it is often not possible to measure frequency dependent properties under non-steady-state conditions. Here we have used a Agilent B1530A Parameter analyzer which includes a waveform generator/fast measurement unit to measure the impedance much faster.
With this setup we applied a voltage pulse composed of several sinusoidal signals to a capacitance structure and measured the current response of the device under test. After careful tuning the input signal (pulse amplitude and width, frequency range, integration times) and filtering of the output it has been possible to measure the impedance response of our device from about 1 Hz up to about 1 MHz and up to $10^9$ Ω. The important aspect is that the device has been stressed for only a very short time during these measurement (less than $10^{-4} - 0.1$s) and therefore it is possible to measure non-steady state properties of the device under test.
In this fast measurement more noise is expected than in a traditional slow frequency sweep with long integration times. Nevertheless it is easily possible to see a small difference of about $10^{-11}$ F between two measured samples.

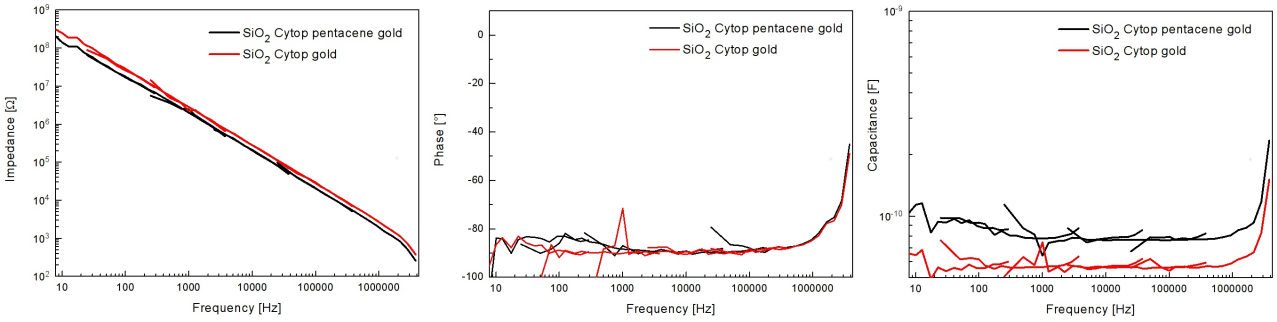


**Figure 1.12:** Left: Impedance measurement. Middle: Measured Phase between input and output signal. Right: Calculated capacitance of the two devices. Every curve is a compilation from 4 short measurements with a specific frequency window. At the edge of the respective window the measurements are more noisy. The black curve has an additional thin organic layer (30 nm) sandwiched between the electrode and the insulator. There is a clear difference between these two measured samples.

## 1.10 Transistors using new TBT oligomeres with various $\pi$-bridge spacers

T.Mathis

Environmental stability and high charge mobility are among the most desirable properties of organic semiconductor materials. Hence research into more stable compounds has been intense. In this research project thienobenzothiophene (TBT) building blocks with different $\pi$-bridge spacers are used to fabricate more stable oligomeres with equal or better electrical properties than pentacene. TBT oligomeres are promising because they have a more efficient orbital overlap and thus improved electrical properties. The molecular packaging in sulfur rich based TBT with the combination of intermolecular multiple sulfur - sulfur, sulfur - carbon and carbon hydrogen - $\pi$ interactions could lead to higher mobilities. Recently trans-TBT oligomeres have shown mobilities similar to pentacene. As sulfur is considered a factor in the molecular orbital overlap formation, its position may have also a key influence on the electrical properties of the solid. Therefore in our new cis-TBT molecules the sulfur was repositioned. These TBT cores with different $\pi$-bridge spacers such as ethylene, benzene and fluorobenzene, were studied. For electrical characterization organic thin film field effect transistors (OFET) were fabricated on various substrate surfaces: $SiO_2$ and $Al_2O_3$ treated with OTS, and Cytop. The OFET performance was optimized by varying the substrate temperature during deposition. The relationship between the film morphology imaged by AFM, including grain size, and the electrical performance has been studied as well. Mobilities up to 2 $cm^2$/Vs are measured for devices made of the benzene-bridged compound deposited on untreated $Al_2O_3$. The devices are kept in He atmosphere for long-term stability studies and no degradation is found after 2 month. Together with the good mobility, this makes the materials promising for further exploration.

## 1.11 Three- dimensional electronic structure of $Na_{0.85}CoO_2$

Y. Sassa, J. Kanter, K. Mattenberger and B. Batlogg in collaboration with M. Månsson, J. Chang (Laboratory for Quantum Magnetism, EPF Lausanne), B. Wojek, O. Tjernberg (Material Physics, KTH, Sweden)

Much attention has been paid on the sodium cobalt oxide $Na_xCoO_2$ system as a material of fundamental scientific interest. By increasing the Na content $x$, which represents the electron doping level in this system, different phases with exotic physical properties emerge, ranging from a 2D superconductor by intercalation of water molecules to a 3D spin density waves (SDW) at higher doping. To understand the two- to three-dimensional crossover of the electronic structure between the different phases, considerable angle-resolved photoelectron spectroscopy (ARPES) studies were performed. However, most of these investigations were focused on the 2D electronic states leaving the 3D SDW electronic structure elusive. To determine the 3D electronic structure we performed a careful study of the $k_z$-dispersion of the SDW phase of $Na_{0.85}CoO_2$ by soft x-ray ARPES. Photoemission experiment in the soft x-ray

range brings a number of advantages such as free-electron final state, simplified matrix elements and increased of the photoelectron escape depth. The latter, along with the enhancement of bulk sensitivity, improves the resolution of the perpendicular momentum $k_z$ and thus, permits reliable investigations of the 3D electronic structure. Figure 1 (a) shows the plot of ARPES intensity at the Fermi level $E_F$ as a function of in-plane wave vectors $k_x$ and $k_y$ measured with 50 eV photons at T = 10 K. The filled circles are extracted from Lorenztian fits of the momentum distribution curves (MDC) at different momenta. A clear single large $a_{1g}$ hole-like Fermi surface centered at the $\Gamma$(A) point is observed confirming previous ARPES report. Figure 1 (b) displays the Fermi surface of $Na_{0.85}CoO_2$ along the $k_z$ direction measured along the $\Gamma$ point with variable photons energies at T = 10 K. A very strong dispersive feature is clearly visible indicating a strong inter-layer coupling between the $CoO_2$ layers at this sodium doping. In addition, at specific $k_z$ a small pocket-like feature was detected. Our high-energy data shed new light on features found in the low-energy electronic excitations spectra of this complex compound.

## 1.12 Improved growth of Ln1111 crystals from NaAs/KAs Flux

N.D. Zhigadlo, P.J.W. Moll, J. Karpinski and B. Batlogg in collaboration with S. Weyeneth, S. Katrych, K. Rogacki, S. Bosma and R. Puzniak

Further progress in exploring the physical properties of Fe-based superconductors and understanding the nature of superconductivity depends crucially on the availability of sufficiently large single crystals of high quality. We have adopted a high-pressure and high-temperature technique and succeeded in the growth of $Ln1111$ crystals using NaCl/KCl as a flux. However, even at optimal conditions, the growth rate is extremely low, and only crystals with linear sizes up to 300 $\mu$m are reproducibly grown. Thus, to make single crystals of larger sizes, further improvements of the growth conditions are required.

We have tested NaAs and KAs fluxes, expecting that their low melting temperature and high solubility of oxygen allow stable synthesis of large $Ln1111$ single crystals. After systematic investigation of the parameters controlling the growth crystals we conclude that the application of NaAs/KAs fluxes is at least three times more efficient in obtaining bigger crystals (Fig. 1.13), but it makes phase formation and doping control more complicated.

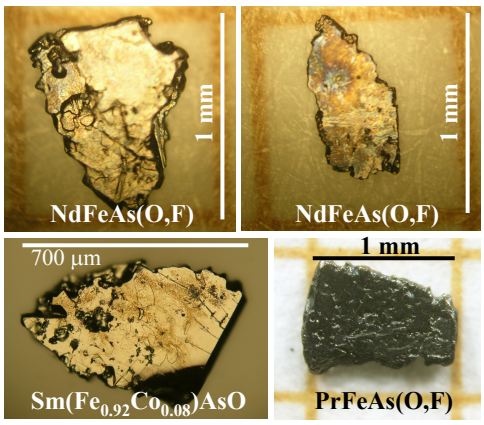


**Figure 1.13:** $Ln1111$ single crystals

From magnetization measurements, we estimate the temperature dependence and anisotropy of the upper critical field and the critical current density of underdoped $PrFeAsO_{0.7}F_{0.3}$ crystals with $T_c \approx 25$ K. Contrasting behavior of optimally doped high-$T_c$ Sm1111 and underdoped low-$T_c$ Pr1111 crystals implies the dependence of $j_c$ on $T_c$ and on the doping level; the more dopants we added, the higher $T_c$ and also the stronger the pinning. From transport and magnetic measurements performed on the $SmFe_{0.92}Co_{0.08}AsO$ crystal with a $T_c = 16.3$ K we estimate the critical fields and their anisotropy and find these superconducting properties to be quite comparable to the ones in $SmFeAsO_{1-x}F_x$ with a much higher $T_c \approx 50$ K. The magnetically measured critical current densities are as high as $10^9$ A/m$^2$ at 2 K up to 7 T, with indication of the usual fishtail effect (Fig. 1.14). The upper critical field estimated from resistivity measurements is anisotropic with slopes of $-8.7$ T/K ($H \parallel ab$-plane) and $-1.7$ T/K ($H \parallel c$-axis). This anisotropy ($\sim 5$) is similar to that in other $Ln1111$ crystals with various higher $T_c$'s (Fig. 1.14).

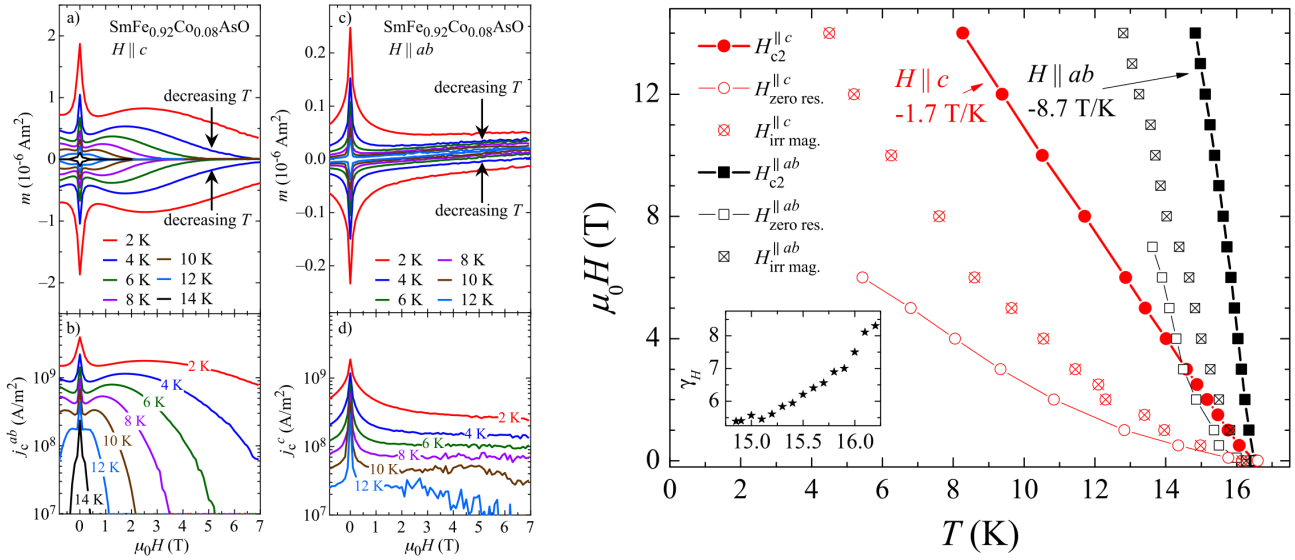


**Figure 1.14:** Left: $j_c^c$ and $j_c^{ab}$ in $SmFe_{0.92}Co_{0.08}AsO$. Right: Phase diagram obtained from magnetization and resistivity measurements of $SmFe_{0.92}Co_{0.08}AsO$ single crystals.

## 1.13 Perfect Ge crystals epitaxially grown on Si substrates

C.V. Falub, T. Kreiliger, A.G. Taboada and H. von Känel in collaboration with M. Meduna (Masaryk University, Brno, Czech Republic), F. Isa, D. Chrastina (L-NESS, Politecnico di Milano, Italy)

Extending the silicon technology to other semiconducting materials with optical and electrical properties beyond those of Si is a long-standing goal of microelectronics. In practice this means growing epitaxial semiconductor layers, often with greatly differing lattice parameters and thermal expansion coefficients. Relaxing misfit and thermal strains may, however, cause excessive dislocation formation, substrate bowing and layer cracking, highly detrimental to subsequent device processing. Recently, we have demonstrated that fast epitaxial growth on substrates deeply-patterned at micron may pave the way for the hetero-epitaxial growth of mismatched structures of any vertical scale onto any substrate [1].

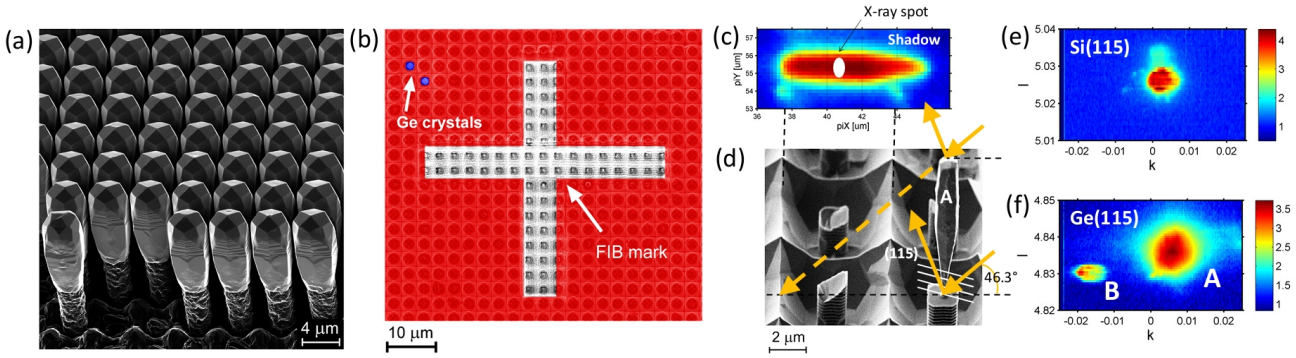


**Figure 1.15:** Nanodiffraction on three-dimensional Ge crystals: (a) SEM micrograph in perspective view of 8-$\mu$m tall Ge crystals grown on patterned Si wafers. (b) Isolated Ge crystals (in blue) are produced by etching in $H_2O_2$ solution and removal of neighboring Ge crystals using micromanipulators in-situ SEM. A reference mark (white cross) in the vicinity of the isolated Ge crystals was written by focused ion beam (FIB) so that these crystals could be located using the optical microscope attached to the diffractometer stage. (c) Total intensity collected from the isolated Ge crystal in (d) around the Ge(115) peak for all incidence angles. (d) SEM micrograph in perspective view of 8-$\mu$m tall, isolated Ge crystal. The crystal was etched in $H_2O_2$ solution. The scattering geometry for (115) reflection is indicated. (e,f) (Qy,Qz) projections of the three-dimensional reciprocal space maps (RSM's) measured around the Si(115) and Ge(115) Bragg reflections. The position of the X-ray spot is indicated in (c). Peaks (A) and (B) correspond to the defected Ge material in the trenches and the perfect Ge crystal, respectively.

By using an X-ray beam, focused to a spot a few hundred nanometers in size, we studied strain and perfection of three-

dimensional epitaxial Ge crystals on patterned Si substrates (4.2% lattice mismatch and 120% thermal mismatch at room temperature). We showed that in the first few microns the crystal planes are bent as a result of elastic relaxation of the thermal strain which develops during cooling from the growth temperature. The strain caused by the large mismatch of the lattice parameters between Si and Ge is on the other hand released by dislocations at the Ge/Si interface, and these cause the crystals to become slightly tilted with respect to one another. Most importantly, after reaching sufficient height, the Ge crystals become indistinguishable from perfect, defect-free single crystals. In short, we have replaced defective continuous heterolayers by perfect crystals with individual tilts. We consider the example studied here as a model system for heterolayers from highly mismatched materials, unaffected by the usual problems of thermal cracks, wafer bowing and crystal defects.

[1] C.V. Falub, H. von Känel *et al.*, Science, **335**, 1330 (2012)

## 1.14 Towards Ge X-ray detector monolithically integrated on Si CMOS

T. Kreiliger, A.G. Taboada, C.V. Falub and H. von Känel in collaboration with F. Isa, G. Isella (L-NESS, Politecnico di Milano, Italy)

Spatial resolution, sensitivity and costs of X-ray imaging detectors would greatly benefit from monolithic integration of an efficient absorber onto Si-CMOS readout circuits, rather than using complex bump-bonding techniques. We have recently shown a novel method to grow a crack- and defect-free crystalline germanium absorber onto a silicon substrate despite the large lattice (4.2 %) and thermal expansion (120 %) mismatches of the two materials involved [1]. We use Si substrates which are deeply patterned at a micron scale in the form of “pillars”, where the base widths range from 2 to 15 $\mu$m. The subsequent epitaxial deposition of Ge in a unique ”low-energy plasma-enhanced CVD” reactor leads then to arrays of individual, closely spaced Ge crystals up to dozens of microns in height.

We performed electrical characterization of hetero-junction diodes formed by these p-Ge crystals and the n-Si substrate. Our structures feature a very high surface-to-volume ratio compared to regular, film-based Si-Ge diodes. Depending on the growth parameters, the Ge crystals exhibit various top surface morphologies, which can, in the case of fully pyramidal shape, drastically reduce their defect density.

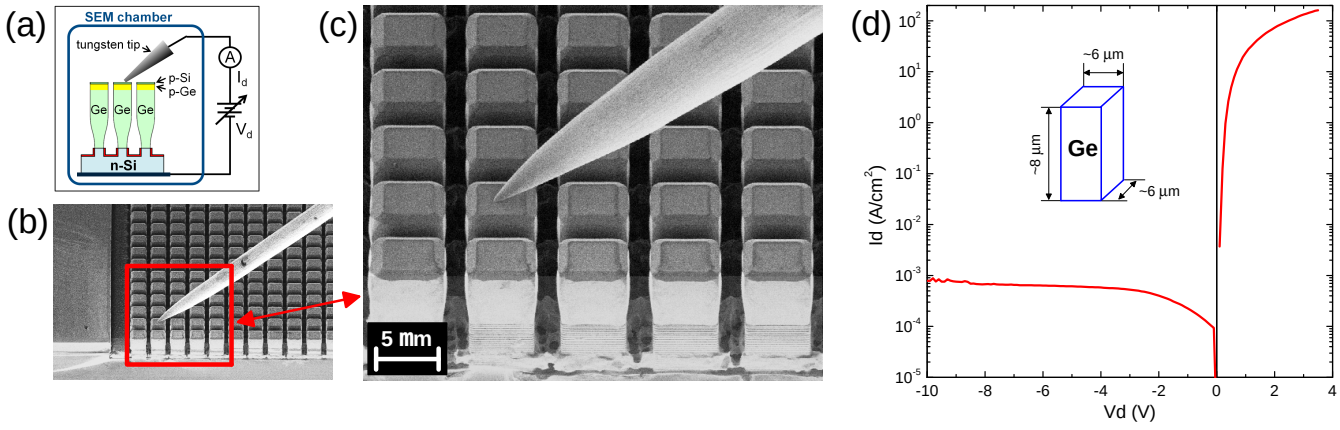


**Figure 1.16:** In-situ SEM conductivity experiments: (a) Schematics of the electric circuit; (b,c) Perspective SEM views of an array of 8 $\mu$m tall Ge towers where a tungsten needle contacts one of the Ge crystals; (d) Typical I-V characteristics of a single 8 $\mu$m tall Ge tower grown onto a deeply patterned n-Si substrate.

The individual Ge crystals were electrically contacted by means of conductive micro-manipulators operating inside an SEM. The effect of Si pillar sidewall passivation onto the diode characteristics was investigated. To prevent surface leakage currents through the sidewalls, wet chemical etching techniques were optimized to remove the defected Ge material in the substrate trenches. Our micron-sized diodes exhibit reverse dark-currents below 1 mA/cm$^2$ at -10 V, which compare favourably with existing Si-Ge diodes and are promising for the development of a novel X-ray detector.

[1] C.V. Falub, H. von Känel *et al*., Science, **335**, 1330 (2012)

## 1.15 GaAs pyramids integrated on patterned Si substrates by MOVPE

A.G. Taboada, C.V. Falub, T. Kreiliger, E. Gini, E. Müller, H. von Känel in collaboration with: F. Isa, G. Isella (L-NESS, Politecnico di Milano, Italy), M. Richter, E. Uccelli, J. Fompeyrine (IBM Reserach Lab. ZÃ$\frac{1}{4}$rich) P. Niedermann, A. Neels, A. Dommann (Centre Suisse d'Electronique et Microtechnique, Switzerland)

The next generation of ultrafast optoelectronic devices may depend on the successful integration of optical and electrical functionalities characteristic of III-V compounds and Si, respectively. Despite the unquestionable advantages of such a system, some well-known challenges need to be met in order to monolithically integrate GaAs on Si substrates, such as: lattice mismatch (4.1 %); thermal expansion coefficient mismatch ($\sim$ 63 %) and anti-phase domain formation.

In order to solve those issues, our approach involves the use of patterned intermediate buffer layers. The basic idea of this method is to grow epitaxial layers in between the GaAs and the Si substrate, consisting of materials with lattice parameters and thermal expansion coefficients in between those of GaAs and Si. The GaAs/Ge/Si structure is the most convenient due to similarities between structural properties of GaAs and Ge, e.g., very small lattice mismatch ($\sim$0.07 %) and comparable thermal expansion coefficients ($\sim$15 %). A recently developed method to grow strain-free high-quality epitaxial Ge towers on patterned Si substrates was identified as a promising solution for GaAs integration on Si [1].

GaAs deposition on Ge/Si towers leads to the formation of GaAs truncated pyramids composed of four (111) lateral facets and a top (001) facet. The differential growth rate in the [001] and [111] directions causes pyramidal shaped crystals. The epitaxial quality of GaAs/Ge/Si grown by MOVPE has been confirmed by X-Ray diffraction (XRD) structural characterization, both for planar and patterned substrates. The analysis of these structures by high-resolution XRD and photoluminescence revealed that the full GaAs pyramids are strain-free despite the large lattice and thermal mismatch with the Si substrate. GaAs pyramids provide similar optical response as GaAs grown on a GaAs substrate.

[1] C.V. Falub, H. von Känel *et al*., Science, **335**, 1330 (2012)

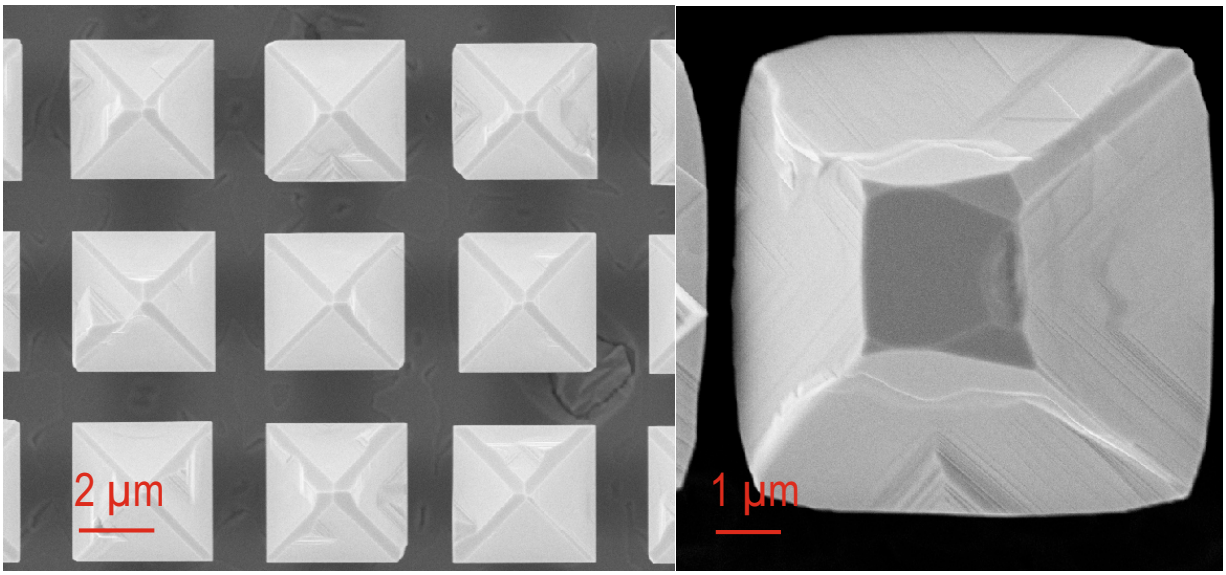


**Figure 1.17: Left:** SEM top view micrograph of 2 $\mu$m tall full GaAs pyramids epitaxially grown on 2x2 $\mu$m$^2$ Ge/Si towers at 680 °C. Right: Detail of a GaAs truncated pyramid grown on a 5x5 $\mu$m$^2$ Ge/Si tower.

# Chapter 2

# Physics of Semiconductor Nanostructures

(http://www.nanophys.ethz.ch)

**Head**
Prof. Dr. K. Ensslin
Prof. Dr. T. Ihn

**Academic Staff**

| | | |
|---|---|---|
| S. Baer | Dr. C. Barraud | Dr. J. Basset |
| D. Bischoff | S. Dröscher | T. Frey |
| T. Choi | S. Hellmüller | A. Jacobsen |
| Dr. A. Kozikov | T. Krähenmann | F. Nichele |
| Dr. A. Pal | N. Pascher | Dr. C. Rössler |
| P. Simonet | A. Varlet | |

**Master Students**

| | | |
|---|---|---|
| Christian Lehner | Pirmin Weigele | Susanne Müller |
| Thomas Hasler | Achille Capelli | Tobias Krähenmann |
| Michael Kopp | | |

**Technical Staff**

| | | |
|---|---|---|
| C. Barengo | P. Studerus | P. Märki |

**Administrative Staff**

| | |
|---|---|
| C. Vinzens | C. Egli |

**Academic Guests**
Sayanti Samaddar, Institut Neel, CNRS, Grenoble, France, (January 15 - February 15, 2012)
Luca Pietrobon, San Sebastian, Spain, (May 2012)

**NCCR QSIT**

| | | |
|---|---|---|
| Dr. I. Blatter | S. Künzel | Dr. J. Rössler |

## 2.1 Irreversibility on the Level of Single-Electron Tunneling

B. Küng, C. Rössler, M. Beck, T. Ihn, and K. Ensslin, in collaboration with M. Marthaler, and D.S. Golubev, Karlsruhe Institute of Technology, Germany and Y. Utsumi, Mie University, Japan

The second law of thermodynamics states that a macroscopic system out of thermal equilibrium will irreversibly move toward equilibrium driven by a steady increase of its entropy. This macroscopic irreversibility occurs despite the time-reversal symmetry of the underlying microscopic equations of motion. Also, a microscopic system will undergo an irreversible evolution on a long time scale, but, over a sufficiently short observation time both entropy-producing trajectories as well as their time-reversed entropy-consuming counterparts occur. It is only because of the statistics of these occurrences that a long-term irreversible evolution is established. This phenomenon is described by the fluctuation theorem.

As a step toward the direct test in the quantum regime, we verify the fluctuation theorem in single-electron tunneling at low temperatures, although our experiment is carried out in the regime of classical charge counting. We employ real-time detection of single-electron charging in quantum dots (QDs). Monitoring the charge state of two QDs that are coupled both in series and to source and drain electrodes (double quantum dot [DQD]) allows us to measure the direction-resolved charge flow through this device and consequently the current probability distribution.

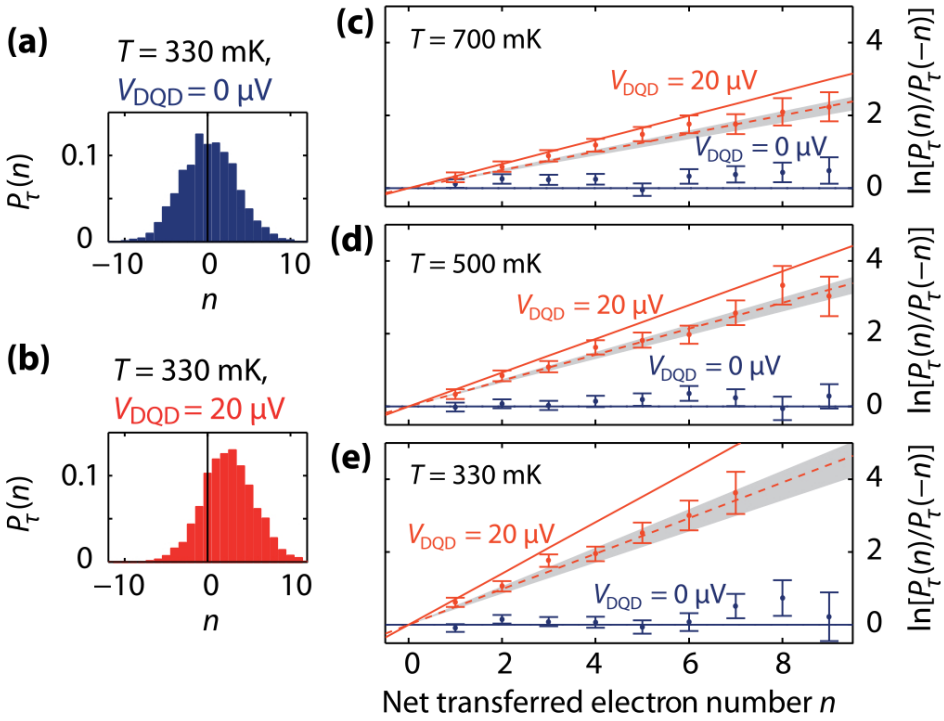


**Figure 2.1:** (a), (b): Experimental probability distribution for the net electron number n transferred through the DQD during time 2 s for two different quantum dot source-drain voltages $V_{DQD}$. (c), (d), and (e): Comparison of experimental data with theory for three different bath temperatures. The data points describe the probability ratio of forward (+n, entropy-producing) and backward (-n, entropy-consuming) processes for a given n. The solid lines mark the expected exponential behavior for the two source-drain voltages 0 V (dark blue, horizontal) and 20 $\mu V$ (red, inclined). If the finite bandwidth of the detector is taken into account (dashed lines), experiment and theory agree within the statistical uncertainty of the data.

Figure 2.1 (a) shows an example of a distribution measured at an electron-bath temperature of 330 mK and with 0V applied bias voltage. It is based on the counting analysis of 3000 time segments, each with length 2 s. The distribution is symmetric about n=0, i.e., there is no net charge flow in equilibrium, as expected. The amount of charge flow at zero bias (compared to the charge flow at finite DQD bias) is a sensitive measure for the strength of residual QPC backaction. Because of left-right asymmetries in the double quantum dot, such as a nonzero level detuning, detector backaction generically leads to nonequilibrium charge flow in a ratchet-type effect. When the bias is increased to 20

$\mu$V, the distribution shifts toward positive n, as shown in Fig. 2.1 (b), and, on average, an electron number of 2.5 is transferred. Still, for some of the time segments, the charge flow is against the applied bias (n<0), which results in a temporary decrease of the system entropy. Similar measurements are carried out at temperatures of 500 mK and 700 mK see Figs. 2.1 (c)-(e),

Our results validate the theory in the near-equilibrium regime with a good accuracy. A remaining discrepancy is very well explained with a master-equation model of the finite-bandwidth detection. This agreement proves the usefulness of this corrective approach in compensating for a slow detector. In the regime far from equilibrium, our results display a strong dependence on the internal level structure controlled by gate voltages. In configurations where our system is well described as a three-state Markovian system, we observe a good agreement with theory, demonstrating the potential of the double quantum dot as a model system for the study of nonequilibrium thermodynamics. Our results anticipate the test of the FT in quantum-coherent electron transport, which requires the measurement of thermal fluctuations on a sub-Kelvin energy scale.

## 2.2 Counting statistics in an InAs nanowire quantum dot with a vertically coupled charge detector

T. Choi, T. Ihn, S. Schön, and K. Ensslin

Single spins in semiconductor quantum dots (QDs) are considered as possible candidates for qubits for solid-state quantum information processing. Many essential experiments have been done in split-gate defined QDs formed in GaAs/AlGaAs two-dimensional electron gases (2DEGs) where coherent rotations of single spins and the coherent exchange of two spins have successfully been demonstrated. While the realization of a spin qubit in such split-gate defined QDs in GaAs/AlGaAs 2DEGs is well established by now, much work focuses on the implementation of spin qubits in other material systems, where different material properties could be advantageous for both longer coherence times or fast manipulation of the spin. For example, systems with negligible nuclear spin and weak spin-orbit interaction such as carbon nanotubes, graphene, or Si-based systems are thought to be promising due to the expected long spin coherence time. On the other hand, systems with strong spin-orbit interaction would promise an efficient manipulation of the spin using only electric fields. Spin-orbit mediated coherent rotation of a single spin has been demonstrated in split-gate defined GaAs QDs and recently in an InAs nanowire establishing a so-called spin-orbit qubit.

The InAs nanowires used in this work are grown by metal organic vapour-phase epitaxy on a GaAs substrate using colloidal Au particles as catalysts. The crystal structure of the nanowires is wurtzite and the nanowires are typically 100 nm in diameter and up to 10 $\mu$m long. The nanowires have a hexagonal cross section and grow perpendicular to the substrate. After growth, the nanowires are deposited on a molecular beam epitaxy grown AlGaAs/GaAs heterostructure containing a 2DEG 37 nm below the surface, where the nanowires come to lie parallel to the surface of the heterostructure. The quantum point contact charge detector is defined by wet chemical etching in such a way that the detector is positioned exactly below the nanowire. A pad of crosslinked PMMA on top of the nanowire is used as a gate insulator. As a final step, three top gates are fabricated by EBL and the evaporation of Ti/ Au. The top gates have a width of 40 nm and a spacing of 128 nm. A false color scanning electron micrograph (SEM) image and a schematical cross section of the sample are shown in Fig. 2.2. The QPC acts as a charge detector for the nanowire QDs and at the same time as a global back gate to tune the electron density in the nanowire. The side gates in the 2DEG are used to tune the conductance of the QPC to a slope where it is sensitive to changes of the electron number of the QDs. All measurements presented are performed at a temperature of T=1.5 K. By applying negative voltages to the top gates, QDs can be formed in the nanowire. Clear Coulomb blockade peaks can be seen in the current through the nanowire. At the same time, the QPC is tuned to a sensitive operating point using the side gates. Steps in the conductance of the QPC appear whenever the electron number of the QD changes by one. The QPC is able to detect transitions even when the current through the nanowire gets too small to be measured directly.

Since electron transport through a QD is governed by Coulomb blockade, the noise is expected to be sub-Poissonian. Thus, the Fano factor F=S/2eI, with S the shot noise and I the average current, is smaller than one. We have presented a

design for highly tunable InAs nanowire QDs with very sensitive charge detection. The high tunability and sensitivity enabled time-resolved charge detection and the measurement of the full counting statistics (FCS). The data agrees with the FCS theory for single-level transport even though $k_BT$ is comparable to the single-particle level spacing in the dot. By reducing the size of the QDs, we expect to be able to reach the few-electron regime and to carry out single-spin detection and manipulation with the help of a charge detector.

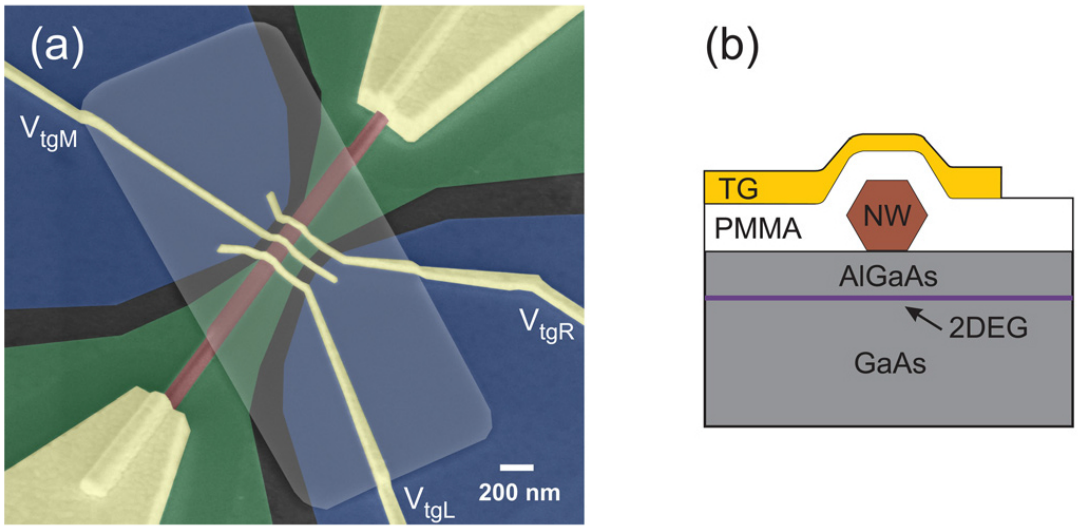


**Figure 2.2:** (a) Tilted SEM image of a sample with the same design as the one measured (false colors). The InAs nanowire is deposited on an AlGaAs/GaAs heterostructure with a 2DEG 37 nm below the surface. Etched trenches in the 2DEG (in black) define a QPC below the nanowire. Side gates in the 2DEG are used to tune the QPC. Three top gates on top of the crosslinked PMMA (bright pad) are used to define the QDs. (b) Schematical cross section of the sample. The PMMA serves as a gate insulator between the nanowire and the top gates.

## 2.3 Dipole Coupling of a Double Quantum Dot to a Microwave Resonator

T. Frey, P. J. Leek, M. Beck, T. Ihn, K. Ensslin, and A. Wallraff, in collaboration with A. Blais, Universite de Sherbrooke, Canada

Typically, quantum dots are investigated by direct current (dc) transport measurements or using quantum point contacts for charge sensing. Here, we have realized a novel device in which a semiconductor double quantum dot is dipole coupled to a GHz-frequency high-quality transmission line resonator. This approach allows us to characterize the properties of the double dot by measuring both its dispersive and dissipative interaction with the resonator. In addition to providing a new readout mechanism, this architecture has the potential to isolate the dots from the environment and to provide long distance coupling between spatially separated dots. These features are expected to improve the potential for realizing a quantum information processor with quantum dots as previously demonstrated for superconducting circuits making use of circuit quantum electrodynamics (QED).

The sample we have investigated in our experiments comprises a microwave resonator which is realized using a 200 nm thick aluminum coplanar waveguide on GaAs which is capacitively coupled to an input and output line to probe its transmission spectrum. The double quantum dot is positioned at an antinode of the standing wave field distribution of the resonator. The left and right dots (LD, RD) are arranged in series with respect to the source and drain (S, D). A selective capacitive coupling between the two systems is mediated by a gate [resonator gate (RG)] extending from the resonator to the right quantum dot only. This coupling scheme results in a strong microwave frequency dipole interaction of the resonator with two charge states in which an electron is on either the left or right quantum dot.

We first investigated the dc transport properties of the double quantum dot [see Fig. 2.3 (a)] by applying a source-drain voltage. To change the electrostatic potentials on the quantum dots, the voltages $V_L$ and $V_R$ are varied while all other gate voltages are fixed. We observe a hexagon charge stability pattern, which is characteristic for electron transport through double quantum dots. Within each hexagon, the number of electrons (N,M) in the dots is fixed. At the

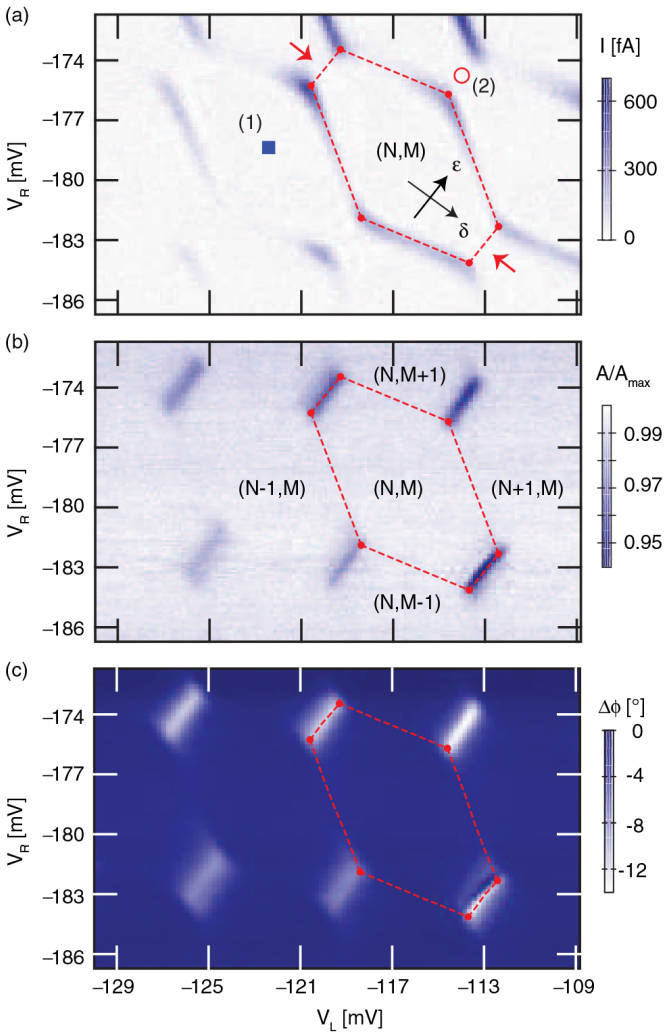


**Figure 2.3:** (a) Measurement of the direct current through the double quantum dot versus $V_L$, $V_R$ (no microwave signal applied). A small background current is subtracted from each horizontal line of the data set. The dashed line outlines a region with fixed electron number (N,M). The $\epsilon$ and $\delta$ axes indicate the direction of the mean and the detuning energy of the two quantum dots. (b) Resonator transmission amplitude at fixed measurement frequency in the same gate voltage range as in (a). The red dashed lines highlight the same hexagon as in (a). (c) Transmission phase change with respect to resonator frequency, gate voltages as in (a). Red dashed lines as in (a).

triple points, where three charge states are degenerate, charge transport is energetically possible and a conductance resonance is observed. The current observed along four of the hexagon boundaries is caused by cotunneling or molecular orbital states. At the two hexagon 0.002 boundaries indicated by red arrows in Fig. 2.3 (a) at which no dc current was measured, two quantum dot charge states with the same total number of electrons are degenerate. Along this direction, the mean energy of the two quantum dots is tuned with respect to the chemical potentials of the leads. The energy detuning between the charge states of the quantum dots is changed along a second axis indicated in the same figure. Both quantum dots contain on the order of 100 electrons. The microwave resonator has a fundamental frequency 6.755 GHz and a loaded quality factor of 2630 corresponding to a decay rate of 2:6 MHz, measured with all gates grounded such that no quantum dots are formed. The resonator is approximately prepared in its ground state with average thermal photon number $n<1$ using appropriate filtering and attenuation in the microwave lines. When the double quantum dot is formed by applying negative gate voltages, we find that the resonator frequency and linewidth are sensitively dependent on these voltages, see Fig. 2.3 (b) and (c).

The dipole coupling of a double quantum dot to an on-chip superconducting microwave resonator was demonstrated. The double dot charge stability diagram was probed by measuring resonator frequency shifts. Two different characteristic regimes with interdot tunnel couplings above or below the resonator frequency could be observed and explained.

This demonstrated that our architecture offers a new way to probe semiconductor quantum systems in the microwave regime, and may be used, for example, for high energy-resolution measurements of double quantum dots and fast time-resolved measurements, in addition to being a promising platform for potentially scalable hybrid solid-state quantum information processing. The presented scheme could be extended to other material systems, manipulating and reading out spin qubits and coupling them to a microwave resonator using either ferromagnetic leads or spin-orbit effects.

## 2.4 Transport in a three-terminal graphene quantum dot in the multi-level regime

A. Jacobsen, P. Simonet, K. Ensslin and T. Ihn

Graphene nanostructures are believed to have potential applications in both conventional electronics and solid-state quantum information processing. In particular, graphene quantum dots are promising for spin qubits due to their predicted long spin lifetimes. As a consequence of the gapless band structure, charge carriers cannot be electrostatically confined in graphene. However, by cutting graphene into narrow ribbons, a so-called transport gap is opened where the current is suppressed around the charge neutrality point. By using short and narrow constrictions as tunnel barriers, more complicated nanodevices such as quantum dots have been successfully created. This has led to a number of experiments where, for example, excited states have been observed in single and double quantum dots, spin states have been investigated and the electron-hole crossover has been studied. In addition, the modulation of transport through graphene quantum dots due to localized states in the constrictions has been investigated in several studies. Still, there are open questions concerning the detailed influence of constriction localizations on the transport on small energy scales. The current through a two-terminal quantum dot does not give access to the individual coupling strengths between the dot and each lead. However, if a dot in the single-level tunneling regime of the Coulomb blockade is connected to three or more leads, the individual tunnel coupling constants between each lead and the quantum dot can be determined from measurements of the conductance matrix of the system.

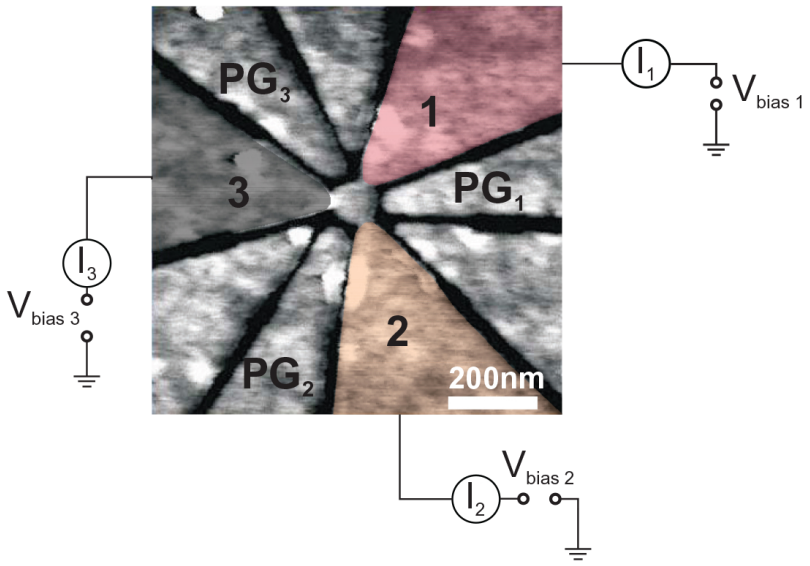


**Figure 2.4:** (a) Scanning force micrograph image of the measured quantum dot with a sketch of the measurement setup. Leads 1, 2 and 3 are highlighted in red, orange and black, respectively. Three plunger gates are used to tune the dot in addition to the global back gate (BG). To each lead a bias voltage can be applied and the current flowing can be measured.

Single-layer graphene flakes were exfoliated from natural graphite, deposited onto a highly doped silicon substrate covered by 285 nm thermal silicon dioxide and identified using Raman spectroscopy and light microscopy. In a first electron beam lithography (EBL) step, followed by metal deposition of 5 nm titanium, 45 nm gold and lift-off, the Ohmic contacts were added to the flake. The structure is then patterned by a second EBL step, followed by reactive ion

etching with argon and oxygen. A scanning force micrograph (SFM) image of the measured quantum dot is depicted in Fig. 2.4. The quantum dot is connected to three leads, labeled 1, 2 and 3, through narrow constrictions. From the SFM image the diameter of the dot is determined to be 110 nm and the width of the constrictions is found to be 40 nm. In addition to the global silicon back gate (BG), three in-plane plunger gates, PG1, PG2 and PG3, are used to tune the dot and the constrictions. The remaining three in-plane gates influence the transport through the dot only weakly and are therefore not used. In figure 2.4 we additionally sketch the measurement setup. In all measurements presented in this study, a dc bias voltage is applied to one of the three leads, while the other two leads are grounded. The currents through the three leads are measured simultaneously using current-voltage converters. All measurements are carried out at 1.7 K unless otherwise stated.

The dot was thoroughly characterized both by gate-gate sweeps where all relative lever arms could be extracted and by temperature-dependent measurements. When investigating single Coulomb peaks in more detail, a shift in peak maxima between conductances measured in the different leads was observed. This result can be qualitatively reproduced by a rate equation model where different leads couple differently strongly to different dot states. The shift can be tuned by the plunger gates, and by investigating the corresponding evolution of the individual conductances we find no correlation between this evolution and the relative lever arm determined. We therefore conclude that on small energy scales the changes in coupling are due to changes in the dot wave function, which is rather a single wave function extended over the dot than several localized states. This is an important insight in view of the potential to use graphene quantum dots for spin qubits.

## 2.5 Optimization of sample-chip design for stub-matched radio-frequency reflectometry measurements

S. Hellmüller, M. Pikulski, T. Müller, B. Küng, G. Puebla-Hellmann, A. Wallraff, M. Beck, K. Ensslin, and T. Ihn

High-frequency reflectometry measurements in semi-conductor nanostructures allow dispersive state readout detecting the state-dependent Òquantum capacitanceÓ of a qubit and time-resolved charge state detection using a quantum point contact (QPC) or a single-electron transistor as charge detector. We investigate a radio-frequency (rf) matching circuit as an approach to reach higher detection bandwidths in single-shot measurements compared to dc read-out techniques. This was motivated by exciting experiments such as the measurement of a single electron spin by spin-to-charge conversion, the measurement of full counting statistics, and single-shot readout of a spin qubit. In contrast to previously demonstrated rf techniques, we use a stub-matching approach, adopted from microwave impedance matching.

The basic idea of reflectometry measurements is to detect the reflection of a rf-signal depending on the load terminating the waveguide. The reflection coefficient is most sensitive to changes of the load impedance $Z_L$ if $Z_L$ is close to the characteristic impedance $Z_0$ of the waveguide of 50 $\Omega$. The setup is sketched in Fig. 2.5 (a). A rf carrier signal is generated by a vector network analyzer (VNA) and applied to the sample via a directional coupler. Before reaching the sample, a dc component is added to the signal by using a bias tee. At the PCB, containing matching circuit and sample, the rf signal is partly reflected and afterwards amplified by 60 dB using a 2.4 GHz room temperature amplifier before reaching the input port of the VNA. Dc blocks are used to avoid ground loops. All components except for the PCB are placed at room temperature for ease of calibration. A schematic of the PCB is shown in the dashed box in Fig. 2.5 (a) and on the photograph in Fig. 2.5 (b). The sample chip including the QPC (shown in the atomic force microscope (AFM) scan in Fig. 2.5 (a)) is glued into a holder and connected with bond wires. In Fig. 2.5 (c), the absolute value of the reflection coefficient versus frequency f for a fixed diode voltage is shown. The PCB is designed for a matching frequency close to 3 GHz, and we measure a full width at half maximum of around 100 MHz, which puts an upper limit on the setup bandwidth.

An in situ tunable shunt stub matching circuit was investigated in detail. We observed that the sample chip design can be improved significantly leading to up to a factor of 3 improvement by integrating coplanar waveguides into the design. A smaller improvement is achieved by simply reducing the distance between Ohmic contact and QPC.

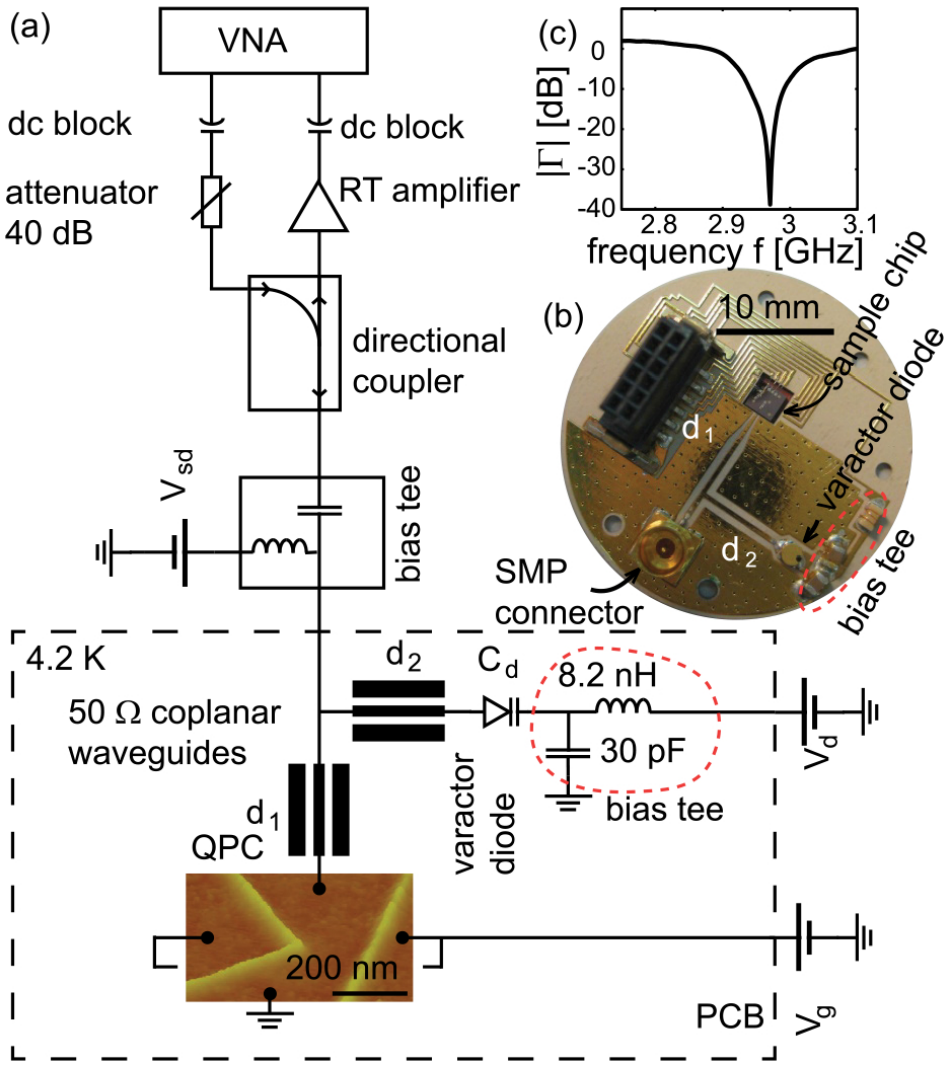


**Figure 2.5:** (a) Experimental setup used to perform the measurements and designed for carrier frequencies of 2.4 GHz. (b) Photograph of the PCB with the two stubs terminated by a varactor diode and the QPC, respectively. Two capacitors and one inductor placed after the diode act as on-chip bias tee. (c) Absolute value of the reflection coefficient as a function of the carrier frequency for a QPC tuned to three conductance quanta.

These designs can be adapted to other rf-matching circuits as well. The design of the matching circuit integrated into the PCB can be adjusted to higher resonance frequencies by decreasing the stub lengths accordingly. The tunability of the matching circuit facilitates impedance matching and the measurement of a variety of different samples in the future such as InAs nanowire or graphene quantum structures which are promising for an increased coupling between detector and nanostructure.

## 2.6 Reactive-ion-etched graphene nanoribbons on a hexagonal boron nitride substrate

D. Bischoff, T. Krähenmann, S. Dröscher, M. A. Gruner, C. Barraud, T. Ihn, and K. Ensslin

Graphene has received tremendous attention since it became easily available for experiments. Only a few years later, the first graphene-based nanostructures were reported. Among others, small stripes called nanoribbons and quantum dots were investigated. In order to understand the limitations of graphene nanostructures better, a large

effort was put into studying graphene nanoribbons which are the simplest nanostructures and also the building blocks of more complex systems. It was found that charge carriers get localized inside these structures uncontrollably due to either bulk or edge disorder (or a combination of both), which limits reproducibility as well as control of graphene nanodevices. The electronic transport properties of micron-sized graphene devices were improved by exchanging the traditional silicon dioxide substrate with a more suitable material. The substrate could either be totally removed (ÒsuspendedÓ) or replaced by hexagonal boron nitride (hBN). It was shown that suspended graphene in combination with current annealing can lead to high-quality nanostructures. Nanostructures patterned on a substrate are, however, more amenable to the realization of complex device geometries.

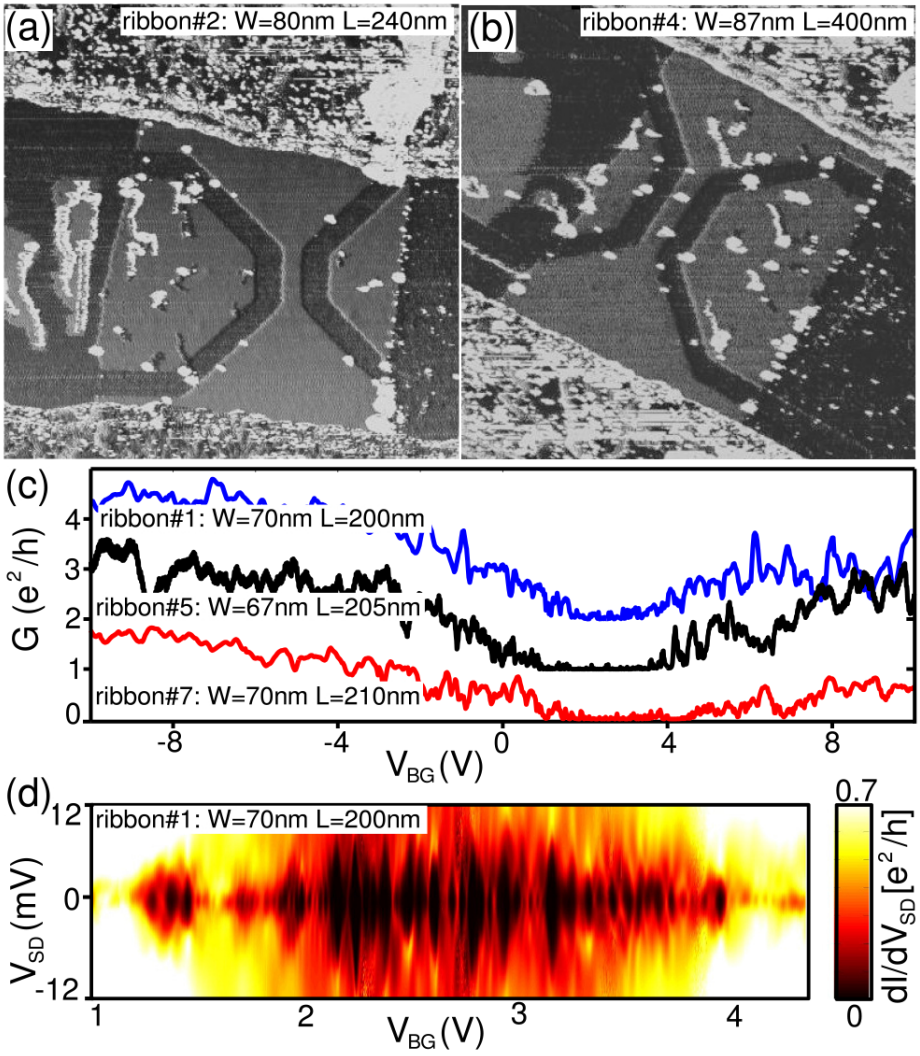


**Figure 2.6:** (a) and (b) Scanning force microscopy image (phase) of two representative nanoribbons. (c) Conductance of three different ribbons that have comparable dimensions (1 mV bias applied). The curves are vertically offset by $e^2/h$ for clarity. (d) Differential conductance as a function of symmetric source-drain bias and back-gate voltage for the blue ribbon trace (ribbon 1 in (c)).

Electrical transport properties may change for reactive-ion-etched graphene nanodevices by fabricating them on hexagonal boron nitride rather than on a silicon dioxide substrate. We report on the fabrication and electrical measurements of both micron-sized stripes and nanoribbons built of single layer graphene on a hexagonal boron nitride substrate. The experiment is designed such that a direct comparison with previous experiments is possible where similar ribbons fabricated with the same process were investigated on a silicon dioxide substrate. We show that our micron-sized devices exhibit superior transport properties to those on silicon dioxide in agreement with literature. At the same time, the electrical properties of the nanoribbons on boron nitride are found to be comparable to devices on silicon dioxide. In both cases, electrical transport is characterized by the random formation of localized charge

ÒpuddlesÓ and activated transport through them. We conclude that the rough edges in our devices have an important influence on electronic transport in our graphene nanostructures and that simply exchanging the substrate yields no clear improvement. In order to change the edges of graphene nanostructures in the future, they could for example be passivated or controlled on an atomic scale. Alternative ways to confine electrons in graphene by locally opening a bandgap include among others functionalizing the graphene or local electrostatic double-gating of bilayer graphene.

## 2.7 Scanning gate microscopy on a graphene nanoribbon

N. Pascher, D. Bischoff, T. Ihn, and K. Ensslin

Graphene is a material which was recently isolated and deposited as a monolayer. It has various special properties including considerable charge carrier mobilities at room temperature making it a valid candidate for possible applications in electronics. The material consists of a single layer of carbon atoms forming a two-dimensional crystal. Due to expected long spin lifetimes, graphene is also a candidate for various applications in nano- and quantum electronics. The basic building block for any electronic device are wires and constrictions that connect the different parts of the device. These small stripes of graphene are usually called Ònanoribbons.Ó It has been shown that graphene nanoribbons can exhibit an effective transport gap which is attributed to the formation of charge localization within the ribbon. In graphene, a two-dimensional electron gas (2DEG) is formed, which lies directly at the surface. This makes it especially accessible for scanning probe techniques. While conventional transport experiments just integrate over the entire structure obtaining little or no spatial information, scanning gate microscopy (SGM) allows to probe the 2DEG with high resolution and accuracy both in real space and energy. This measurement technique uses the conducting tip of an atomic force microscope (AFM) to locally gate the nanostructure, while its conductance is measured as a function of the tip position. The method is perfectly suited to probe graphene nanostructures, as some very fundamental mechanisms, like the formation of charge localization inside the narrow constriction, are still subject of intense theoretical debate. Various microscopic mechanisms for the formation of charge localization have been postulated. Many of these theories make assumptions about the position of the localized charges in real space. Thus, it is promising to combine transport measurements with methods offering spatial resolution.

The effect of the voltage-biased tip on transport through a quantum dot has been studied extensively in various material systems, e.g., GaAs, graphene and many other material systems. Localized charges have been imaged with this technique in InAs nanowires and carbon nano-tubes. Previous experiments show concentric rings, which originate where quantum dots form either due to fabrication or localization in a disorder potential. In Fig. 2.7(a), the scanning gate image taken with a tip-sample distance of 20 nm at a temperature of 1.7 K, a source-drain bias of 0.1 mV and a backgate voltage of 18 V is related to the lithographic outline (white dashed lines) of the nanoribbon. The tip-voltage of 2 V was determined to be a parameter, where the tip is little invasive. A rich pattern is visible, with a correlation with the ribbon geometry. There are two centers of enhanced conductance in the middle of the structure. If the average conductance over all lines scanned vertically is taken, an increased conductance can be seen at the position of the ribbon.

When the tip-induced potential is scanned along a line across a quantum dot, alternately the conditions of electron tunneling will be fulfilled and not fulfilled, thus, a Coulomb-peak like pattern is expected to occur for every line. If the backgate voltage is changed, this leads to a rising or lowering of the ladder of energy states inside the dot. Thus, to fulfill the condition for electron tunneling, a different part of the peaked lineshape of the tip-induced potential will be probed and this change of the energy relations of the quantum dot and the tip will lead to a shifted peak-pattern as a function of tip position. For each quantum dot which is located inside the channel we expect peak shaped curves reflecting the tip induced potential. Thus, this pattern is expected to allow us to characterize the existing QDs with spatial resolution. The presence of the families of peaked curves in Fig. 2.7(b) and (c), which occur because the tip-induced potential helps to overcome Coulomb-blockade, allows to identify the two sites as QDs as schematically shown in Fig. 2.7. If there were just two local tunnel-barriers present in the structure, such behavior could not be observed. Scanning gate microscopy proves to be a powerful tool to characterize transport properties of graphene quantum structures. Particularly important is the possibility to find and locate localized sites, which unintentionally

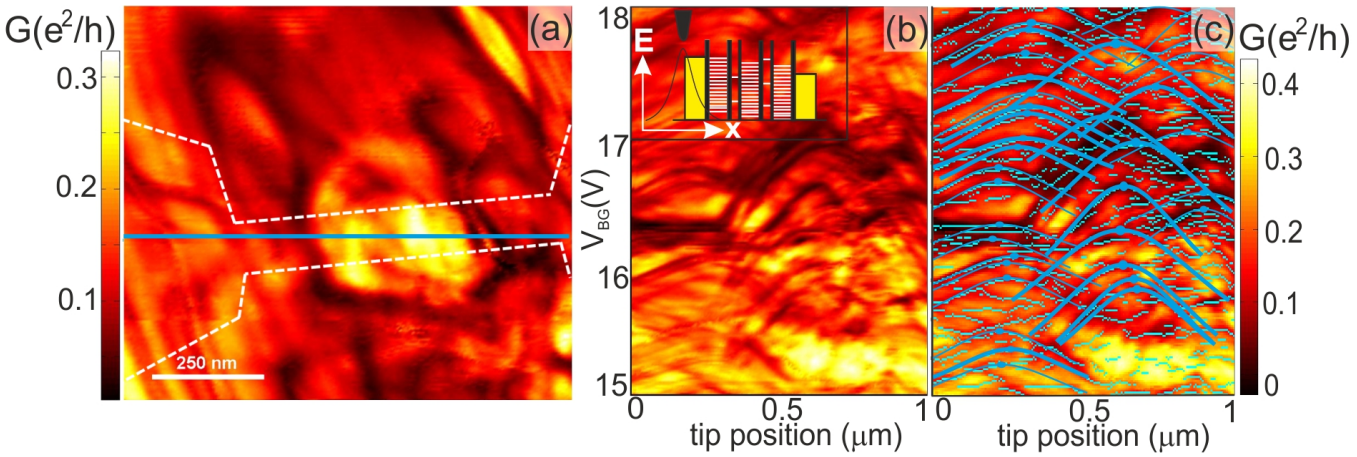


**Figure 2.7:** (a) Scanning gate image of the nanoribbon. The lithographic outline is shown via the white dashed lines. Two centers of enhanced conductance can be seen as bright spots. The rich pattern far away from the graphene structure is attributed to the effect of trapped charges inside the substrate.(b)Linescan parallel to the nanoribbon along the blue line in (a). After each line is finished the voltage applied to the backgate is changed. a) Raw data. Insert: Proposed model for interpretation. Transport is dominated by two small quantum dots with large spacing of quantized energy levels. (b) Light blue pixels describe positions of local minima in y-direction as evaluated numerically. The series of Lorentzian curves (solid blue lines as guide for the eye manually overlaid using the local minima. Dots mark their centers) represent at least two QDs forming inside the structure. The shifting of the centers of the curves indicates that the QDs shift in real space as a function of backgate voltage.

form inside a narrow constriction. In the nanoribbon which is examined here, we find that transport must be dominated by two rather small quantum dots, which is consistent with previous transport experiments. Future experiments will have to focus on how to minimize the contrast arising from charges in the substrate.

## 2.8 Electron flow in split-gated bilayer graphene

S. Dröscher, C. Barraud, T. Ihn and K. Ensslin, in collaboration with K. Watanabe and T. Taniguchi, Tsukuba, Japan

Graphene nanostructures have triggered intensive research efforts, both theoretical and experimental. Proposals for the manipulation of individual spin states in graphene quantum dots have been made, and the excited charge and spin states in graphene quantum dots have been experimentally observed. These results show that confining single electrons is possible and constitutes an important step towards fully controlled electronic states in graphene nanostructures. Up to now, nanostructures in graphene have been realized mainly by etching the flakes through a lithographically defined mask. Split-gate defined nanostructures cannot be realized in single-layer graphene because an intrinsic band gap is absent and Klein tunneling occurs between n- and p-doped regions, which prevents electrostatic gating. A promising technological alternative has been unveiled by the use of bilayer graphene since a band gap can be electrically induced and tuned in this material. Electrostatic confinement of carriers thus becomes possible, as with semiconductor-based devices. The apparent advantage of this method is the smoother confinement potential expected, in contrast to the rough and uncontrolled edges on a microscopic scale in present-day graphene nano-devices.

Mechanical exfoliation of natural graphite is used to extract bilayer graphene flakes and deposit them onto an $Si/SiO_2$ substrate. Thin flakes were identified using an optical microscope. Subsequent atomic force microscope (AFM) measurements as well as Raman spectroscopy were carried out to verify the flakesÕ bilayer nature. Ohmic contacts were defined by electron beam lithography (EBL) followed by metal evaporation (2 nm Cr and 40 nm Au) and a lift-off process. Hexagonal boron nitride (BN) was deposited on the bilayer flake as a dielectric material. Since micrometer-sized flakes of this material are mechanically exfoliated as well, we used the mechanical transfer technique developed by Dean et al to place a BN flake at the desired position on a chip. After covering the contacted bilayer graphene flake with Å 7.5 nm thick BN, top gate electrode patterns were defined by EBL. Finally, metal was evaporated (0.5 nm Cr and 45 nm Au) and the gate fingers were revealed by a subsequent lift- off. A schematic diagram of such a sample is

shown in Fig. 2.7(a). Panel (b) of the same figure displays an atomic force micrograph of the device studied here.

We have verified that a band gap can be opened in the region of the bilayer graphene flake covered by the continuous top gate stripe marked with a blue solid line in figure 2.8(b). Here, a four-terminal measurement was carried out using contacts (3)–(6). In order to split the valence and conduction band edges in bilayer graphene, the layer symmetry has to be broken. Such an asymmetry is imposed by an electric field oriented perpendicularly to the bilayer graphene plane. Measurements of the resistance through the device as a function of the back gate and top gate voltage were done. From a back gate trace at zero applied top gate voltage, we extracted the charge carrier mobilities using the parallel plate capacitor model. For both holes and electrons we determined the mobilities to be $\mu \approx 4000 cm^2/Vs$.

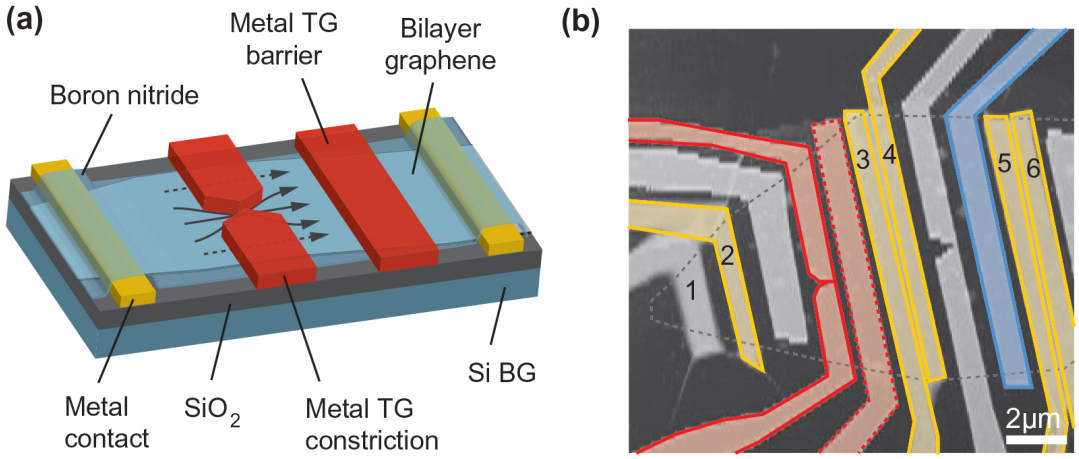


**Figure 2.8:** ((a) Schematic diagram of a double-gated bilayer graphene flake. The graphene flake resides on Si/$SiO_2$ substrate and is electrically contacted with metallic electrodes (yellow). The boron nitride flake (light blue) covers the bilayer graphene and these electrodes. Top gate fingers (red and blue) are deposited last. The gray arrows indicate where current can flow through the split-gate structure. (b) AFM image of the bilayer graphene device. The black dotted line outlines the graphene flake, the red solid line indicates the split-gate structure considered in this paper and the red dotted line outlines the barrier, which is directly compared with the constriction. The blue solid line marks the barrier measured separately and presented in figure 2, and the yellow solid lines mark the ohmic contacts used. The width of all top gate fingers is W = 900 nm.

We have carried out transport measurements in a dual-gated bilayer graphene device. By applying a perpendicular electric field between the global back gate and the local top gates the conductance is strongly modulated in the gated regions since a band gap is opened. However, we observe an increased conductance with temperature by activated transport through gap states. Our measurements show that charge carriers can be guided through electrostatically defined nanoconstrictions. The observed interference effect, leading to fluctuations in the transconductance signal, was identified as originating from the narrow transport channel defined by the split gates. We attribute them to universal conductance fluctuations, indicating that the device is in the diffusive regime. Recent experiments on dual-gated suspended bilayer graphene devices demonstrated that phenomena such as Coulomb blockade and quantized conductance are observable in gate defined quantum dots and quantum point contacts. These free-standing devices typically exhibit excellent transport quality, implying a smooth potential landscape. Alternatively, similar properties are achieved by using boron nitride as the substrate. Hence, bilayer graphene, which is encapsulated between two BN flakes, is a promising candidate for electrostatically defined nanostructures in the ballistic transport regime.

## 2.9 Fast detection of single-charge tunneling to a graphene quantum dot in a multi-level regime

T. Müller, J. Güttinger, D. Bischoff, S. Hellmüller, K. Ensslin, and T. Ihn

Time-resolved charge detection on quantum dots is a powerful technique to straightforwardly extract single-particle transport properties such as the occupation probability of quantum dots determined by the Fermi distribution function

in the leads and the dot-lead tunneling rates. Recording the charge-detector signal through radio- frequency (rf) reflection measurements can enhance the time resolution drastically, enabling studies of systems with larger tunneling rates. The application of rf reflectometry on a graphene quantum dot with its concomitant speed-up in detection time presented here consequently opens the door for a variety of fascinating studies on transport phenomena in graphene quantum circuits. To date, charge-detection experiments mainly probe quantum dots in the single-level regime, and investigations involving transport through more than one level have focused on the phenomenon of super-Poissonian noise. Here, we present measurements and an analytical calculation of multi-level tunneling rates using a graphene single quantum dot connected to only one lead, thus ensuring that the tunnel barrier the charge carriers need to overcome is the same for tunneling-in and -out. It should be noted that the restriction imposed by studying the same barrier requires charge detection, and in combination with the desire for multi-level tunneling graphene quantum dots turn out to be appropriate toy systems for studying this unusual parameter regime but in principle our results are applicable to any other material system.

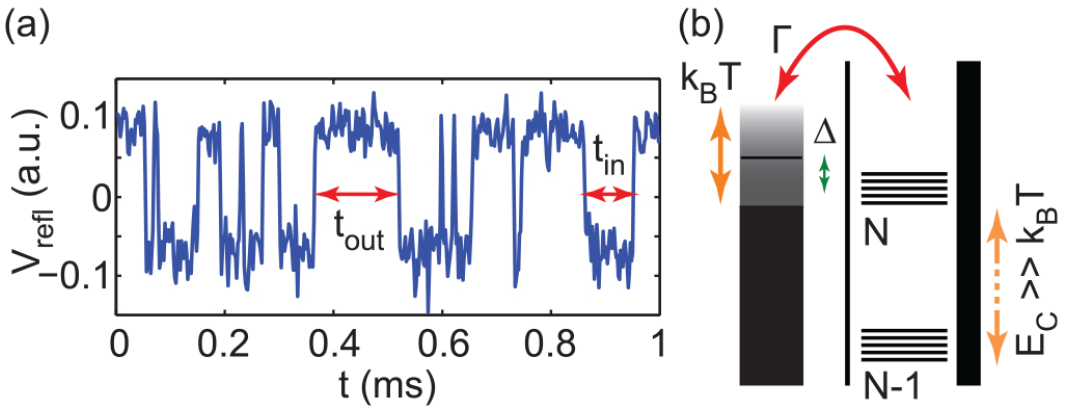


**Figure 2.9:** (a) Time-dependent rf signal, 8-th order Bessel low-pass filtered at 200 kHz and sampled at 500 kHz, revealing the times $t_{in}$ and $t_{out}$ the quantum dot is occupied or unoccupied by a single negative excess charge. (b) Sketched energy diagram corresponding to the multi-level regime studied here. A quantum dot with a closely spaced energy spectrum is connected to a lead with a tunnel rate $\Gamma(E)$. The Fermi function of the lead is softened by a temperature T which is much larger than the level spacing but much smaller than the charging energy $E_C$. The difference between the Fermi level in the lead and the chemical potential of the quantum dot is denoted by $\Delta$.

Tuning all gate voltages such that the quantum dot is at a charge-degeneracy point between N-1 and N negative charges on the dot, and recording the charge-detector conductance via rf reflectometry, allows for studying tunneling of single charge carriers in real-time, as shown in Fig. 2.9(a). This trace has been 8-th order Bessel low-pass filtered at 200 kHz, roughly two orders of magnitude faster than with previous time-resolved experiments on graphene quantum dots - and sampled at 500kHz to ensure large enough signal-to-noise ratio for reliable electron counting. From the average time a negative charge spends inside (out of) the dot we can compute the dot occupation probability and the rate for tunneling out of (into) the quantum dot.

At our elevated temperatures, we have good reason to assume that we are in a multi-level tunneling regime. Thus, we calculate the tunneling rates of a quantum dot connected to one lead in the multi-level regime schematized in Fig. 2.9(b). We have performed fast time-resolved charge-detection measurements on a graphene quantum dot. By using rf reflectometry, we could enhance the read-out bandwidth by two orders of magnitude compared to previous charge-detection experiments on graphene. To test this method, we have extracted the rates for tunneling-in and tunneling-out of the dot through the same lead, which are in good agreement with an analytical model for multi-level tunneling to a single lead. This type of fast charge detection on graphene quantum dots opens possibilities for studying interactions of Dirac Fermions in the framework of full counting statistics and is a great instrument for determining spin relaxation times in graphene quantum dot circuits.

## 2.10 Quantum dot occupation and electron dwell time in the cotunneling regime

B. Küng, C. Rössler, M. Beck, J. Faist., T. Ihn and K. Ensslin

Quantum dots (QDs) coupled to source and drain electrodes represent versatile and well-controlled systems for the study of mesoscopic transport. The many aspects of electron tunneling through QDs are typically studied by measuring either the QD conductance or the QD charge occupation. There are several techniques available for measuring the QD charge occupation, among them direct capacitance measurements, and the use of single-electron transistor and quantum point-contact (QPC) electrometers. More insight can be gained when combining charge and conductance measurements and extracting information from both of them to obtain a more complete picture of the system. In the sequential tunneling regime of the QD, combined charge and conductance measurements can be used to determine the system timescales, whereas in a strong-coupling regime, such measurements reveal the effect of Kondo correlations on the charge of a QD.

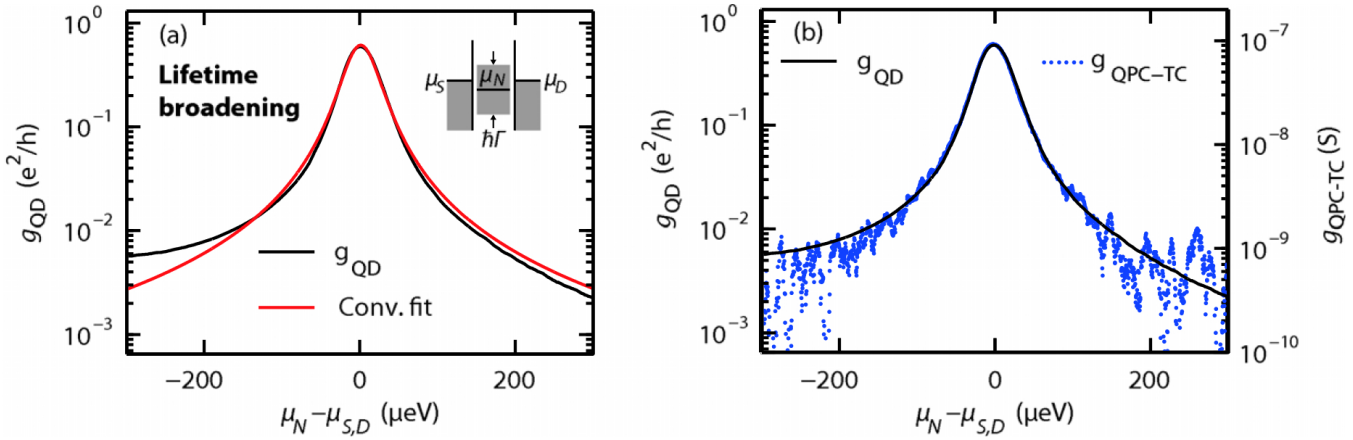


**Figure 2.10:** (a) Differential QD conductance $g_QD$ (black) in the regime of strong dot-lead coupling along with a fit (red) to a Fermi-Lorentz convolution (fit parameters $h\Gamma = 37.8\mu eV$, whereas the parameter $k_BT = 4.4\mu eV$ was held fixed). (b) Black solid curve: the same data as in (a). The blue dotted curve is the transconductance signal measured with the QPC. Both data sets have been smoothed over a range of $7.5\mu eV$ (20 data points).

The coupling strength of the QD state to the leads is controlled with gates. The lifetime broadening of the QD state can be continuously tuned from below to above the thermal energy $k_BT$ corresponding to the temperature of the electrons in the leads. The larger of the two energy scales determines the line width of the conductance resonances of the QD. The limiting regimes are characterized as thermally activated single-level transport if the lifetime broadening is the smallest energy scale, and as a Breit-Wigner transmission resonance if $k_BT$ is the smallest energy scale. We experimentally approach the two regimes in the measurements shown in Fig. 2.10. In both regimes, the QPC transconductance signal was measured simultaneously with the QD conductance. In Fig. 2.10(b), we plot the two signals on top of each other for comparison. The scaling of the vertical axes is chosen so to achieve an optimal overlap of the curves. Indeed, QD conductance and QPC transconductance match well over the covered range of signal strength, about two orders of magnitude.

We have presented simultaneous measurements of the conductance and charge occupation of a QD in several parameter regimes. At zero QD voltage, the charge signal is successfully interpreted in terms of the equilibrium occupation and the equilibrium conductance of the QD. Both in the regimes of weak coupling (dominated by thermal broadening) and of strong coupling (dominated by lifetime broadening), conductance and charge signal lineshapes are found to agree. At nonzero QD voltage, we study the inelastic cotunneling regime where the charge signal is generally weaker and where an analysis in terms of equilibrium occupation is not possible. We compare the charge signal to a theoretical signal calculated from the QD current and a charge carrier dwell time of h/E, where E is the blockade energy of first-order tunneling. Such a dwell time estimate is often derived from a cotunneling picture involving a virtual intermediate state with a lifetime bounded by an energy-time uncertainty principle. Since our measured charge occupation is smaller than the calculated one, our results support this cotunneling picture experimentally. Assuming an energy-independent dwell time allows for a good fit of the data in the accessible range of energies E. Further measurements carried out in a regime of mixed sequential tunneling and inelastic cotunneling are consistent with the

above interpretation. The charge occupation signal observed in this regime clearly exceeds the calculation based on a dwell time of h/E. This is as expected because of the longer carrier dwell time in sequential tunneling as compared to that in cotunneling.

# Chapter 3

# Dynamics of strongly correlated materials

(http://www.dscm.ethz.ch)

**Head**

Prof. Dr. Joël Mesot | Prof. Dr. Hans-Rudolf Ott

**Academic Staff**

Dr. Toni Shiroka | Francesco Casola | Marek Pikulski

**Administrative Staff**

Gabriela Strahm

## 3.1 Dimensional crossover of spin chains in a transverse staggered field

F. Casola, T. Shiroka, H.-R. Ott, and J. Mesot

in collaboration with G. Dhalenne and A. Revcolevschi (Université Paris-Sud, Orsay, France), A. Zheludev (ETH Zurich),

V. N. Glazkov (Kapitza Institute, RAS, Moscow, Russia), and A. Feiguin (Northwestern Univ., Boston, USA)

Heisenberg spin-$1/2$ chain materials are known to substantially alter their static and dynamic properties when experiencing an effective transverse staggered field originating from the varying local environment of the individual spins [1]. The local magnetic properties of the spin-chain compound $BaCu_2Si_2O_7$, which orders magnetically at $T_N = 9.2$ K [2], were studied by $^{29}$Si NMR. The data reveal the crossover from 1D behaviour at elevated temperatures to 3D features at $T \leq T_N$ to be dominated by a diverging transverse susceptibility. The latter, which is predicted by DMRG calculations, clearly influences the local magnetic field as monitored by NMR both above and below $T_N$ [3]. The $T$-dependence of the NMR-line shift shown in Fig. 3.1 can be understood by taking into account the influence of a local staggered transverse field (LTSF). The influence of the LTSF is also manifest below $T_N$ and indicates that the 1D character of the spin configuration competes with the 3D nature of the magnetic order. Our analysis of the LTSF implications, including a Landau-type expansion calculation [4], also explain some so-far unexplained spin-reorientation transitions reported earlier by other authors.

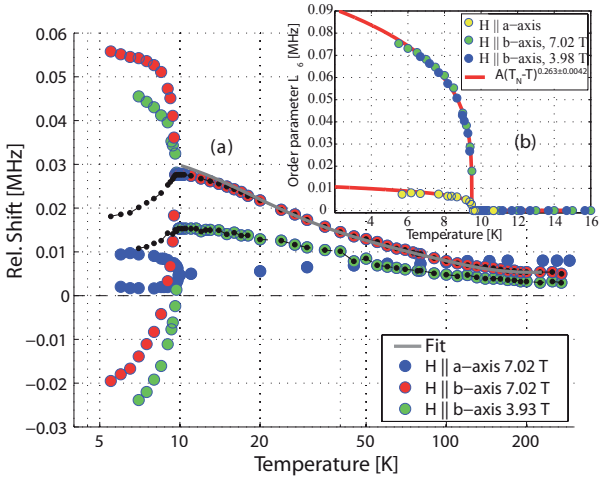


**Figure 3.1:** Relative $^{29}$Si NMR peak positions vs. temperature for magnetic fields along the $a$ and $b$ axes of $BaCu_2Si_2O_7$ (zero refers to the frequency of a $Si(CH_3)_4$ standard). Black dots indicate the mean values in the ordered phase, while the continuous gray line is a fit based on an LTSF model. Inset: The NMR line splitting below $T_N$ reflects directly the order parameter in the AF phase.

## 3.2 Field-induced quantum soliton lattice in a frustrated two-leg spin-$^1/_2$ ladder

F. Casola, T. Shiroka, H.-R. Ott, and J. Mesot

in collaboration with M. Grbić, M. Horvatić, S. Krämer, S. Mukhopadhyay, C. Berthier (LNCMI, Grenoble, France),

S. Wang and H. M. Rønnow (EPFL, Lausanne), Ch. Rüegg (PSI, Villigen), A. Feiguin (Northwestern Univ., Boston, USA)

Characterized by a strong spatial confinement and by enhanced quantum fluctuations, low-dimensional spin systems provide unique opportunities for enhancing our understanding of strongly-correlated electron systems. In $BiCu_2PO_6$, a well-known model compound for studying the effects of frustration in spin ladders [5], the substitution of Cu with Zn induces non-magnetic defects and corresponding local magnetization clouds. Maps of $H$-$T$ phase diagrams were obtained from data of low-temperature $^{31}$P NMR studies in magnetic fields between 11 and 32 T on single crystals of pure, $x = 0$, and $x = 0.01$ doped samples.

For $x = 0$ the onset of a field-induced magnetic ordering (FIO) at $T = 0$ K occurs at $H_c = 21$ T, with the phase boundary given by $T_c \sim (H - H_c)^{0.42}$. In the doped ($x = 0.01$) case, the site disorder mimics tunable ladder-leg lengths. Here the low-temperature, *defect-induced* ordering (IIO) is suppressed by a moderate field of 4 T. Subsequently, a *field-induced* order sets in below an analogous phase boundary as for $x = 0$, but with $H_c = 24.2$ T. Results of a low-field study of hyperfine interactions and a DMRG-based analysis of the NMR line shapes in the ordered regime were used to identify the details of the ordered structure, which includes the formation of a soliton lattice.

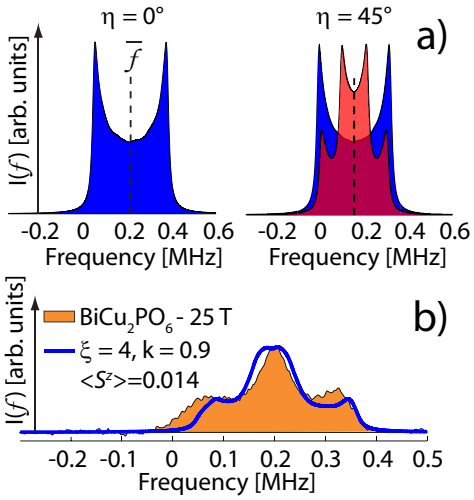


**Figure 3.2:** a) Simulated $^{31}$P NMR lineshapes $I(f)$ using a *classical* model with different parameters for a spin-cone arrangement. b) Expected NMR lineshape in case of a *soliton* lattice (blue line) and experimental NMR line for $BiCu_2PO_6$ taken at 0.25 K and 25 T (filled area).

## 3.3 Competing order parameters in low-dimensional antiferromagnets

T. Shiroka, F. Casola, and H.-R. Ott
in collaboration with V. N. Glazkov (Kapitza Institute, RAS, Moscow, Russia)

Phase diagrams of antiferromagnets in externally applied magnetic fields $H$ have been studied, both experimentally and theoretically, for many decades. In conventional collinear antiferromagnets the competition between Zeeman-, anisotropy-, and exchange interactions gives rise to several phase transitions. For example, if the antiferromagnetic order parameter has a preferred orientation (easy axis), a magnetic field applied along that axis provokes a spin-flop transition at a critical field value $H_c$, where the loss of anisotropy energy is compensated by a gain in Zeeman energy. Another transition in standard antiferromagnets, the spin-flip transition, occurs when the Zeeman energy exceeds the exchange energy. In the more complicated cases of non-collinear and/or frustrated antiferromagnets the choice of an ordered phase and the orientation of the relevant order parameter are dictated by a fine balance between the different interactions or by fluctuation effects. This competition implies rich phase diagrams with unusual features such as, e.g., the appearance of $M(H)$ magnetization plateaus.

Our work focused on the quasi-one-dimensional Heisenberg antiferromagnet $BaCu_2Si_2O_7$ which, due to the interchain couplings, undergoes a transition to the 3D antiferromagnetically ordered phase at $T_N = 9.2$ K. The temperature dependence of its static magnetization exhibits unusual features at low temperatures. Neutron-scattering experiments have confirmed the one-dimensional character of the spin system in BCSO, [2] a result reinforced by magnetic-susceptibility data along the $a$, $b$, and $c$ directions, respectively. Their variations with temperature exhibit the Bonner-Fisher maxima, as expected for spin chains at elevated temperatures. At lower temperatures, however, unexpected increases of $\chi_b$ and $\chi_c$ with decreasing temperature are observed above the Néel temperature $T_N$, atypical for this type of spin systems. More recent experiments probing the $^{29}$Si NMR line shift and its temperature dependence also revealed deviations from the expected conventional Bonner-Fisher behaviour [3].

Based on a conventional Landau approach which takes into account new results from experiments probing the local magnetization, both above and below the Néel temperature, [3] we have reconsidered the interpretation of the $H, T$ phase diagram of BCSO. The field-induced transverse staggered magnetization (TSM) competes with the order parameter of the phase with spontaneously broken symmetry below $T_N$. This competition induces additional phase transitions in non-zero external magnetic fields which influence the magnetization process. We demonstrate that a Landau-expansion-type analysis of the available data provides a semi-quantitative description of the phase diagram and predicts both the phase boundaries and their variation upon changing the external magnetic-field orientation with respect to the crystal axes.

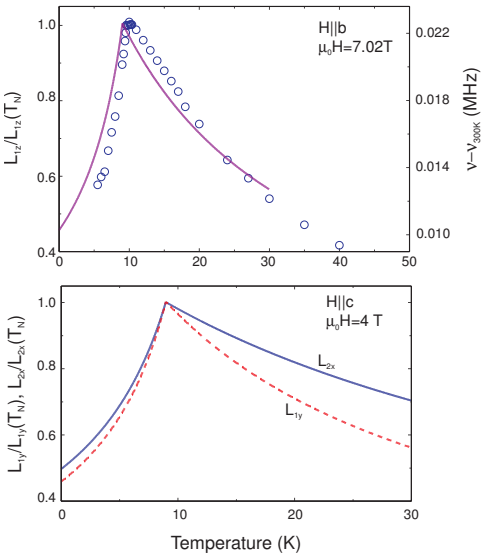


**Figure 3.3:** Upper panel: Comparison of the modelled temperature dependence of the field-induced order parameter (solid line) vs. the measured NMR line shift [3] (circles) ($\mathbf{H} \parallel b$ with $\mu_0 H = 7.02$ T). Lower panel: Temperature dependence of the field-induced "order parameters" related to the representations $L_{1y}$ and $L_{2x}$ (for details refer to ref. [4]). Here $\mathbf{H} \parallel c$ and $\mu_0 H = 4.0$ T.

## References


1. T. Shiroka, F. Casola, V. Glazkov, A. Zheludev, A. Revcolevschi, G. Dhalenne, K. Prša, H.-R. Ott, and J. Mesot, *J. Phys.: Conf. Series* **400**, 032089 (2012).
2. M. Kenzelmann, A. Zheludev, S. Raymond, E. Ressouche, T. Masuda, P. Böni, K. Kakurai, I. Tsukada, K. Uchinokura, and R. Coldea, *Phys. Rev. B* **64**, 054422 (2001).
3. F. Casola, T. Shiroka, V. Glazkov, A. Feiguin, G. Dhalenne, A. Revcolevschi, A. Zheludev, H.-R. Ott, and J. Mesot, *Phys. Rev. B* **86**, 165111 (2012).
4. V. N. Glazkov, F. Casola, H.-R. Ott, and T. Shiroka, *Phys. Rev. B* **87**, 054427 (2013).
5. A. A. Tsirlin, I. Rousochatzakis, D. Kasinathan, O. Janson, R. Nath, F. Weickert, C. Geibel, A. M. Läuchli, and H. Rosner, *Phys. Rev. B* **82**, 144426 (2010).
6. T. Giamarchi, Ch. Rüegg, and O. Tchernyshyov, *Nature Phys.* **4**, 198 (2008).
7. S. Sachdev, *Nature Phys.* **4**, 173 (2008).
8. T. Shiroka, F. Casola, V. Glazkov, A. Zheludev, K. Prša, H.-R. Ott, and J. Mesot, *Phys. Rev. Lett.* **106**, 137202 (2011).
9. F. Casola, T. Shiroka, S. Wang, K. Conder, E. Pomjakushina, J. Mesot, and H.-R. Ott, *Phys. Rev. Lett.* **105**, 067203 (2010).
10. S. Wang, E. Pomjakushina, T. Shiroka, G. Deng, N. Nikseresht, Ch. Rüegg, H. M. Rønnow, and K. Conder, *J. Cryst. Growth* **313**, 51 (2010).

# Chapter 4

# Nanoscale imaging, Nanoscale Magnetism

**Head**
Prof. Dr. D. Pescia

**Academic Staff**

| | | |
|---|---|---|
| L. De Pietro | H. Cabrera | D. Zanin |
| Dr. U. Ramsperger | Dr. A. Vindigni | Prof. Dr. M. Erbudak |

**Technical Staff**
Th. Bähler

**Academic Guests**
Prof. Dr. J. Xanthakis, National Technical University (NTU) Athens, Greece, June 20 - 22, 2012

A. Kyritsakis,National Technical University (NTU) Athens, Greece, June 20 - 22, 2012 and September 1 - 30, 2012

Prof. Dr. S. Cannas, November 24 - December 1, 2012

## 4.1 Nanoscale Imaging

### Fundamental Aspects of Near Field-Emission Scanning Electron Microscopy

D. A. Zanin, H. Cabrera, L. De Pietro, U. Ramsperger, A. Vindigni, Th. Bähler, D. Pescia

The desire for a deeper understanding of physical phenomena has always encouraged scientists in the development of new techniques to investigate both the macro- and the microscopic universe. A good example is given by E. Ruska, who in 1933 proposed for the first time a microscope based on a probing beam consisting of electrons instead of light. In electron microscopy, the source of electrons is remote from the target (typically of the order of 1 meter) and the electrons are focused onto a small spot by a sequence of electron optical elements. 50 years later, H. Rohrer and G. Binning introduced a method to achieve atomic resolution using the quantum mechanical tunnel effect to probe the surface, called STM (**S**canning **T**unneling **M**icroscopy), revolutionizing therefore for the second time the world of microscopy. In STM, the source of the primary electrons is at subnanometer distances from the target, so that electrons directly tunnel from the source – a sharp tip – into the target.
Here we present a fundamental study of a technology (Near Field-Emission Scanning Electron Microscopy (NFE-SEM) (also known as the "topografiner") that is somewhat "intermediate" between Electron Microscopy and STM. In NFESEM electrons are emitted from a tip (placed at few tens of nanometers away from the target) via field emission (FE) – electric field assisted quantum tunneling –, impinge and interact with the sample and produce electrons (let us call them Secondary Electrons, SE) which are ejected from the surface and can escape the strong electric field environment existing in the tip-surface region. By scanning the tip parallel to the surface, using the ultra-precise positioning techniques known from STM technology, and measuring the FE and/or SE current, a topographic image of the surface can be obtained, with subnanometer spatial vertical resolution and few nanometers lateral spatial resolution. The bias voltage used in NFESEM is typically some 10 V: NFESEM is therefore a low voltage "scanning electron microscope". It differs from conventional low voltage SEM in that the electron source is positioned locally – in contrast to the remote electron gun used in conventional electron microscopes. This means that NFESEM get rid of all electro/magneto-static lenses required in conventional SEM for focusing the electron beam and that the spot size is limited by the short tip-surface distance. NFESEM also differs essentially from STM. First, the electrons propagate, at least over a short distance, in vacuum and the excitation processes during the interaction with the surface atoms are rather described as scattering process (elastic and/or inelastic) rather than within the tunneling formalism. In addition, the excited electrons are able to escape the NFESM junction, in contrast to the STM junction, and can be used for different purposes (electron spectroscopy, spin polarized electron spectroscopy, etc.). It was the main scope of this year to design and develop a novel instrument where both STM **and** NFESEM could be performed routinely at the **same** location of the target, in order to have a comparison of both technologies at glance.

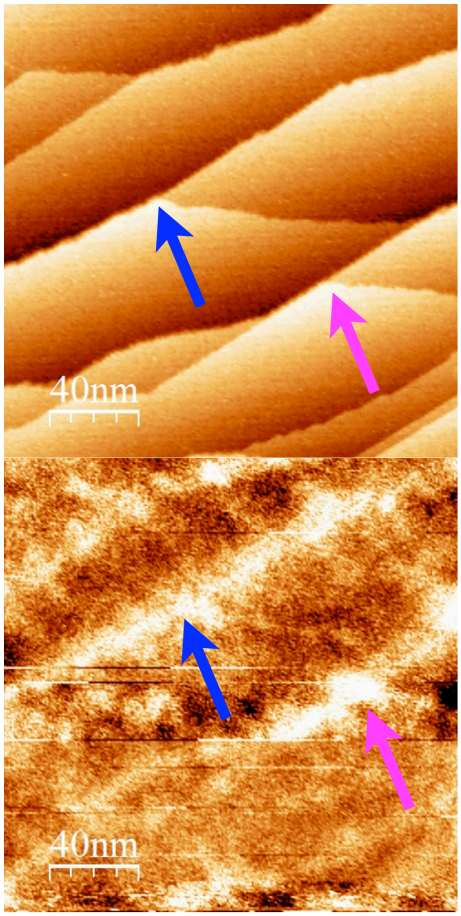


**Figure 4.1:** Top: STM image of a Si(111) surface covered by few monolayers of Fe. In STM-mode, the tunneling current is kept constant while scanning the tip parallel to the surface and the displacement of the tip perpendicular to the surface (typically few 0.1 nm) is recorded. The total displacement in the image is 1.21 nm. For rendering the image, a plane is subtracted, so that the edges of the image are equalized to the same height. Clearly visible are monoatomic steps dividing flat terraces (height of the steps: 0.2 nm), running almost along the diagonal of the image. Two characteristic features are marked with arrows. Bottom: the same area of the sample imaged after retracting the tip to 25 nm distance. The current of the electrons escaping the NFESEM junction is recorded while scanning the field emitter at a constant distance of 25 nm from the surface. The current is plotted using a dark (low current)- bright (high current) scale. The same monoatomic steps are observed (see e.g. the two arrows marking the characteristic features already pointed out in the STM image), although they seem not to be as sharp as in the STM image. However, taking into account that the distance between the STM and the NFESEM mode has changed by about a factor of 100, we would expect a much more pronounced deterioration of the spatial lateral resolution. The persistence of sharp features in the NFESEM mode is still an unresolved problem.

## 4.2 Nanoscale Magnetism

### Domain walls in ultrathin magnetic films and nanowires at finite temperatures

Thomas Michaels, A. Vindigni, D. Pescia

The possibility of inducing domain-wall (DW) motion in magnetic nanowires by means of electric currents has recently renewed theoretical interest in this field. The problem is usually modeled on a micromagnetic approach, but ignoring thermal fluctuations. However, some relevant experimental facts - like the correct order of magnitude of the critical current needed for DW motion - still lack satisfactory explanations. We thus developed a one-dimensional stochastic model for DW dynamics, which allowed us to take into account both thermal fluctuations and external drifts (magnetic field and electric spin-polarized current) simultaneously. We also provided a general theoretical framework, which highlights the crucial role played by thermal fluctuations at the center of DWs. The latter, for example, qualitatively accounts for the shrinking of magnetic domains observed in Fe films on Cu(001) with increasing temperature and the renormalization of the critical current for DW motion in magnetic nanowires at finite temperatures.

# Chapter 5

# Optical and Magneto-optical Spectroscopy

**Head**
Prof. Dr. L. Degiorgi

**Academic Staff**
Dr. C. Mirri A. Dusza

**Administrative Staff**
I. Mettler

## 5.1 High pressure crystalline phases of tellurium: a combined Raman and *ab-initio* study

M. Lavagnini and L. Degiorgi
work in collaboration with P. Postorino, University La Sapienza, Rome, Italy.

Recent investigations of the pressure induced structural evolution in several elements (mostly Chalcogens and Halogens like S, Se, Te, I, and Br) have provided evidence for the onset of a high pressure (HP) incommensurately modulated (IM) lattice arrangement. These findings suggest the idea that the development of aperiodic structures is a common phenomenon in elemental systems under pressure. Moreover, in a variety of those, e.g. I, Br, P, S, Se, and Te, the overall picture is even more intriguing, since applied pressure induces a metallization transition preceding the onset of the IM phase, which suggests a connection of the IM phase with an electronic instability. In this context, Te is a prototype system well suited for an experimental and theoretical investigation of the crystalline and electronic structure stability under pressure. A room temperature study of the high pressure phases of crystalline Te was carried out by combining Raman spectroscopy and Density Functional Theory (DFT) based calculations.

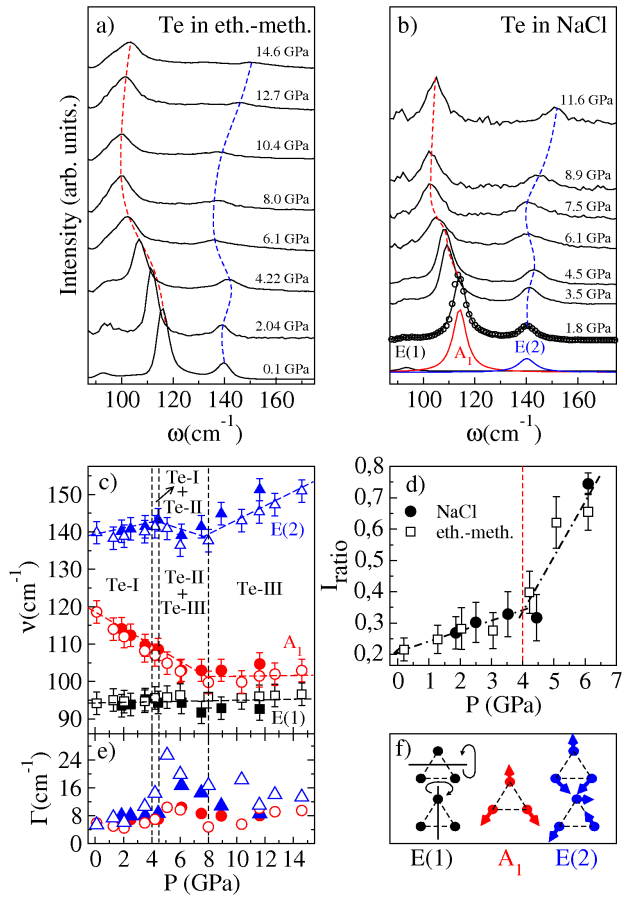


**Figure 5.1:** Te Raman spectra at 300 K and selected pressures (p), in ethanol-methanol (a), and NaCl (b). Best fit curve and phonon contributions for the p=1.8 GPa spectrum are also shown in (b). The p-dependence of the phonon frequencies is displayed in (c) and of the linewidths in (e). Vertical lines in (c) and (e) mark the phase transitions pressures. Panel (d) shows the intensity $I_{ratio} = I[E(2)]/(I[E(1)] + I[A_1])$ vs. pressure dependence. Open (close) symbols in (c), (d) and (e) refer to measurements using ethanol-methanol mixture (NaCl). (f) Color code and atomic displacements for the Raman active modes in Te-I.

Normalized and background subtracted Raman spectra of Te, collected using NaCl and methanol/ethanol are shown in Fig. 5.1 at selected pressure values. According to the standard group theory, the irreducible representation of the optical modes of Te-I is $A_1 + A_2 + 2\,E$. The Raman active modes are: the $A_1$ mode (breathing in the *ab* plane) and the

two doubly degenerate E modes (E(1) *a*- and *b*-axis rotation, E(2) asymmetric stretching mainly along *c*-axis). The latter two modes are also Infrared active since the crystal lacks a center of inversion. In Fig. 5.1b the best-fit curve and the phonon assignment for the Te-I phase are shown as an example for the spectrum at the lowest pressure value, namely 1.8 GPa. The Raman spectrum shows a remarkable pressure dependence, albeit the three-peaks structure is basically preserved over the whole pressure range and the pressure dependence of the experimental phonon spectrum reveals the occurrence of IM phase transitions. Looking at Fig. 5.1c, where the values of the best-fit parameters for frequency and linewidth are shown, three different pressure regions can be identified by the slope change of the observed pressure dependences. Over the 0-4 GPa pressure range, the phonon frequency of the $A_1$ mode (chain breathing) shows a linear softening ($\sim 10$ cm$^{-1}$), whereas the frequencies of the two E modes show a weak increase. Over the same pressure range, a contraction of the *b* lattice parameter is observed, while *c* keeps almost constant, which suggests a progressive weakening of intrachain bonds in favor of interchain atomic interactions. The slope discontinuity of the pressure dependence of the E(2) mode, whose frequency starts to decrease at 4 GPa, marks the appearance of a new crystal phase although, within the 4-7 GPa, the frequency of the $A_1$ phonon is still decreasing and that of the E(1) mode remains almost constant. The narrow pressure range in which Te-I and Te-II coexist (4-4.5 GPa) makes it impossible to determine whether the discontinuity can be ascribed to the Te-I/Te-II transition or to the onset of the Te-III phase. According to previous work, where the Te-II/Te-III coexistence is reported over the 4.5-8 GPa pressure range, the observed softening of the E(2) mode can be ascribed to the structural instability of the Te-II phase that is progressively converted into the rather similar Te-III phase. We observe that larger values of the phonon linewidths (Fig. 5.1e) are found within the coexistence region (4.5-8 GPa), with respect to the other pressure range, as a consequence of the lattice disorder. On further increasing the pressure above 8 GPa, all the phonon modes show a rather regular frequency hardening, indicating that a single, stable phase (Te-III) has finally established.

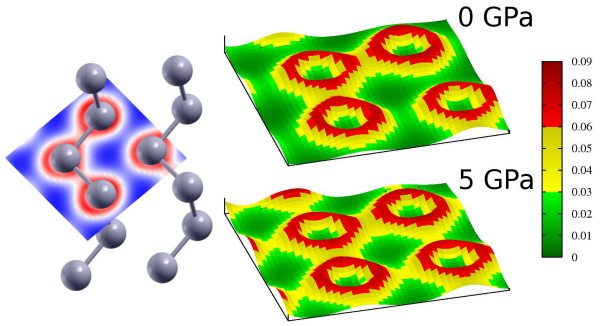


**Figure 5.2:** Valence electron density at 0 and 5 GPa in the Te-I phase over the plane containing 3 atoms along the chain and the closest atom in the adjacent chain.

To gain further insight into the microscopic charge-transfer process, pseudopotential DFT-based calculations have been carried out using the Quantum-Espresso Code. DFT-based calculations show that the metallization process at 4 GPa is due to charge-bridges between atoms belonging to adjacent chains. In particular, our calculations provided also the maps of the valence electron ($5S^2 5P^4$) densities at ambient pressure and 5 GPa, shown in Fig. 5.2. The onset of a bridge of charge density linking the atoms inside the chain and the first neighbor atom in the adjacent chain is pretty clear at P=5 GPa. The metallization transition is therefore the result of the simultaneous lattice symmetrization and charge-transfer processes from intrachain to interchain regions, which enables the mobility of the valence electrons. This is a pressure induced (i.e. density induced) mechanism which closely resembles the intra- to inter-molecular charge transfer processes observed in the metallization transition of molecular elemental systems.

In summary, a high pressure study of crystalline Te, using a combined approach of experimental spectroscopic with *ab initio* calculations, was presented. The DFT calculations well reproduce the experimental data, allowing for an accurate and systematic investigation of the microscopic modifications of both structural and electronic dynamics under lattice compression: the metallization transition is driven by an intra- to inter-chain charge transfer.

## 5.2 An alternative route to charge density wave formation in multi-band systems

M. Lavagnini and L. Degiorgi

work in collaboration with H.M. Eiter and R. Hackl, Walther-Meissner Institut, Garching, Germany, and T. Devereaux, J.-H. Chu and I.R. Fisher, Stanford University, California, U.S.A.

The common view of charge density wave (CDW) formation was originally posed by Kohn. Following Kohn's reasoning, the tendency towards ordering is particularly strong in low dimensions, because the Fermi surface has parallel parts, referred to as nesting. This leads to a divergence in the Lindhard susceptibility, determining the magnitude and direction of the ordering vector $\mathbf{Q}$. This divergence in the electronic susceptibility is conveyed to the lattice via the electron-phonon coupling, so that a phonon softens to zero frequency at $\mathbf{Q}$, and a static lattice distortion develops when the system enters the CDW state; a behavior known as the Kohn anomaly.

However, several publications raise the question as to whether nesting alone is sufficient to explain the observed ordering direction $\mathbf{Q}$, particularly in dimensions higher than one. A central question is whether the selection of the CDW ordering vector is always driven by an electronic instability, or if the ordering vector could instead be determined by a lattice distortion driven by some other mechanism exploiting the role of the electron-phonon coupling. In the latter case, the selected ordering vector would not necessarily nest the Fermi surface. The importance of strongly momentum dependent electron-phonon coupling on CDW formation was pointed out in the literature, where the relevance of the Fermi surface for determining the ordering vector was indeed found to decrease as the coupling strength increases.

For exploring a possible relation between anisotropic electron-phonon coupling and CDW ordering selection, it is desirable to map out the coupling strength in momentum space. For certain types of phonons, the electron-phonon matrix element is proportional to the electron-photon matrix element from Raman spectroscopy. As a result, Raman spectroscopy, which efficiently projects out different regions of the Brillouin zone with different photon polarizations, can provide an indirect method for investigating the momentum-dependence of the electron-phonon coupling in a system. We analyze data from Raman experiments and the related selection rules for the CDW $ErTe_3$ material ($T_{CDW1}$=265 K, followed by a second one at $T_{CDW2}$=155 K) and demonstrate that the lifting of band degeneracies enhances the light-scattering sensitivity and, concomitantly, the electron-phonon coupling at ordering vectors that do not coincide with those predicted by nesting alone.

Figure 5.3 depicts the electronic Raman response of $ErTe_3$ at various temperatures below $T_{CDW1}$. The spectra at 262 K (Fig. 5.3*A*) are isotropic, rise almost linearly between 800 and 3500 $cm^{-1}$ and finally become flat. Upon lowering the temperature there is a transfer of spectral weight in the $aa$ spectrum from low to high energies (Fig. 5.3*B* and *C*). At 8 K (Fig. 5.3*C*), there is a relatively weak new structure in the $cc$ spectrum in the range 500-1200 $cm^{-1}$. The insets in Fig. 5.3*C* highlight the temperature dependences of the $aa$ and $cc$ polarized spectra right above and below $T_{CDW1}$ and $T_{CDW2}$, respectively. In either case, spectral weight is progressively suppressed below the gap edges and piles up above. There is a full anisotropy without any leakage between the two orthogonal $aa$ and $cc$ directions. We identify the edges with twice the maximum gap energies of the first and the second CDW, $2\Delta_1$=2800 $cm^{-1}$ and $2\Delta_2$=800 $cm^{-1}$, respectively, in agreement with ARPES findings.

The electronic Raman response including the selection rules can be derived directly from the band structure and the momentum dependences of the CDW gaps using the formalism of Ványlos and Virosztek. The intensity of the light scattering for different polarization combinations (Raman vertices) are mainly determined by the curvature of the electronic dispersion. If we neglect hybridization, the Raman vertices are almost featureless with little highlights in particular regions of the Fermi surface, as illustrated in Fig. 5.4*A*-*C* for the $aa$, $cc$ and $ac$ polarizations. Upon including hybridization, the band degeneracy is lifted, and the two bands exhibit strong curvatures. As a result, the vertices become highly focused along the diagonals of the Brillouin zone for parallel polarizations, as shown in Fig. 5.4*D*, *E* and *G*, *H* for both bands, because of nearly singular band curvature. This focusing enhances the light scattering precisely at the Fermi surface points connected by the CDW ordering wavevectors.

The focusing effect on the electronic spectra can be demonstrated directly via the weak-coupling Raman response. We assume that at $T < T_{\mathrm{CDW2}}$ the two perpendicular CDWs with ordering vectors $\mathbf{Q}_1$ and $\mathbf{Q}_2$ have fully developed gaps

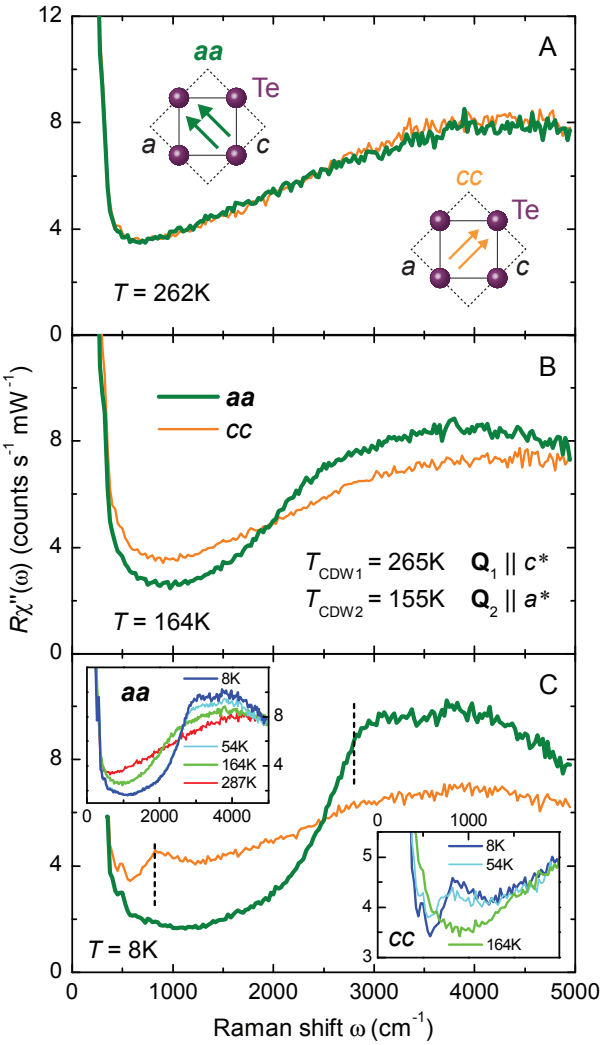


**Figure 5.3:** Temperature dependence of the high energy Raman spectra in $ErTe_3$. (*A*) At 262 K there is no difference in the electronic excitations at high energy for both polarizations. The insets sketch the incoming and scattered photon polarizations. (*B*) At 164 K the anisotropy between the two polarizations is already well resolved. (*C*) In the limit $T \to 0$ the electronic gaps with edges at 800 and 2800 $cm^{-1}$ (dashed lines) for both CDWs are fully developed. The upper left and lower right insets show the temperature dependences of both CDW gaps, using the same colour-code.

$\Delta_1$ and $\Delta_2$, respectively. The $\mathbf{Q}_1$ and $\mathbf{Q}_2$ vectors connect the corners of the electron pocket around the $\Gamma$ point with the corners of the hole pockets (Fig. 5.4). The response for the $aa$, $cc$, and $ac$ polarization orientations is shown in Fig. 5.4*J*-*L*. No mixing can be observed in the spectra with parallel polarizations (panels *J* and *K*). In the $ac$ configuration both gaps are in principle visible (panel *L*), but the expected intensity is three orders of magnitude smaller than in $aa$ and $cc$ and cannot be observed in the experiment.

We thus identify two cooperating effects determining the overall selection of the ordering vector: (i) The system gains energy by gapping the band degeneracy points on the Fermi surface where the Raman selection rules indicate substantial fluctuations with fourfold symmetry above $T_{CDW1}$. (ii) Since the electron-phonon coupling vertex is proportional to the Raman vertex for stress phonons, both quantities are enhanced near band degeneracies. Hence, while electron-phonon coupling is known to be important in CDW systems, we identify on a microscopic basis the focusing effect to be a more generic paradigm for multiband materials. As a future outlook, it seems particularly interesting to explore this novel scenario in the proximity of superconductivity, eventually competing or coexisting with CDW order. Moreover, it would be intriguing to address in a wider context the effects of band hybridization in multi-band materials such as the iron-based superconductors, in which density-wave order and superconductivity interplay on a microscopic scale.

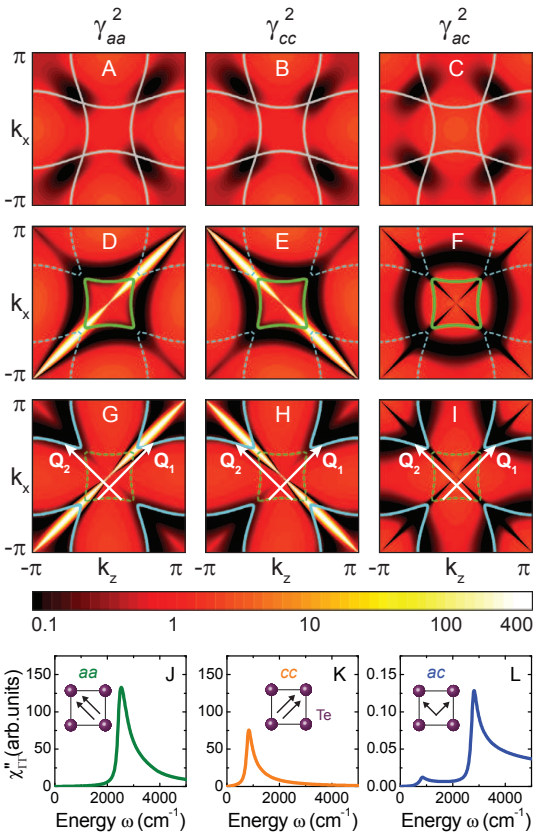


**Figure 5.4:** Theoretical prediction for the Raman vertices and spectra of $ErTe_3$. (*A*-*I*) All vertices are derived from the band structure. (*A*-*C*) The first row shows the vertices without 2D coupling and the corresponding Fermi surfaces. (*D*-*F*) Raman vertices for the bands corresponding to the central part of the Fermi surface (green) and (*G*-*I*) to the outer part (light blue). The focusing effect due to the lifted degeneracy enhances the vertices by more than two orders of magnitude as indicated by the color code. The ordering vectors are displayed in the third row. (*J*-*L*) All spectra are calculated at temperatures lower than $T_{CDW2}$ and include both CDWs. (*J*, *K*) For parallel polarizations one observes only the CDW with ordering vector perpendicular to the light polarizations. The response of the respective orthogonal CDW is too weak to be visible. (*L*) For $ac$ polarization both gaps can be resolved but the overall intensity is more than three orders of magnitude lower than that in the two other configurations. This is well below the detection limit, and, in fact, no signatures of the gaps can be observed experimentally in $ac$ polarization.

# Chapter 6

# Solid-State Dynamics and Education

**Head**
Prof. Dr. A. Vaterlaus

**Academic Staff**

| | | |
|---|---|---|
| Dr. Yves Marc Acremann | Dr. Audra Baleisis | Andreas Fognini |
| Andreas Lichtenberger | Dr. Thomas Uli Michlmayr | Martin Mohr |
| Gerard Salvatella Orgilles | Dr. Guillaume Schiltz | Dr. Clemens Wagner |

**Academic Guests**

| | |
|---|---|
| Christoph Wetli | FS12 |
| Rafael Gort | FS12 |
| David Perriard | FS12 |

**Technical Staff**
Thomas Bähler

## 6.1 A kinematics concept/misconception diagnosis test

A. Lichtenberger

A majority of students have difficulties to understand physics concepts (Halloun & Hestenes, 1985; Hake (1998)). Students often attend classes with solid misconceptions. In order to adapt to the proper concepts not only the concepts have to be learned but also the misconceptions have to be removed (Wagner & Vaterlaus, 2011). This requires the diagnosis of student concepts and misconceptions.

We have developed a diagnostic test, which identifies the student concepts and misconceptions in kinematics at the high school level. The test can be used as an element of formative assessment. We have identified the following seven basic kinematics concepts:

- C1: Velocity as a rate
- C2: Velocity as a vector
- C3: Vector addition of velocities
- C4: Displacement as area under the curve in a velocity-time-diagram
- C5: Acceleration as a rate
- C6: Acceleration as a vector
- C7: Change in velocity as area under the curve in an acceleration-time-diagram

To every concept, a set of corresponding misconceptions is assigned. The concepts as well as the misconceptions have been verified by asking the students open questions and by analysing their answers. They have been confirmed by experts and are in good agreement with concepts identified elsewhere (Hestenes et al., 1992).

The test consists of 56 multiple-choice items on kinematics, each item containing one right answer and three or four distractors. Every distractor has been chosen in a way that it can be associated with one misconception. This is different from other kinematics tests (Hestenes et al., 1992; Beichner, 1993). Thus the test not only uncovers student concepts but also student misconceptions. The items can be furthermore divided into three levels of abstraction: items with images, e.g. stroboscopic pictures (1), items with diagrams (2), items with tables of values (3).

For test validation interviews with students have been conducted and experts have been asked to revise the test. In addition test theory and confirmatory factor analysis have been applied to the data collected from 285 students.

The kinematics diagnosis test is a useful instrument for the teacher as well as for the students to get feedback about the concept/misconception levels. Every student receives two diagrams. One illustrates the percentages of items solved correctly for each of the seven concepts and the other shows which misconceptions are still present (Fig. 6.1). The teacher gets feedback about the performance of the class, which may help him to amend his instruction.

We have used the validated test in a preliminary study as pre- and posttest in mechanics courses at two high schools

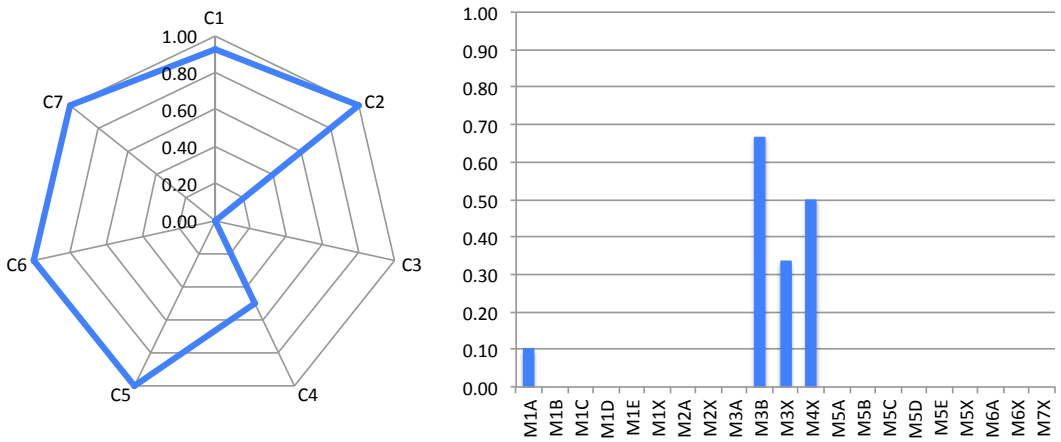


**Figure 6.1:** Diagrams illustrating the concept levels (left) and misconception levels (right) of a student.

in Switzerland (56 students). The average normalized gain has been found to be 0.45. This value is similar to the results found by Hake (1998) for physics courses with interactive engagement. The test contains 10 extra items about basic mathematics. Each of these items refers to a corresponding item in kinematics. The test data has revealed a high correlation between the mathematics and kinematics items.

In summary, we have developed and validated a diagnosis test, which identifies the student concepts and misconceptions in kinematics at the high school level. It can be used in formative assessment or as a pre- and posttest to provide information about the effectiveness of instruction.

**References**

Beichner, J. R. (1993). Testing student interpretation of kinematics graphs. Am. J. Phys. 62 (8): 750-762.

Hake, R. R. (1998). Interactive-engagement versus traditional methods: A six-thousand-student survey of mechanics test data for introductory physics courses. Am. J. Phys. 66 (1): 64-74.

Halloun, I. A. & Hestenes, D. (1985). The initial knowledge state of college physics students. Am. J. Phys. 53 (11): 1043 -1055.

Hestenes, D., Wells, M., & Swackhamer, G. (1992). Force concept inventory. The Physics Teacher, 30, 141-158.

Wagner, C. & Vaterlaus, A. (2011). A Model of Concept Learning in Physics. Conference Proceedings, Frontiers of Fundamental Physics FFP12. http://www.fisica.uniud.it/ ffp12/proceedings.html.

## 6.2 E-Learning and teaching support

G. Schiltz

**Strategic activities**

19 lectures have been supplemented by the learning management system Moodle in 2012. 12 introductory lectures (service and internal), 3 teacher training courses and 4 MSc lectures reached more than 2000 students. Moodle was mainly used to support the course organization and to serve as a repository for course material. For some lectures, however, supplementary pedagogical scenarios, such as self-assessment tests, formative evaluations and collaborative tasks have been set up.

Summary podcasts (audio/visual weekly summary) and peer instruction (via concept questions) are now adapted by a growing number of faculty members. More than 60 podcast episodes have been produced in 2012. Peer instruction was extensively used by 6 lecturers and reached a total of 1990 students (Fig. 6.2).

**Innovedum projects**


**Figure 6.2:** Peer instruction in „Physik II".

In 2012 a new project has been granted by Innovedum. Rainer Wallny is building a database of concept questions (Fig. 6.3), which can be used by other lecturers as well.

**Promotion and Network**

The teaching activities pursued at the department have been communicated to a greater public (4 presentations at international conferences, 4 community presentations).

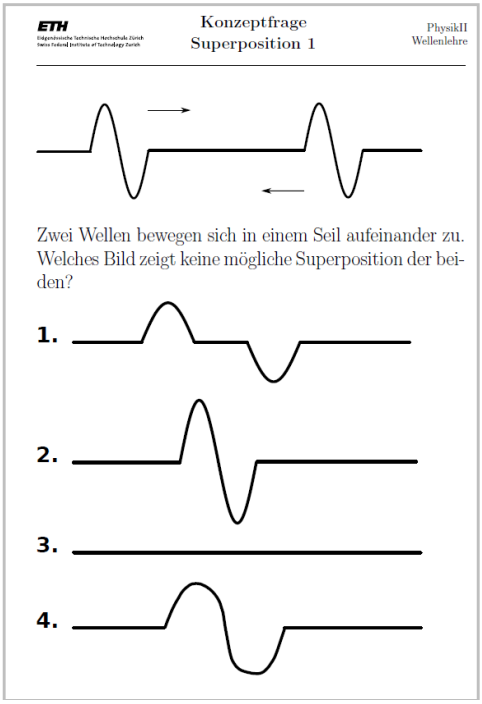


**Figure 6.3:** Concept question

## 6.3 Simulation of conceptual change

C. Wagner

The analysis of misconceptions and the difficulty of conceptual change have been of major interest in physics education research during the past few decades. Although many different strategies have been suggested conceptual change is often unsuccessful. It appears that there is no study in the literature, which shows that misconceptions are fully extinguished and replaced by new scientific concepts. Most investigators report that the old misconceptions are still alive and only peripheral conceptual change has taken place.

In order to obtain a better understanding of the interaction between the presence of misconceptions and new concepts during conceptual change we have constructed a mathematical model. It consists of two differential equations describing the dynamics of the concept level c and misconception level m as well as their interactions. However, these variables are latent variables and have therefore no direct access. In order to measure the levels one has to design problem sets, which have to be solved by the students. Hence, read out functions, $c_{\mathrm{T}}$ and $m_{\mathrm{T}}$, have to be designed, in order to estimate the latent levels from the test results.

Depending on the problem students have three different possibilities to answer a question. If they answer correctly they apply the concept $c$. If they choose the respond due to the misconception the answer is related to the $m$-level. Finally, if the student has no clue how to solve the problem the answer is dominated by the term $(1-m)(1-c)$. However, there also occur interferences between the read out of the concept and the misconception, which we account for by the following equations.

$$\begin{aligned} c_{\mathrm{T}} &= c(1-\xi m)+\zeta(1-m)(1-c) \\ m_{\mathrm{T}} &= m(1-(1-\xi)c)+\zeta(1-m)(1-c) \\ n_{\mathrm{T}} &= (1-c)(1-m)(1-2\zeta) \end{aligned}$$

The concept read out function is displayed in Fig. 6.4. If the misconception and the concept levels are both high, the student faces an internal conflict. The outcome of this phenomenon is accounted for by the parameter $\xi$. Just by chance students with no clue how to solve the problem can select the correct answer. It motivates the term $\zeta(1-m)(1-c)$. The same also holds for the misconception answer. The sum of all three read out functions is of course one. The read out function allows for properly exploring experimental data. Time courses of misconception levels often show

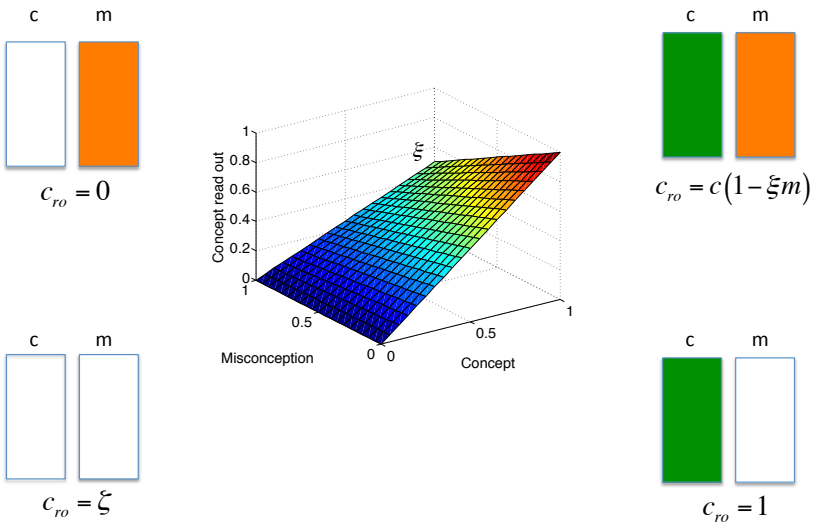


**Figure 6.4:** Concept read out function depending on the latent concept and misconception levels for $\xi = 0.5$ and $\zeta = 0$. The concept read out level is given for $(c, m) = (0, 0)$ lower left, $(0, 1)$ upper left, $(1, 1)$ upper right and $(1, 0)$ lower right.

an unexplainable decay during the teaching phase although they are high again shortly after the learning units. This phenomenon can now be explained in terms of the read out function. The decay is mainly due to the read out. In contrast, the internal level stays high and determines the long-term behavior of the student.

## 6.4 Productive practice

C. Wagner

Productive practice is a new way to design exercises in Mathematics. It is based on 4 tenets. First, the problems should make sense for the student. Hence the student realizes while solving the problems that he achieves a better understanding of the content. Second, the problems have to be designed in a way that students can make their own discoveries. Problems also should allow for different solution paths. Third, the problems have to be reflexive. For example, if a series of solutions has to be calculated it is easy to identify solutions, which do not fit into the series. Fourth, the problems show an increase in difficulty so the each student can work until he has reached his own level. We have transferred these tenets to Physics in order to design exercises for concept learning. Different basic design principles were identified. In order to get a better understanding of a system one can, for example, explore the parameter space or part of it. Another principle is to invert problems. For example, an electric field vector is given at point P and the student has to locate two charges, which lead to the given solution. Finally, one extends the system in a stepwise manner so that the solution consists of a series. An example hereof is to compute the electric field at the origin while one change is located on the x-axis at $-1\,\mathrm{m}$. Then, one adds additional charges equally distributed on the x-axis. Finally, the number of charges tends to infinity. Of course, this latter approach has to be applied with care, so that the series converges. We have designed a set of productive practice problems in electrostatics and are now in the validation phase. We challenged students and experts with the problems and received a positive feedback in the majority (Fig. 6.5). We conclude that the experts enjoyed solving the problems and characterized them as challenging.

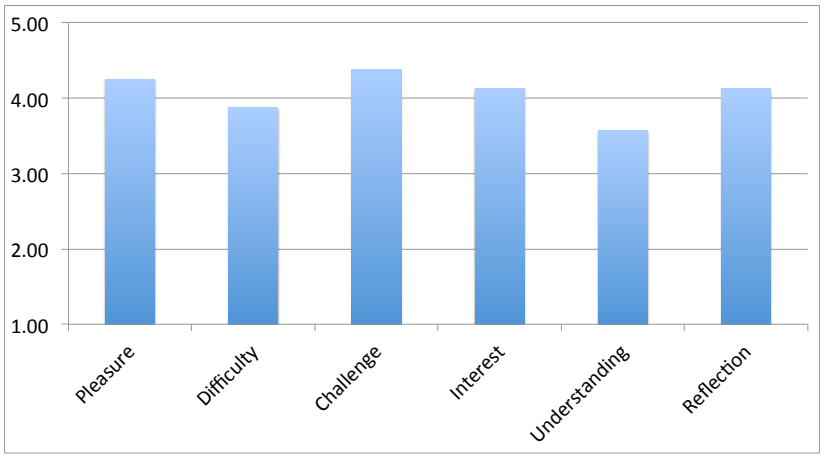


**Figure 6.5:** Results of an anonymous survey using a 5-point Likert scale among experts (8 PhD-students or postdocs) about their opinion concerning problems (number of problems: 4) of productive practice in electrostatics.

Further investigations will have to provide explanations, why the experts think that the understanding is not fostered to the desired extent by the given exercises. Moreover, our goal is to explore how these problems can indeed enhance conceptual understanding of students.

## 6.5 Spin and demagnetization dynamics on the fs-timescale probed by energy and angular resolved photoemission

Y. Acremann

Demagnetization can be achieved on the 100 fs timescale by heating up a ferromagnet with an ultrashort laser pulse. Since the first observation in 1996 by Beaurepair *et al.* no unifying explanation regarding the origin of this phenomenon could establish. Measurements were done by magneto optical Kerr effect (MOKE) and X-ray magnetic circular dichroism (XMCD). Another approach to determine the magnetic state of a ferromagnet is to use photoemission of electrons with spin analysis which can be done by a Mott detector. This approach has the advantage to be a very direct measurement or the magnetization: Electrons which form the magnetic moment are extracted and their spin polarization is measured. Therefore it is not influenced by electronic effects caused by the heating laser pulse. All the mentioned techniques use an experimental setup with variable time-delayed pump and probe pulses for excitation and immediate measurement.

A novel, more efficient electron spin detector based on spin dependent low electron energy diffraction (SPLEED)

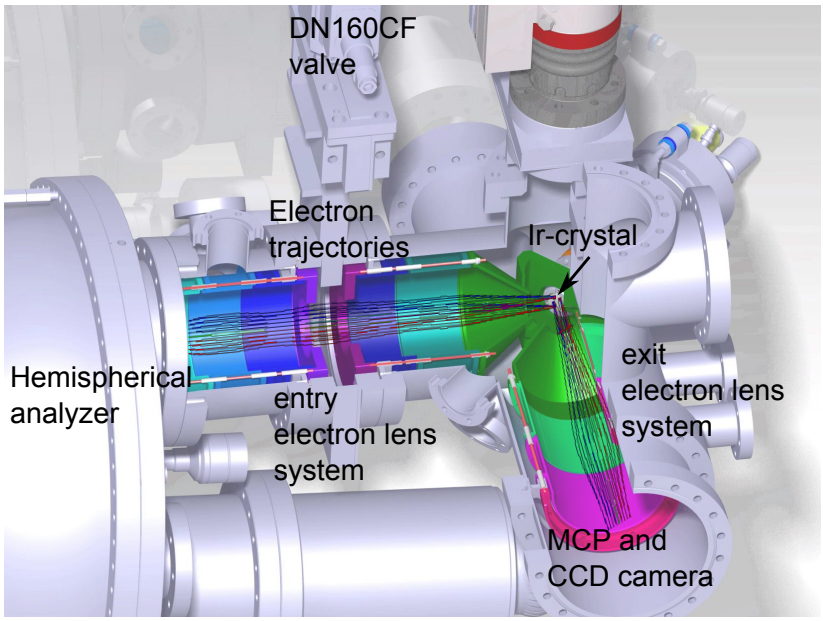


**Figure 6.6:** Electron trajectories trough a cut-open SPLEED detector. The electrons exiting the hemispherical energy analyzer enter an imaging lens system and scatter under an angel of 45 ° on an Ir crystal. The scattering process is energy and spin dependent. The exit lens system images the output of the energy analyzer onto a detector consisting of multichannel plate, phosphorous screen and a CCD camera.

was developed by the group of G. Schönhense at the University of Mainz, Germany and successfully commissioned and optimized at the Swiss light source (SLS), Villigen and at our laboratory. It has been used for first experiments at the free electron laser facility (FLASH) in Hamburg. One of the benefit of this novel spin detection system is the two orders of magnitude higher figure of merit in comparison with a Mott detector. Its imaging capabilities allow for parallel detection of angel and energy if combined with a hemispherical energy analyzer.

As a laboratory source for ultrashort pump probe experiments a pulsed 800 nm laser system with 1.0 mJ pulse energy and 10 kHz repetition rate was acquired in the year 2012. An optical parametric amplifier (OPA) allows for excitation with various photon frequencies. A fourth harmonic generator (FHG) provides the photon energy needed for photoemission into vacuum.

### References

E. Beaurepaire, J.-C Merle, A. Daunois, and J.-Y. Bigot, Ultrafast Spin Dynamics in Ferromagnetic Nickel, Phys. Rev. Lett. **76**, 4250–4253 (1996).

# Chapter 7

# Quantum Device Lab

**Head**
Prof. Dr. A. Wallraff

**Academic Staff**

| | | |
|---|---|---|
| Dr. A. Abdumalikov | Dr. M. Allan | Dr. M. Baur |
| S. Berger | R. Ebert | C. Eichler |
| Dr. A. Fedorov | Dr. S. Filipp | Dr. J. Fink |
| T. Frey[1] | L. Heinzle | C. Kern |
| C. Lang | S. Miesch | J. Mlynek |
| M. Oppliger | M. Pechal | Dr. G. Puebla-Hellmann |
| Dr. K. Reim | Y. Salathe | M. Stammeier |
| L. Steffen | T. Thiele | A. van Loo |

[1] joint PhD student with Prof. Dr. K. Ensslin, ETH Zürich, Switzerland

**Master Students**

| | | |
|---|---|---|
| R. Barmettler | J. Govenius | D.-D. Jarausch |
| K. Juliusson | P. Kurpiers | Y. Liu |
| M. Peterer | A. Stocklauser | |

**Technical Staff**

| | | |
|---|---|---|
| H. Aeschbach | S. Arnold | S. Däster |
| C. Heidegger | J. Lütolf | |

**Administrative Staff**

| | |
|---|---|
| Dr. F. Bay | G. Strahm |

## 7.1 Exploring quantum microwave radiation and its entanglement with a superconducting qubit using linear detectors

C. Eichler, C. Lang, D. Bozyigit, J. M. Fink, J. Govenius, S. Filipp, and A. Wallraff

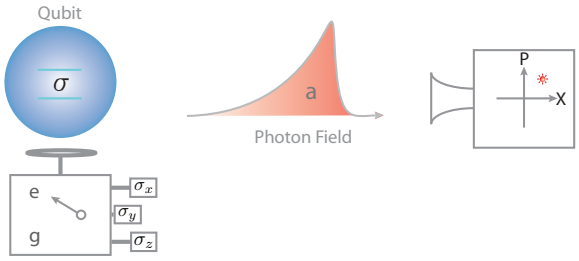


**Figure 7.1:** Sketch of the measurement scheme.

Propagating photons are ideal carriers for distributing entanglement between distant matter systems in a quantum network. Entanglement between photons and stationary qubits has thus far been exclusively studied at optical frequencies with single atoms or electron spins. However, rapid progress in the development of superconducting circuit based quantum technologies also renders propagating microwave photons an attractive quantum information carrier. A major obstacle in measuring quantum correlations between superconducting qubits and itinerant radiation has thus far been the limited detection efficiency at microwave frequencies. In our experiments we have overcome this problem by using a quantum limited amplifier, which significantly improves the signal-to-noise ratio. In combination with novel tomography methods [1], this allows us to measure quantum correlations between itinerant microwave radiation and a stationary qubit with high fidelity [2].

In our experiments, we use the controlled interaction between a superconducting qubit and a microwave radiation field to create entangled Bell states of the form $|g1\rangle + |e0\rangle$. Here, $g$ and $e$ label ground and excited state of the qubit and $0, 1, ...$ the photon numbers of the propagating field. We resolve the entanglement by measuring correlations between the qubit Bloch vector components $\langle\sigma_i\rangle$ and the quadrature components $X$ and $P$ of the photon field, see Fig. 7.1. In the $\sigma_z$ basis, we find a higher probability of observing the qubit in its ground state at large measured field amplitudes [blue region in Fig. 2(a)(i)] which demonstrates that a photon emission is associated with the qubit to be detected in the ground state. We distinguish the quantum superposition state from a classically correlated state by analyzing the equatorial Bloch vector components $\langle\sigma_x\rangle$ and $\langle\sigma_y\rangle$ vs. $X$ and $P$ [Fig. 7.2(a)(ii)-(iii)]. Our measurement record clearly shows the expected phase dependence between the qubit and the field. Based on these measured correlations and the photon field statistics we reconstruct the full density matrix $\rho$ of the joint system with high fidelity F = 0.83 compared to the ideal Bell state [Fig. 7.2(b)]. The absence of any higher photon number state populations verifies that we have entangled the qubit with no more than a single microwave photon.

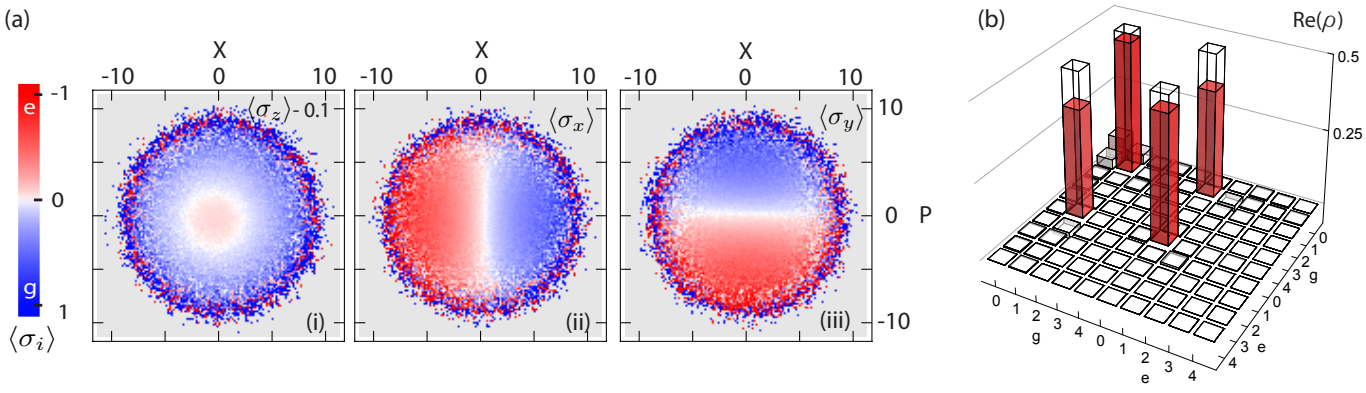


**Figure 7.2:** (a) Bloch vector components $\langle\sigma_i\rangle$ of the qubit conditioned on the photon field quadrature measurements $X$ and $P$. (b) Real part of the measured (colored bars) and ideal (wireframes) density matrix $\rho$.

[1] C. Eichler, D. Bozyigit, and A. Wallraff. *Phys. Rev. A.*, **86**, 032106 (2012).

[2] C. Eichler, C. Lang, J. M. Fink, J. Govenius, S. Filipp and A. Wallraff. *Phys. Rev. Lett.*, **109**, 240501 (2012)

## 7.2 Quantum gates and algorithms explored in superconducting circuits

L. Steffen, M. Baur, A. Fedorov, S. Filipp, M. P. da Silva, and A. Wallraff

### 7.2.1 Implementation of a Toffoli gate with superconducting circuits

The Toffoli gate is a three-qubit operation that inverts the state of a target qubit conditioned on the state of two control qubits. It enables universal reversible classical computation, forms a universal set of gates in quantum computation together with a Hadamard gate and is also a key element in quantum error correction schemes. In our experiment [1], we demonstrated the implementation of a Toffoli gate with three superconducting transmon qubits coupled to a microwave resonator as shown in Fig. 7.3 (a-d). By exploiting the third energy level of the transmon qubit, the number of elementary gates needed for the implementation of the Toffoli gate has been greatly reduced in comparison to theoretical proposals using two-level systems only. To characterize the process matrix $\chi$ we performed full process tomography, see Fig. 7.3 (e,f). For this approach we used a maximum-likelihood procedure to correct for unphysical properties of the reconstructed process matrix $\chi$. To gain an accurate alternative estimation of the process fidelity without resorting to a maximum-likelihood procedure, we implemented Monte Carlo process certification (see section 7.2.2). The gate fidelity evaluated this way is found to be $68.5 \pm 0.5$ %. These results reinforce the potential of macroscopic superconducting qubits for the implementation of complex quantum operations and point at the possibility to implement quantum error correction schemes.

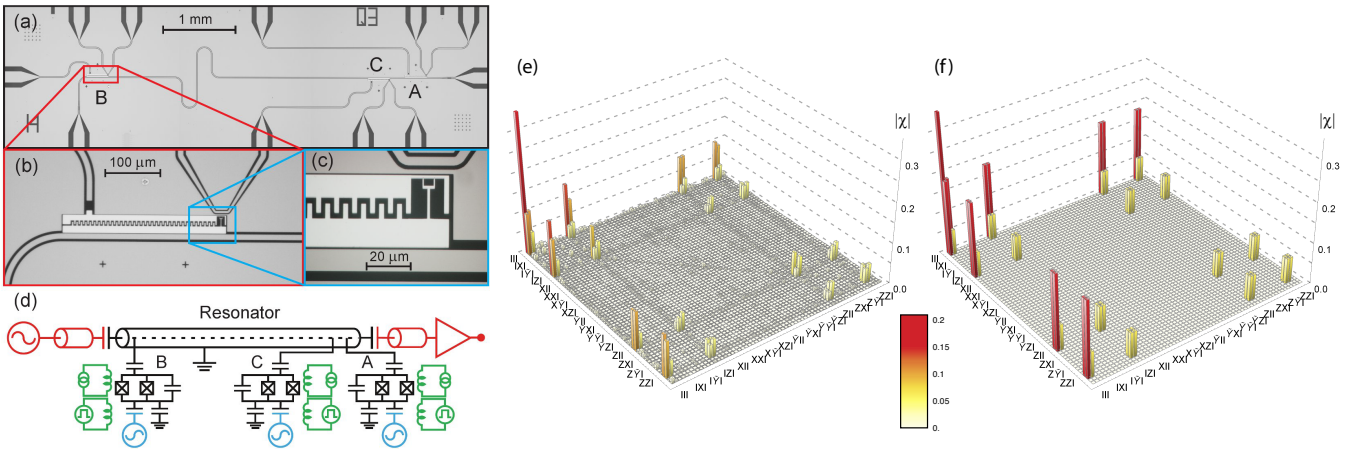


**Figure 7.3:** (a-d) Sample used in the quantum computing experiments. (a) Micrograph of the chip with three superconducting qubits coupled to a coplanar waveguide resonator with individual local microwave and magnetic flux-bias lines for each qubit. (b) and (c) show a close up of qubit B. (d) Simplified circuit diagram of the chip. (e-f) Absolute values of the experimental and ideal process matrix $\chi$ of the Toffoli gate [1].

### 7.2.2 Experimental Monte Carlo quantum process certification

Tomography is the main method used for measuring the fidelity of an experimentally implemented quantum process. However, it is a very inefficient method since the number of measurements as well as the time needed for the data post-processing scale exponentially with the number of qubits. With the ongoing experimental progress and growth in system size, quantum process tomography will soon become infeasible in state-of-the art experiments. Nevertheless, the task of certifying how an experimental implementation of a process compares to the corresponding ideal process is crucial in any quantum system. A more practical approach to determine the fidelity of an experimental quantum process has recently been proposed, where the experimental data is compared directly to an ideal process using Monte Carlo sampling. The significant advantage of Monte Carlo process certification is that the number of measurements needed to be performed to obtain some desired accuracy depends only polynomially rather than exponentially on said accuray and not on the size of the system.

We realized an experimental implementation of this scheme in a circuit quantum electrodynamics setup [2] to determine the fidelity of two qubit gates, such as the CPHASE- and the CNOT-gate, and three qubit gates, such as the Toffoli gate and two sequential CPHASE-gates. By comparing the obtained fidelities with the ones obtained from quantum process tomography, we find that all estimates are consistent, while Monte Carlo process certification gives more accurate estimates of the fidelity with fewer measurements.

### 7.2.3 Benchmarking a quantum teleportation protocol in superconducting circuits using tomography and an entanglement witness

Teleportation of a quantum state may be used for distributing entanglement between distant qubits in quantum communication and for quantum computation. We demonstrate the implementation of a teleportation protocol, up to the single-shot measurement step, with superconducting qubits coupled to a microwave resonator [3]. Using full quantum state tomography and evaluating an entanglement witness, we show that the protocol generates a genuine tripartite entangled state of all three qubits. Calculating the projection of the measured density matrix onto the basis states of two qubits allows us to reconstruct the teleported state. Repeating this procedure for a complete set of input states we find an average output state fidelity of the teleportation process of $86\ \%$. This suggests that full teleportation is likely to become possible in the near future with superconducting circuits by also implementing a high fidelity single-shot readout technique.

[1] A. Fedorov, L. Steffen, M. Baur, M. P. da Silva, A. Wallraff, Nature **481**, 170 (2012)

[2] L. Steffen, M. P. da Silva, A. Fedorov, M. Baur, A. Wallraff, Phys. Rev. Lett. **108**, 260506 (2012)

[3] M. Baur, A. Fedorov, L. Steffen, S. Filipp, M. P. da Silva, A. Wallraff, Phys. Rev. Lett. **108**, 040502 (2012)

## 7.3 Demonstrating W-type entanglement of Dicke-states in resonant cavity quantum electrodynamics

J. A. Mlynek, A. A. Abdumalikov Jr, J. M. Fink, L. Steffen, M. Baur, C. Lang, A. F. van Loo, and A. Wallraff

One important key characteristics of a non-classical physical system is entanglement. For a system containing three qubits two important classes of entangled states are GHZ- and W-states. The first class consists of superposition states between $|000\rangle$ and $|111\rangle$ and the second one arises when a single excitation is symmetrically shared between three qubits, i.e. in an equal superposition between $|001\rangle$, $|010\rangle$ and $|100\rangle$.

In our experiment [1] we have exploited the resonant interaction between three superconducting transmon-type qubits and a microwave transmission line resonator to show that a W-state can be generated with high efficiency in this system by harnessing its collective dynamics. Interestingly, our method also benefits from the $\sqrt{N}$-nonlinearity of the coupling strength between N qubits and a single field mode. Thus in contrast to many entangling gates our scheme is actually faster for a larger number of qubits and thus also is expected to be less affected by dephasing and relaxation.

To generate the W-state we first populate the resonator with a single photon by using a single qubit vacuum Rabi $\pi$-pulse. Then the two remaining qubits are also tuned into resonance. The single photon now has equal probability to be absorbed by each of the three qubits. Our lack of knowledge about which qubit the photon finally excites, naturally leads to a W-type entangled state.

We use full quantum state tomography to characterize the degree of entanglement generated (see figure 7.4). To better understand the limitations of our collective method we also employ a procedure, in which the excitation is distributed sequentially by tuning the qubits in and out of resonance one after another. In fact this method leads to a higher fidelity, which suggests that the main limitation in the collective approach is due to on-chip crosstalk among the flux lines, which are used for fast tuning of the qubit transition frequencies.

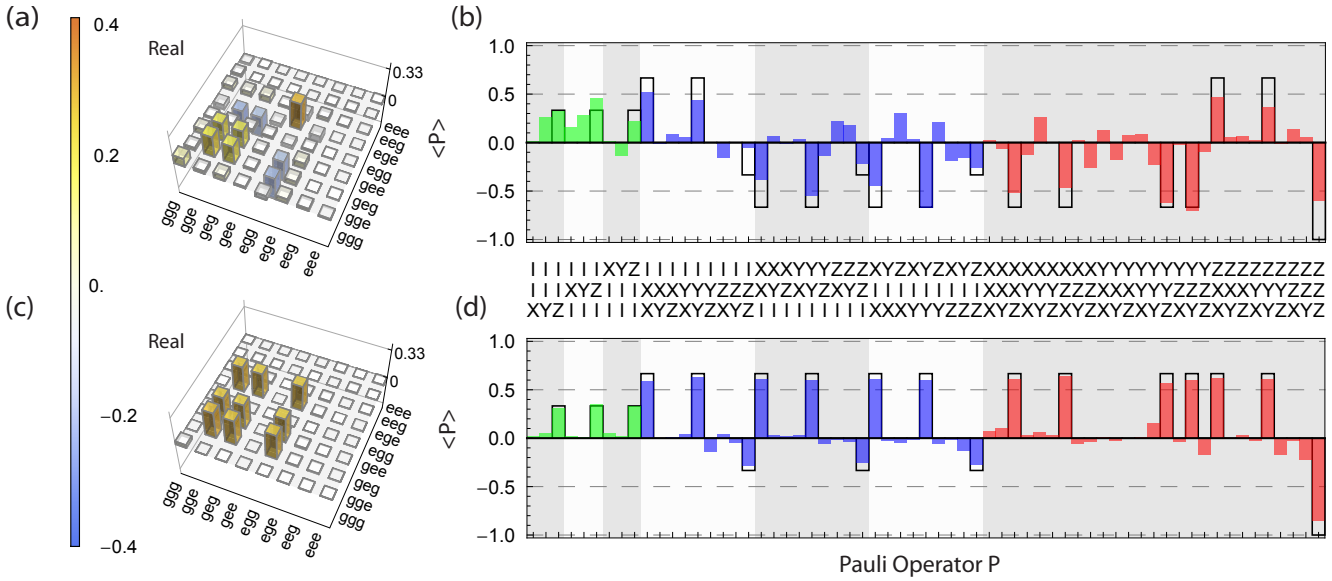


**Figure 7.4:** Real part of the density matrix of the W-state for (a) the collective approach and (c) the sequential approach. (b/d) are Pauli sets for the collective/sequential approach, respectively.

[1] J. A. Mlynek, A. A. Abdumalikov Jr, J. M. Fink, L. Steffen, M. Baur, C. Lang, A. F. van Loo and A. Wallraff, Phys. Rev. A **86**, 053838 (2012)

## 7.4 Geometric phases in circuit QED

S. Berger, M. Pechal, S. Pugnetti, A. A. Abdumalikov Jr., J. M. Fink, L. Steffen, J. A. Mlynek, A. Fedorov, A. Wallraff, and S. Filipp

When a quantum mechanical system evolves under a time-dependent Hamiltonian, it acquires not only the well-known dynamic phase, which is the time-integral of the energy of the system, but also a geometric phase. As indicated by its name, it is of a purely geometric nature in that it solely depends on the trajectory of the quantum system in state space.

One way to measure geometric phases is to employ a superposition of ground and first excited state of a two-level system (a qubit). In previous studies [1], we have observed geometric phases in a Cooper pair box, a superconducting quantum system with large anharmonicity. In this system, the energy levels defining the qubit are well separated from higher energy levels. To explore the effects of higher energy levels, we make use of a superconducting transmon-type qubit with low anharmonicity. We measure the contribution of the second excited state to the geometric phase (Fig. 7.5a) and find very good agreement with theory treating higher levels perturbatively [2]. Furthermore, we quantify non-adiabatic corrections to the geometric phase by decreasing the manipulation time in order to optimize our geometric gate. Geometric phases have also been shown to be resilient against adiabatic field fluctuations. We are currently investigating the resilience of the geometric phases against noise in view of potential applications for quantum information processing and quantum metrology.

We have also studied the adiabatic geometric phase in another simple quantum system – a harmonic oscillator, naturally represented in our circuit QED setup as one of the electromagnetic modes of an on-chip coplanar waveguide resonator [3]. Unlike the qubit case, the geometric phase of a harmonic oscillator is a global phase common to all energy eigenstates and, as a result, is not directly observable. Therefore, we make use of a transmon-type qubit dispersively coupled to the resonator mode as a probe. The coupling modifies the oscillator geometric phase depending on the qubit state, which allows us to read out the phase difference in a standard interferometric measurement (Fig. 7.5b).

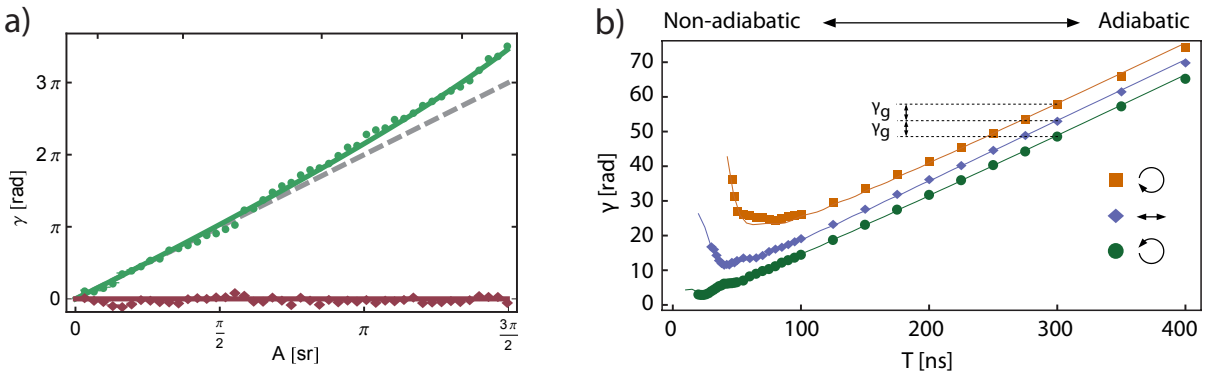


**Figure 7.5:** (a) Experimentally determined geometric phase $\gamma$ of a qubit as a function of the solid angle $A$ enclosed by the effective magnetic field applied to the qubit [2]. Shown is the data where geometric phase was acquired (green dots) as well as the zero phase measured in a control experiment (red diamonds). Theory curves obtained with second-order perturbation theory (solid lines) and the prediction for a two-level system (dashed line) are also plotted. (b) The total measured phase $\gamma$ accumulated by a harmonic oscillator as a function of the total evolution time $T$ [3]. The geometric phase $\gamma_g$ is determined by the difference between the trajectories encircling a positive (green), negative (orange) and zero (blue) area.

We have observed the key features of the geometric phase – its dependence on the shape of the quantum state path only and its insensitivity to the total evolution time. We have also identified non-adiabatic effects which cause undesirable qubit-oscillator entanglement, resulting in qubit dephasing. However, the measured qubit coherence exhibits revivals when the total evolution time is approximately divisible by the period of the non-adiabatic transients. This points towards future implementations of faster, non-adiabatic geometric quantum gates which benefit from the expected noise resilience of geometric phases but do not suffer from decoherence due to non-adiabaticity.

[1] P. J. Leek, J. M. Fink, A. Blais, R. Bianchetti, M. Göppl, J. M. Gambetta, D. I. Schuster, L. Frunzio, R. J. Schoelkopf, and A. Wallraff, Science **318**, 1889 (2007).

[2] S. Berger, M. Pechal, S. Pugnetti, A. A. Abdumalikov Jr., L. Steffen, A. Fedorov, A. Wallraff, and S. Filipp., Phys. Rev. B **85**, 220502(R) (2012).

[3] M. Pechal, S. Berger, A. A. Abdumalikov Jr., J. M. Fink, J. A. Mlynek, L. Steffen, A. Wallraff, and S. Filipp, Phys. Rev. Lett. **108**, 170401 (2012).

## 7.5 Hybrid quantum systems based on semiconductor quantum dots and superconducting microwave resonators

### 7.5.1 Dipole coupling of a double quantum dot to a microwave resonator

T. Frey, P. J. Leek, M. Beck, A. Blais, T. Ihn, K. Ensslin, and A. Wallraff

We have realized a novel device in which a semiconductor double quantum dot is dipole coupled to a GHz-frequency high-quality transmission line resonator as shown in Fig. 7.6. This approach allows us to characterize the properties of the double dot by measuring both its dispersive and dissipative interaction with the resonator [1]. In addition to providing a new readout mechanism, this architecture has the potential to isolate the dots from the environment and to provide long distance coupling between spatially separated dots. These features are expected to improve the potential for realizing a quantum information processor with quantum dots as previously demonstrated for superconducting circuits making use of circuit quantum electrodynamics.

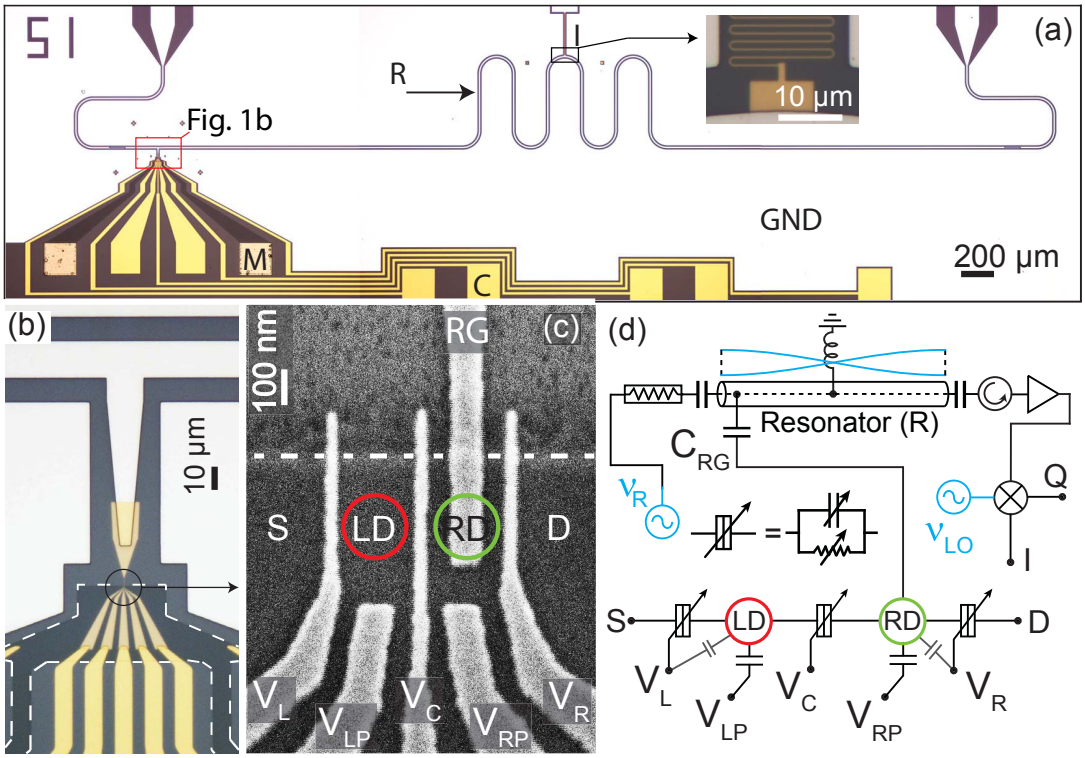


**Figure 7.6:** (a) Optical micrograph of the microwave resonator (R), with integrated double quantum dot, Ohmic contacts (M), top gates (C), ground plane (GND), and on-chip inductor (I). Inset: Magnified view of inductor (I). (b) Enlarged view of the device near the double quantum dot. The mesa edge is highlighted with a dashed line. (c) Scanning electron micrograph of the gate structure defining the double quantum dot (LD, RD). (d) Electric circuit representation of the double quantum dot coupled to the resonator.

[1] T. Frey, P. J. Leek, M. Beck, A. Blais, T. Ihn, K. Ensslin and A. Wallraff, Phys. Rev. Lett **108**, 046807 (2012)

### 7.5.2 Quantum dot admittance probed at microwave frequencies with an on-chip resonator

T. Frey, P. J. Leek, M. Beck, J. Faist, A. Wallraff, K. Ensslin, T. Ihn, and M. Büttiker

We have investigated the microwave frequency dynamic admittance of a quantum dot tunnel coupled to a two-dimensional electron gas. The measurements are made via a high-quality 6.75 GHz on-chip resonator capacitively coupled to the dot. The resonator frequency is found to shift both down and up close to conductance resonances of the dot corresponding to a change in the reactance of the system from capacitive to inductive (see Fig. 7.7). The observations are consistently explained in a scattering matrix model. The character of the reactance depends on the detuning of the dot from conductance resonance and on the magnitude of the tunnel rate to the lead with respect to the resonator frequency [1]. Inductive response is observed on a conductance resonance, when tunnel coupling and temperature are sufficiently small compared to the resonator frequency. Our measurement scheme using the microwave resonator for detecting finite frequency properties of semiconductor nanostructures has promise for future experiments in which the sensitivity of the resonator can be further exploited to, for example, measure the shot noise properties of a tunnel barrier in more detail.

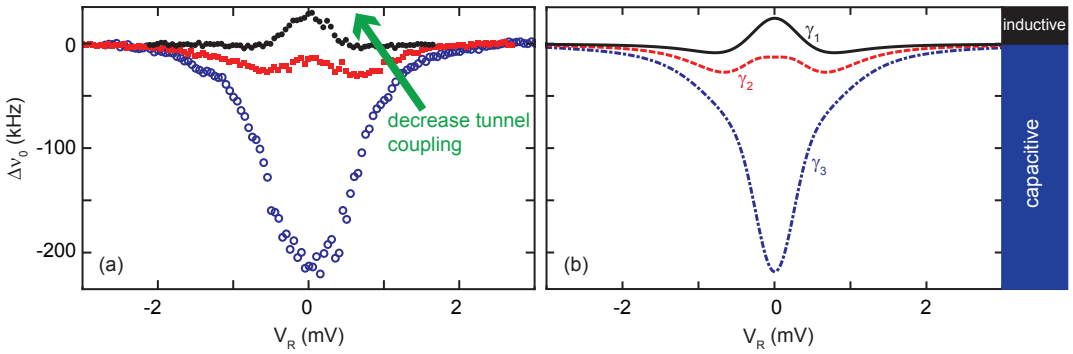


**Figure 7.7:** (a) Measured change of resonator frequency $\Delta\nu_0$ for three different characteristic resonant dot lead coupling strengths $\gamma$. (b) Results of the scattering matrix model calculations using three different tunnel couplings: $\gamma_1/h = 20$ MHz, $\gamma_2/h = 58$ MHz, $\gamma_3/h = 125$ MHz.

[1] T. Frey, P. J. Leek, M. Beck, A. Wallraff, K. Ensslin, T. Ihn and M. Büttiker, Phys. Rev. B **86**, 115303 (2012)

## 7.6 Realization of gigahertz-frequency impedance matching circuits for nano-scale devices

G. Puebla-Hellmann, and A. Wallraff

Microwave circuits based on superconducting transmission lines can also be used to investigate electron transport through nanometer scale electronic devices based on single molecules or carbon nanotubes. By measuring the radio-frequency properties of such a circuit, the properties of the integrated device can be determined with a larger bandwidth and better signal-to-noise compared to DC measurements, allowing, for example, for measurements with microsecond or better time resolution.

We realized so-called stub tuners, which transform a target impedance, typically 12-100 kΩ, to 50 Ω at a resonance frequency in the GHz range [1]. The device consists of two transmission line sections, with the device placed at the end of one section, the other section terminating in an open end, as shown in Fig. 7.8 (a-c). We measure the microwave reflection coefficient, which depends both on the frequency and the resistance of the integrated device, expecting a coefficient of one for low device resistances and away from the resonance frequency and zero on resonance and at the target matched resistance.

To characterize the circuit, a thin gold wire, known as a break-junction was integrated and successively thinned by application of a current, leading to a variable resistance. Reflection spectra of the device at different resistances were taken. A resonance developed as the resistance increased, plotted in Fig. 7.8 (d). The relevant device parameters were extracted from a single spectrum and then used to predict the properties of the device. In particular, Fig. 7.8 (e) shows a comparison of the measured reflection coefficient at resonance as a function of DC resistance (blue points) versus the predicted behavior (dashed line) based on the parameters extracted at 12 kΩ. It is further possible to extract the impedance of the gold wire at GHz frequencies from the spectra using these parameters. A comparison of the measured DC resistance and extracted RF impedance is shown in Fig. 7.8 (f), indicating that the DC resistance agrees well with the RF impedance of a break-junction at 6 GHz.

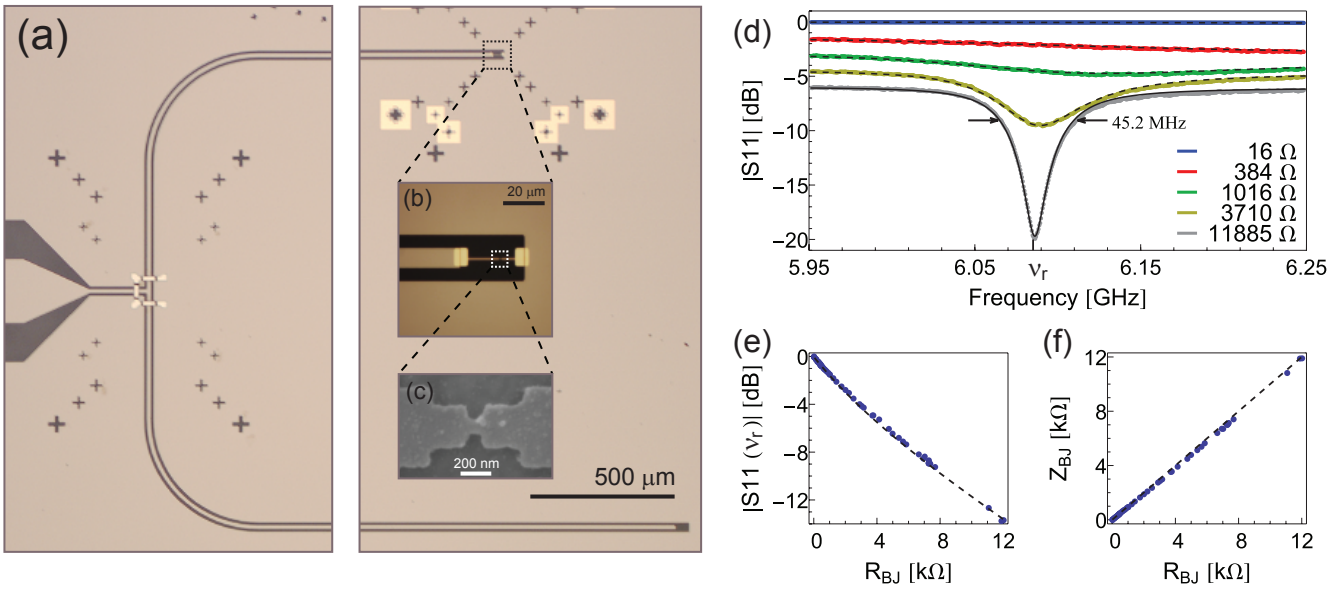


**Figure 7.8:** (a) Optical image of the sample, showing the input port (left hand side) and the two transmission lines. A break-junction is placed at the end of the upper line, an optical zoom is shown in (b) and an SEM image in (c).(d) Reflection spectra of an impedance matching circuit at different resistances of the break-junction. As the junction resistance increases, the resonance becomes more pronounced. (e) The reflection coefficient $\Gamma$ as a function of break junction resistance (blue points), the dashed line is the predicted behavior based on the parameters extracted at 12 k$\Omega$. (f) A comparison between the DC resistance and RF impedance of the break-junction.

[1] G. Puebla-Hellmann, and A. Wallraff. App. Phys. Lett. **101**, 053108 (2012)

## 7.7 Driving Rydberg-Rydberg transitions from a coplanar microwave waveguide

S. D. Hogan, J. A. Agner, F. Merkt, T. Thiele, S. Filipp, and A. Wallraff

A variety of physical systems such as neutral or charged atoms, quantum dots, nuclear spins or superconducting circuits, to name a few, can nowadays be coherently controlled and manipulated in the lab to explore quantum mechanics at the level of single energy quanta. In our experiments we aim to extend the scope of current techniques by combining two seemingly disparate systems – Rydberg atoms and artificial superconducting atoms – into a single hybrid quantum device to explore novel directions towards quantum-enabled applications. In our cryogenic experiments we utilize quasi-one-dimensional chip-based microwave resonators as a photonic interface between Rydberg atoms and superconducting qubits. As a first step towards a hybrid quantum device we have demonstrated Rabi oscillations between Rydberg states of meta-stable helium driven by a microwave waveguide source in a cryogenic setup [1].

We have realized a cryogenic setup in which a pulsed meta-stable helium beam is produced in a supersonic expansion followed by an electric discharge (Figure 7.9(a)). The atoms are excited to their $33p$ Rydberg state by a 313 nm pulsed laser excitation inside the cold chamber which can be operated at temperatures down to 3 Kelvin. Transitions between Rydberg states ($33p \rightarrow 33s$) are induced by microwave photons from a coplanar transmission line fabricated on a printed circuit board. Turning on the microwave field for about 1 $\mu$s when the atomic ensemble passes over the coplanar transmission line leads to a population transfer to the $33s$ state. After interacting with the microwave fields, an electric field pulse ionizes the Rydberg atoms depending on their electronic state and the resulting electrons are detected at a micro-channel plate. In this way, Rabi oscillations with typical oscillation frequencies of 30 ns have been measured (Figure 7.9(b)).

Currently, the coherence time is limited by field inhomogeneities across the dimension of the Rydberg cloud as well as by stray electric fields emanating from the PCB surface. A dephasing time of approx. 250 ns due to the atomic motion in an inhomogeneous fluctuating electric field has been deduced from Monte-Carlo simulations of the

atom trajectories. In future experiments the coplanar transmission line on a copper-plated PCB used in the current experiments will be replaced by a superconducting one fabricated on a single-crystal substrate to reduce the effects of stray electric fields from surface imperfections. Collimation and guiding elements will be realized on chip to gain control over the atom-surface distance and the size of the ensemble.

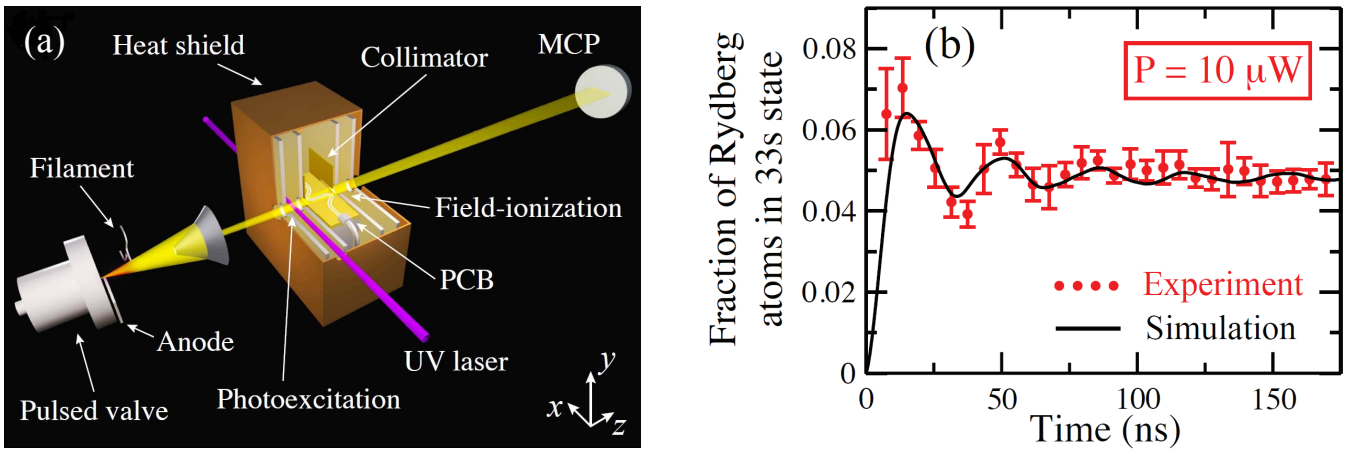


**Figure 7.9:** (a) Diagram of the setup used to generate Rydberg states of helium by a frequency doubled pulsed dye laser. (b) Rabi-oscillations observed in the fraction of Rydberg states transferred from the $33p$ to the $33s$ state at a microwave input power P of 4 W. The Monte-Carlo simulation (solid line) takes the inhomogeneities of the microwave field and the stray field of the surface into account.

[1] S. D. Hogan, J. A. Agner, F. Merkt, T. Thiele, S. Filipp, and A. Wallraff. Phys. Rev. Lett. **108**, 063004 (2012)

# Chapter 8

# Semiconductor Quantum Materials

(http://www.mbe.ethz.ch/)

**Head**
Prof. Dr. W. Wegscheider

**Academic Staff**

| | | |
|---|---|---|
| C. Charpentier | Dr. S. Fält | Dr. T. Feil |
| A. Maier | S. Peters | C. Reichl |
| S. Riedi | Dr. W. Stumpf | Dr. L. Tiemann |
| W. Wüster | | |

**Technical Staff**

| | | |
|---|---|---|
| J. Gmür | S. Heider | M. Sturzenegger |

**Guest Professor**
Prof. Dr. W. Dietsche

**Secretaries**

| | |
|---|---|
| C. Egli | C. Vinzens |

## 8.1 Highest quality two-dimensional electron systems for $\nu$= 5/2 fractional quantum Hall effect physics

C. Reichl, W. Dietsche, W. Wegscheider

The high-mobility molecular beam epitaxy (MBE) system established in Zurich is capable to produce ultrapure two-dimensional electron gases (2DEGs) in the AlGaAs/GaAs material system with electron mobilities exceeding 2E7 $cm^2$/Vs on a regular basis. Even more important, a well developed fractional quantum hall state (FQHS) $\nu$ = 5/2 can be observed on a variety of sample structures. This very fragile electron state is believed to be crucial for the aspired realization of topological quantum computing. Therefore, one research focus lied on a quantitative analysis of the activation energies of the $\nu$ = 5/2 state with respect to growth conditions and structure design. By reducing the potential disorder originating from randomly distributed ionized donors the 5/2 gap energy could be increased from 25 to 138 mK. Substantial improvements in terms of gap energy were also achieved by optimizing growth parameters like substrate temperature profile, which also lead to a reduction of uncharged impurities in the 2DEG channel region. First results have been obtained to link the quality of the $\nu$ = 5/2 state to other, less fragile FQHSs which can be observed at much easier to reach temperatures around 300 mK.

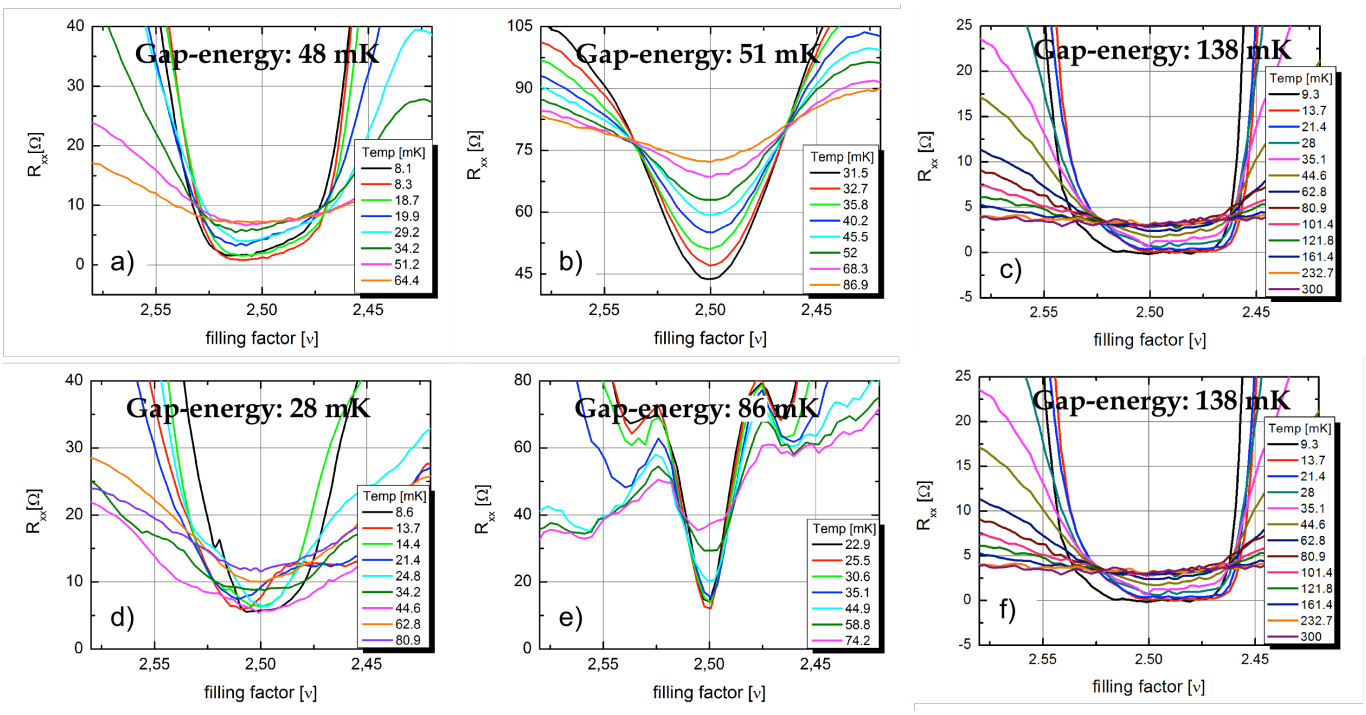


**Figure 8.1:** Temperature-dependent B-field measurements around $\nu$ = 5/2. The structures vary in setback distance 75nm (a), 80nm (b) and 100nm (c); and in the implemented doping scheme: simple $\delta$-doping in AlGaAs (d), $\delta$-doping in AlGaAs with additional secondary quantum wells (e), short-period superlattice (SPSL)-doping (f).

## 8.2 Gate-induced two-dimensional electron systems in undoped GaAs/AlGaAs heterostructures

S. Peters, W. Wegscheider

Hall-bar devices were fabricated on undoped GaAs/AlGaAs heterostructures. By means of a back gate or a top gate, we managed to induce a 2DEG in these undoped structures both from the back and the front side of the wafer. In the

latter case a Ti/Au top gate was evaporated on a polyimide layer functioning as an insulator. In the back-gate case an undoped structure was grown on a n+-substrate acting as a back gate. Thus the distance between the gate and the Ohmics is increased considerably, compared to the top gate overlapping the Ohmics on the surface, and a 2DEG could be induced both at a single interface and inside a quantum well. Figure 1 shows the densities and mobilities obtained at different positive voltages applied to the back gate (a) and to the top gate deposited on a single-interface structure (b). The much higher voltages needed are due to the thickness of the polyimide which is around 1.5 micron.

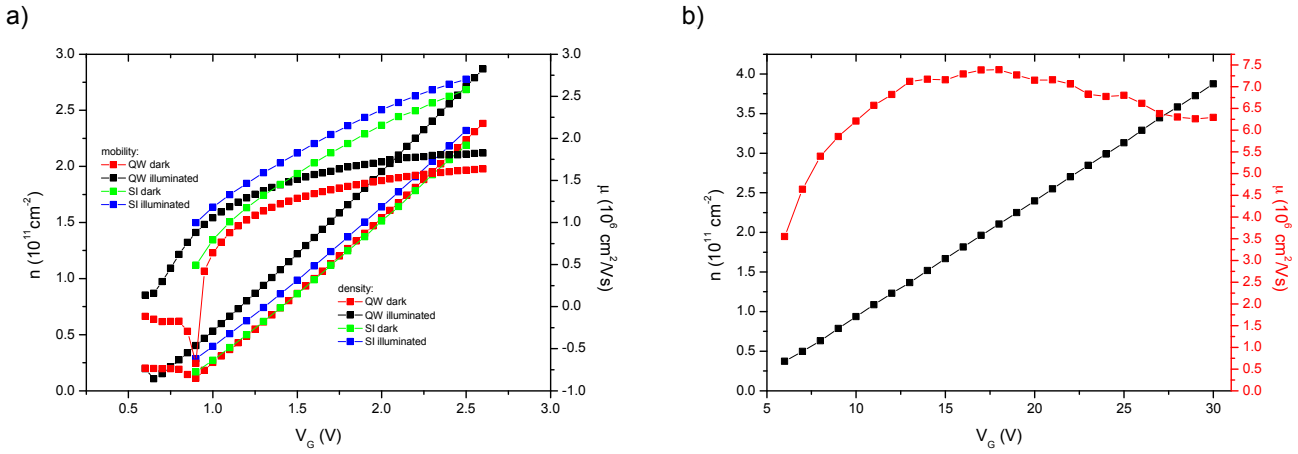


**Figure 8.2:** Gate-voltage dependences of density and mobility obtained in an induced 2DEG - a) back gate b) top gate, measured at 1,5K.

The lower values of mobility in the back-gated structures might be caused by the fact that the wave function is located in the AlGaAs/GaAs interface, which is known from doped inverted structures to show a higher roughness than the GaAs/AlGaAs interface. This issue will be addressed during the growth process and by depositing an additional top gate. This top gate should enable us to move the 2DEG wave function off the critical AlGaAs/GaAs interface. Analogously, an additional back gate should make the mobility of the top-gate induced 2DEG increase.

## 8.3 Raman Spectroscopy in the Quantum Hall Regime

T. Feil, S. Peters, S. Fält, W. Wegscheider

We study the excitations of high-mobility 2DEGs at low temperatures and high magnetic fields. A crucial obstacle for these studies is the light sensitivity of samples with respect to illumination. Under constant illumination samples change their density and screening properties which leads to the destruction of interesting correlated electron states. In order to stabilize samples under illumination, structures were developed that show high mobility and a well developed 5/2 state while having an additional tuning knob to adjust the sample under illumination. This added degree of freedom comes in form of a backgate. This is a conducting layer underneath the two-dimensional electron gas whose potential can be used to change the shape and density of the quantum well. Since the gate lies underneath the quantum well, optical access to the structure is not inhibited. Figure 8.3 shows transport measurements of the longitudinal and Hall resistance where the gate voltage is swept while the magnetic field is held constant. With increasing magnetic field filling factor 5/2 becomes more and more pronounced. With a transparent gate dielectric the back-gate can be used to compensate changes in sample properties that are introduced under illumination.

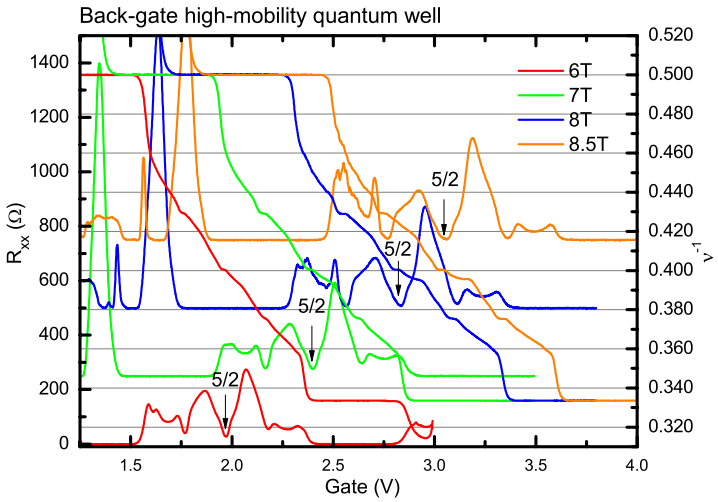


**Figure 8.3:** Gate voltage scans across filling factor 5/2 for different magnetic fields, recorded at a temperature of 20mK.

## 8.4 Quantum Hall effects in Aluminium Gallium Arsenide

L. Tiemann, W. Wegscheider

The ability to epitaxially grow layers of aluminium gallium arsenide ($Al_xGa_{1-x}As$) compounds which possess band gaps that depend on the aluminium content x is the key to study a variety of quantum effects in two-dimensional electron systems. When pure GaAs (i.e., x = 0) is sandwiched between $Al_xGa_{1-x}As$ (with ca. $0.2 < x < 0.4$), electrons accumulate at the center of the Brillouin zone, rendering it a direct semiconductor. For many years these GaAs/AlGaAs heterostructures have been the prevailing system in research focusing on the quantum Hall effect. In contrast, in pure AlAs (i.e., x = 1) quantum wells electrons are confined to either one valley or two degenerate valleys near the X-point at the boundary of the Brillouin zone, rendering it an indirect semiconductor with an anisotropic (ellipsoidal) Fermi surface; akin to silicon. The resulting anisotropic effective electron mass in combination with different valley degeneracies make AlAs an interesting material for mesoscopic physics and collective phenomena. However, research has mainly focused on GaAs systems, which nowadays exhibit top electron mobilities exceeding 3E7 $cm^2$/Vs, while the low temperature electron mobilities in AlAs systems have stagnated below 5E5 $cm^2$/Vs. The first goal in this project is therefore to improve the design and growth parameters in order to increase the scattering times, a prerequisite for the observation of many quantum effects in AlAs.

## 8.5 High mobility two-dimensional hole-gas (2DHG) structures for charge and spin transport measurements

S. Riedi, A. Maier, W. Wegscheider

High quality 2DHG structures are the building blocks for interesting spin and charge transport experiments in hole systems. We have optimized molecular beam epitaxy (MBE) growth of single sided carbon doped quantum well structures and reached low-temperature mobilities exceeding 1E6 $cm^2$/Vs. In magnetotransport measurements pronounced beating patterns are observed in the longitudinal resistance (Figure 8.4a) , indicative of Rashba spin-orbit coupling. Consequently, these samples are suitable candidates for examining both charge and spin transport in 2DHGs.

One exciting application is the cleaved edge overgrowth technique (CEO) for the fabrication of nanowires and perpendicular interfaces. To exploit the full potential of this method, i.e. the creation of atomically flat interfaces, samples

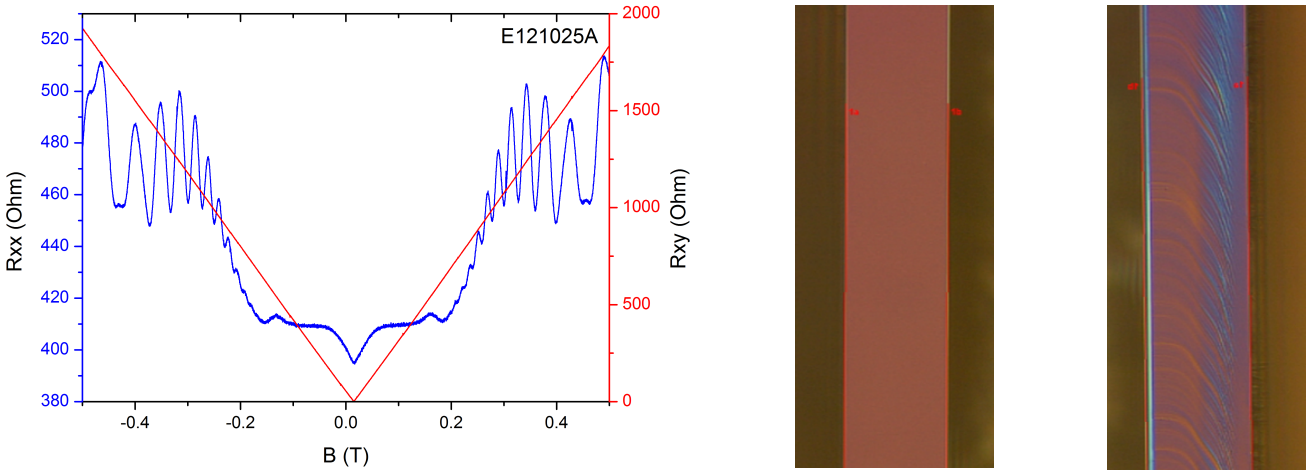


**Figure 8.4:** a) Low-temperature (0.3 K) magnetotransport measurement of a single sided carbon doped quantum well. Note the beating pattern at $\pm$ 0.3 T. b) Microscopy images (Nomarski mode) of a smooth and a rough overgrown cleaved edge of a CEO sample (the sample thickness, i.e. width of the displayed sample region, is approx. 100 micron).

are cleaved inside the MBE at pre-established scratch marks and immediately overgrown. A smooth cleaving is thereby the crucial step and a hallmark for promising samples. Standard characterization of the cleaved edges is done by light microscope imaging whereby unwanted distinct step-like features can be detected quite sensitively (Figure 8.4b). However, scanning electron microscopy studies revealed even smaller features, which could explain problems in the fabrication of working CEO structures. Since this issue has not been addressed previously, further studies are necessary to clarify the relevance of these features.

## 8.6 Optically active quantum dots for quantum information devices

W. Stumpf, M. Locher, S. Fält, W. Wegscheider

The growth of high mobility structures as achieved using our MBE system is not only favorable for application to indium containing heterostructures but also for the combination with them. Indium compound material confined to a small number of dimensions (self-assembled quantum dots [SAQDs], quantum wires, etc.) becomes increasingly sensitive to material impurities, composition, and its enclosing environment, thus allowing for probing and manipulating inherent quantum states. Hence, material purity and quality are crucial points in applications of manipulating, storing, and sensing quantum information. A gate-defined QD in a 2DEG coupled to a SAQD in close proximity may help to gain insight to mutual interactions and may allow for creating an opto-electronic device to control photon polarization in the future. Thus far, transport experiments demonstrated the ability to sense electronic properties of single SAQDs. SAQD growth however, not necessarily yields the desired needs in emission wavelength, exciton linewidth, QD density and other parameters. In order to cope with the challenge to adjust SAQD properties to different experimental requirements, we started building an experimental setup that can achieve high sensitivity simultaneously with high spatial and optical resolution. The setup already enables basic characterization of test samples, here blue-shifted SAQDs, exemplarily shown in Figure 8.5.

For SAQD devices that store the electron spin in the SAQD rather than a gate-defined QD, the material properties of the SAQD becomes more interesting than that of a hypothetical 2DEG. SAQD structures have recently been grown in our lab under conditions optimized for the formation of InAs QDs rather than high mobility. These devices show optical properties that are indicative of high SAQD quality and are necessary for quantum information experiments, such as spin-pumping that can be used for qubit initialization.

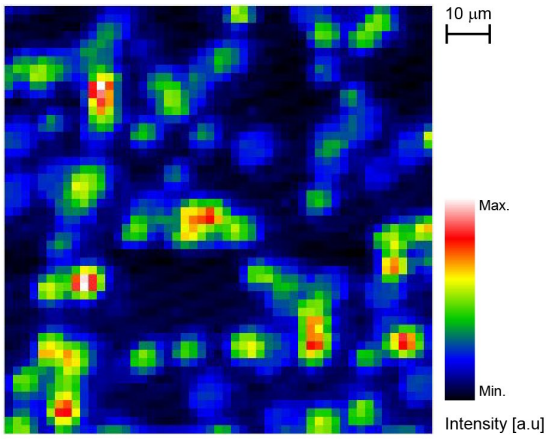


**Figure 8.5:** 2D plot of the integrated photoluminescence intensity around 950 nm of InAs QDs measured at 4.2 K.

## 8.7 Excitons and Trions in Gated High Mobility 2DEGs

W. Wüster, S. Smolka, F. Haupt, S. Fält, C. Reichl, A. Imamoglu, W. Wegscheider

We investigate excitonic and trionic transitions in gated 2DEG quantum well structures at mK temperatures in a confocal microscope setup with a diffraction limited spot size and magnetic fields up to 7 Tesla. Optical absorption spectroscopy allows probing the many body nature of the states of the electron gas in presence of a photo-excited hole. Tuning the electron density via a top gate enables us to reach the limits of the empty quantum well as well as the regime of a 2DEG. With these knobs we study many body phenomena as the Fermi edge singularity at zero magnetic fields or the spin polarization of quantum Hall states at finite magnetic field.

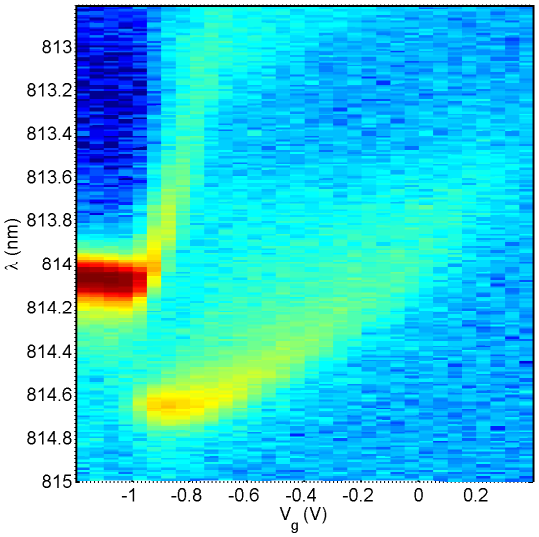


**Figure 8.6:** At zero magnetic field the absorption spectrum as function of gate voltage shows characteristics of excitonic two-particle and trionic three-particle bound states of the photo-excited hole with one and two electrons respectively. The additional binding energy of the trion is reflected in the discrete jump at about -1 volts. At high electron densities the trion is energetically favorable and the exciton vanishes. The blueshift of the transitions is most probably due to an interplay of band-gap renormalization and the screening capability of the 2DEG electrons. Line shapes get asymmetric which is commonly attributed to the Fermi edge singularity.

## 8.8 High-mobility Sb-based III/V-semiconductor heterostructures

C. Charpentier, W. Wegscheider

Sb-based III/V semiconductor heterostructures offer a wide range of interesting physical properties as the very high barriers (1.35 eV) and low effective electron mass ($0.023m_e$) in InAs/AlSb quantum wells, the broken gap band alignment in InAs/GaSb/AlSb composite quantum wells and the extremely low electron mass ($0.014m_e$) and very high g-factor (g*=-51) in InSb/AlInSb quantum wells. In the past year, our group was successful in the MBE growth of high-quality InAs/GaSb/AlSb composite quantum wells that show signs of electron-hole hybridization and, thus, being promising candidates for showing the topologically insulating phase responsible for the quantum spin Hall effect, as predicted by Liu et al. (Phys. Rev. Lett. 100, 236601 (2008)). This project is in collaboration with the group of Prof. Ensslin where the samples are processed and structured. To improve our understanding of the basic growth mechanisms and to optimize the electronic properties and surface roughnesses of the 6.1 Å lattice constant materials (AlSb/GaSb/InAs) on GaAs substrates, we investigated InAs/AlSb quantum wells with different growth procedures by magnetotransport experiments, atomic force microscopy and fourier transform infrared spectroscopy. In addition, we started the fabrication of InSb/AlInSb quantum wells. The very large lattice mismatch of InSb with respect to GaAs substrates ($\sim 15\%$) makes the growth of these structures difficult. Further effort has to be put into the optimization of growth processes and doping schemes. These quantum wells, in addition to their unique material properties as mentioned above, are very interesting candidates for the creation of Majorana fermions in combination with nanolithography a proximity superconductivity.

# Chapter 9

# Neutron scattering and magnetism

**Head**
Prof. Dr. A. Zheludev

**Academic Staff**

| | | |
|---|---|---|
| S. Gvasaliya | D. Hüvonen | W. Lorenz |
| E. Wulf | G. Simutis | M. Haelg |
| M. Thede | D. Schmidiger | S. Chillal |

**Masters Students**

| | |
|---|---|
| D. Koulialias | FS2013 |

**Administrative Staff**
B. Abt

**Academic Guests**
K. Povarov (P.L. Kapitza Institute, Moscow, Russia) 01.10.12 – 30.11.12
S. Lushnikov (Ioffe Institue, St. Petersburg, Russia) 03.05.12 – 15.06.12
E. Popova (St. Petersburg State University, Russia) 01.07.12 – 31.08.12

## 9.1 Complete spectrum of a spin-ladder in the field-induced Luttinger-Liquid phase

D. Schmidiger

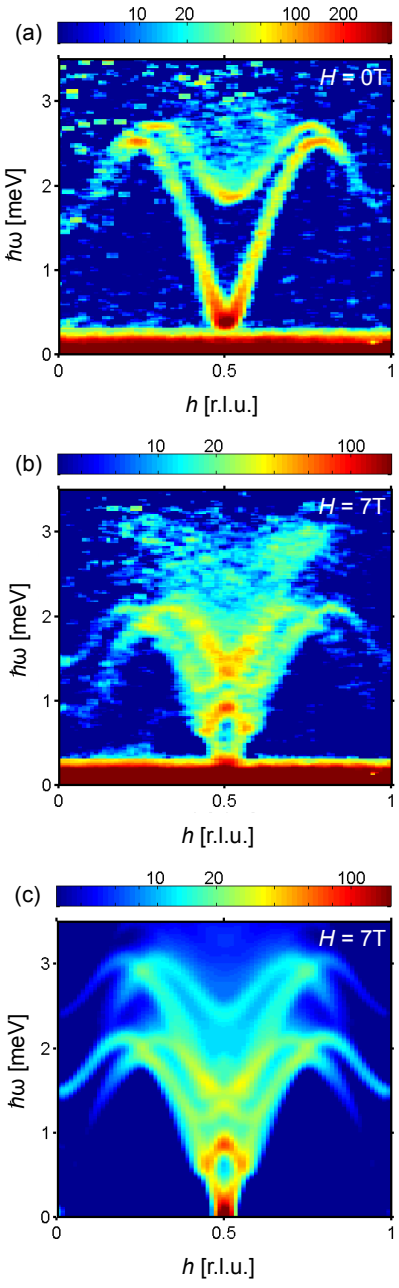


**Figure 9.1:** Time-of-flight data measured $(a)$ at $H = 0$ T in the spin liquid regime and $(b)$ at $H = 7$ T in the Luttinger liquid regime. $(c)$ Numerical DMRG calculation fully reproducing the measured spectrum.

The quantum $S = 1/2$ antiferromagnetic spin ladder belongs to the most important models in quantum magnetism. However, it was the discovery of *organometallic* materials that opened the door to completely new physics: These systems are not only clean realization of one-dimensional toy Hamiltonians, but feature *intrinsically* low energy scales such that e.g. magnetic field strenghts available in laboratories may have tremendous effects.

In the last few years, we have studied the organometallic Heisenberg spin-ladder material $(C_7H_{10}N)_2CuBr_4$ (DIMPY) [1,2]. In zero field, the system remains in a spin-liquid ground state while its spectrum consists of a gapped dispersive magnon excitation below a two-magnon bound state and a weaker two-magnon continuum (fig. 9.1a).

Detailed inelastic neutron scattering studies in combination with numerical DMRG calculations revealed that this material is fully described by a spin-ladder Hamiltonian with exchange constants $J_{\mathrm{leg}} = 1.42$ meV and $J_{\mathrm{rung}} = 0.82$ meV, leading to a gap of $\Delta = 0.33$ meV [2]. By applying a magnetic field larger than $H_{\mathrm{c1}} \simeq 2.7$ T, the system is driven through a quantum phase transition to an algebraic Luttinger liquid state with a spectrum dominated by intercalated two-spinon continua.

Being interested in the field-dependence of the momentum- and energy- resolved spectrum, we performed inelastic neutron scattering experiments with the neutron time-of-flight technique at the LET instrument (ISIS, UK). In zero field, we observe the magnon, two-magnon bound state as well as continuum contributions (fig. 9.1a), in agreement with previous experiments. However, by applying a magnetic field larger than $H_{\mathrm{c1}}$, the spectrum dramatically changes (fig. 9.1b). The initially sharp modes decompose into various intercalated and structured continous contributions while the low-energy spectrum becomes linear and gapless. Although the latter is analytically described by the universal Luttinger liquid theory [3], most of the spectrum is non-universal and depends on the details of the Hamilton operator. Due to recent progres in numerical methods, it can be calculated with high precission nowadays. In figure 9.1c we present DMRG calculations from the group of Prof. Giamarchi and Prof. Kollath (University of Geneva) which prove excellent agreement between theory and experiment.

In conclusion, we claim to fully understand now the complete spectrum of a spin-ladder (in its simplest form), both in the zero-field spin liquid and the field-induced Luttinger-liquid phase. In the future, we are focussing on the effects of other external parameters such as finite temperature, applied pressure as well as the rich field of magnetic and non-magnetic impurities.

[1] D. Schmidiger et al., Phys. Rev. B **84**, 144421 (2011)
[2] D. Schmidiger et al., Phys. Rev. Lett. **108**, 167201 (2012)

[3] T. Giamarchi, Quantum Physics in one Dimension, Clarendon Press (2003)

## 9.2 Spin dynamics in an exchange disordered spin liquid.

D. Hüvonen

Disordered quantum magnets are expected to exhibit qualitatively different behaviour from pure systems. Our recent efforts have been focused on determining the effect of random bond strengths on the spin excitation spectrum in the prototypical spin liquid PHCC [1].

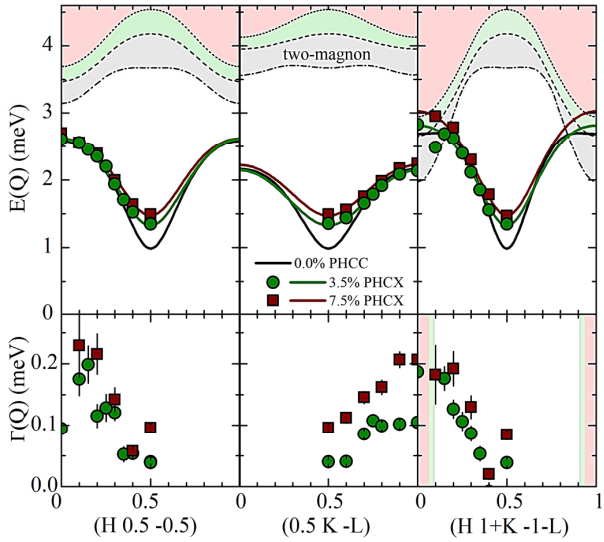


**Figure 9.2:** Magnon frequencies and intrinsic linewidths (symbols) for bond disordered PHCC. Solid lines show the model fit and shaded areas the calculated two-magnon continua for the respective model.

In PHCC the s = 1/2 $Cu^{2+}$ ions are connected through a complex semi-frustrated network of exchange interactions by Cu-Cl-Cl-Cu bonds in the crystallographic (ac)-planes. We introduce disorder by substituting a fraction of the nonmagnetic exchange interaction-mediating Cl ions for the larger ionic radii Br in our wet chemistry lab at ETH. Such a substitution affects the involved bond angles and lengths and therefore locally modulates the strength of superexchange interactions. For neutron scattering studies we have grown fully deuterated samples with 3.5% and 7.5% Br [2]. Measurements were performed with triple axis spectrometer TASP at PSI and on time-of-flight instrument CNCS at Oak Ridge National Laboratory. As extension to our work from previous year [3] we have studied magnon excitation energy and linewidth throughout the Brillouin zone. The measured intrinsic magnon linewidth and the resonance energies are plotted as symbols in Fig. 9.2. The observed magnon spectrum can be described with the same spin wave model as that of the unperturbed material with slightly renormalized parameters to account for increase of spin gap (from 1 to 1.4 and 1.5meV for pure, 3.5 and 7.5% Br samples respectively) and reduction of bandwidth by ≈ 0.2meV (solid lines in Fig.9.2).

Most notable effect of bond disorder is on the lifetime of magnons. At the bottom of the dispersion the resolution limited magnons resonances of the pure material get considerably broadened. Additional increase of damping rate by up to a factor of 3 occurs roughly linearly with wavevector when moving to Brillouin zone boundaries in all measured directions [4]. In comparison to disorder-free PHCC, where magnons dampen due to decay into two magnons, the reduced bandwidth excludes the possibility in the presence of disorder. Although the magnon kinematics are not fully understood such wavevector dependence is likely due to magnon collisions with the impurities of hopping potential induced by bond disorder. This explanation is further supported by observation that the damping rate correlates with single magnon density of states, see Fig. 9.3.

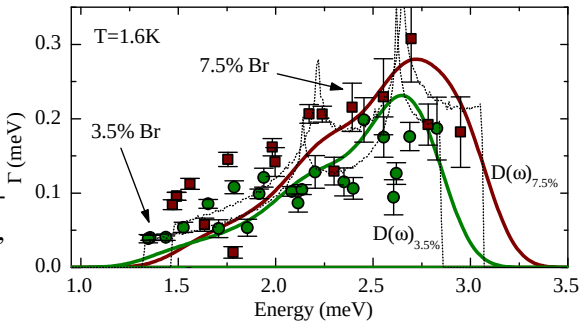


**Figure 9.3:** Measured magnon linewidths and corresponding single magnon density of states functions with (thick lines) and without (thin lines) experimental resolution convolution.

[1] A. Daoud, et al. Phys. Rev. B 33, 6253 (1986).
[2] T. Yankova et al. Philosophical Magazine 92, 2629 (2012).

[3] D. Hüvonen et al. Phys. Rev. B 85, 100410(R) (2012).
[4] D. Hüvonen et al. Phys. Rev. B 86, 214408 (2012).

## 9.3 Pressure induced quantum phase transition in an organic spin liquid

M. Thede, M. Mansson, D. Hüvonen

Field-induced quantum phase transitions in spin liquids have attracted much attention and were studied in great detail in a number of materials. Such transitions are equivalent to BEC in that they break $SO(2)$ symmetry and have a $z = 2$ dynamical critical exponent at the critical point. Much less is known about quantum phase transitions induced in such systems by external pressure. They correspond to a different universality class, breaking $SO(3)$ symmetry. A gapless linear spectrum at the critical point implies a dynamical critical exponent $z = 1$ [1]. The main challenges are experimental: detecting weak magnetic order at very low temperatures inside a hefty pressure cell.

Piperazinium hexachlorodicuprate (PHCC) is a prototypical metallo-organic $S = 1/2$ Heisenberg magnet with a spin liquid ground state. Previous high-pressure inelastic neutron experiments on PHCC by other groups [2] demonstrated that applied hydrostatic pressure has a profound effect on the magnon excitations. Encouragingly, the spin gap appears to soften with increasing pressure. To detect a possible pressure induced ordering transition we performed a series of $\mu$SR experiments at Paul Scherrer Institut. We have studied powder samples at ambient- and four different applied pressure values. At each pressure, we performed zero field and weak transversal field measurements to map out the $P - T$ phase diagram. In the zero field, $\mu$SR time spectra show clear oscillations at 0.3 K, and at pressures exceeding 10.2 kbar. Such features indicate the presence of long-range magnetic order (Fig. 9.4 a). For each pressure, the measured temperature dependence of the internal field at the muon site, which is proportional to the order parameter, is shown in Fig. 9.4 b. The big surprise is that the critical pressure projected of spin gap softening is twice as high as that of magnetic ordering. One possible explanation is that the wave vector of gap softening does not correspond to the dispersion minimum at ambient pressure.

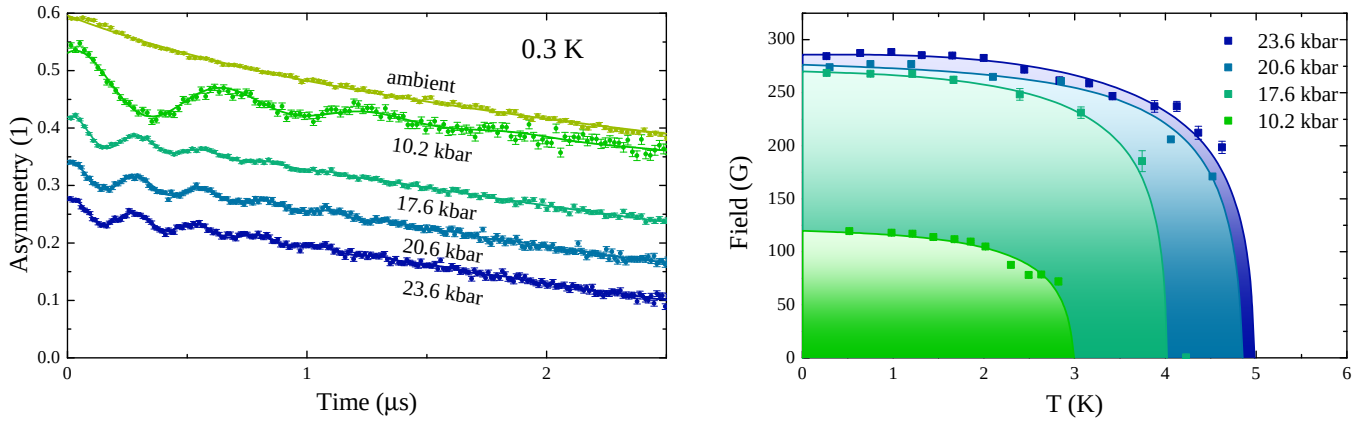


**Figure 9.4:** left: (a) $\mu$SR time spectra measured in PHCC for five different pressures at T = 300 mK. (b) Temperature dependence of the magnetic order parameter for four different pressures.

[1] S. Sachdev, *Quantum Phase Transitions* (Cambridge, 1999)
[2] T. Hong *et al.*, Phys. Rev. B 82, 184424 (2010).

## 9.4 Defect-induced spin pseudogap in $SrCuO_2$

G. Simutis

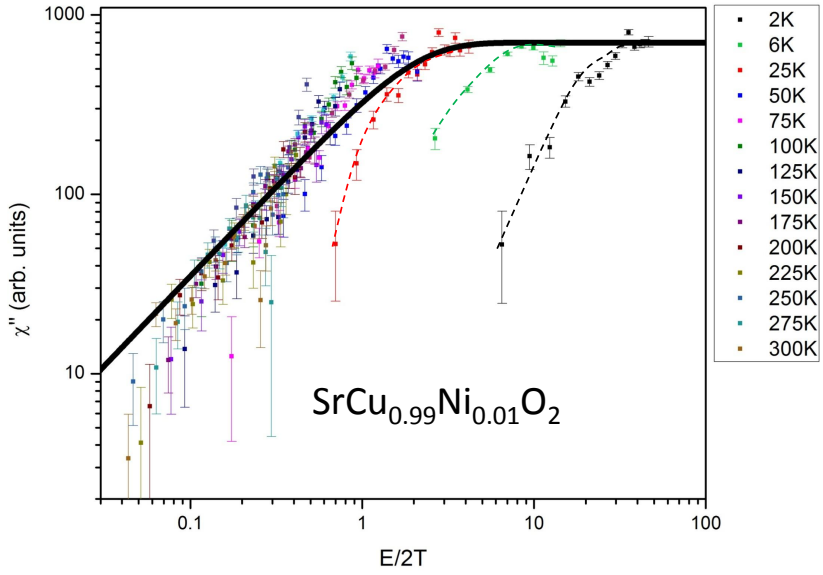


**Figure 9.5:** The imaginary part of the generalized susceptibility in $SrCu_{0.99}Ni_{0.01}O_2$ obtained by inelastic neutron scattering (symbols). The solid line is the expected scaling function of a disorder-free Tomonaga-Luttinger spin liquid. Dashed lines are guides for the eye.

Disorder and defects are always relevant in one dimensional systems. A growing recent research effort has focused on their effect on dynamical and transport properties in one-dimensional quantum magnets. Of particular interest are defects in two of the best known Heisenberg spin chain systems, namely $SrCuO_2$ and $Sr_2CuO_3$. In the parent compounds, $S = 1/2$ antiferromagnetic chains are formed by copper-oxygen plaquetes. The in-chain interactions are rather strong and antiferromagnetic, $\sim 226$ meV and $J \sim 190$ meV, respectively. The gapless spin excitation spectrum, and the huge spin wave velocity ensure that spinons play a significant role in thermal transport along the chain axis. Recent NMR and heat-transport studies have suggested that introduction of disorder in the form of Ca- or Ni-doping may lead to an opening of a spin gap [1]. Neither the details, nor the mechanism of this effect were fully understood, although a possible spin Peierls state was suggested.

To unravel this mystery, we performed inelastic neutron scattering experiments on one doped material, $SrCu_{0.99}Ni_{0.01}O_2$, with the aim to compare it to the previously studied excitations in the defect-free compound [2]. Our main result is that at low tempeteratures the Ni-doped system develops a *pseudogap* in the excitation spectrum. The pseudogap spans about to 10 meV energy transfer and seems to set in at low temperatures, below about 75 K. This is illustrated in Fig. 9.5, which shows the measured imaginary part of the $q$-integrated susceptibility of $SrCu_{0.99}Ni_{0.01}O_2$ plotted as a function of energy transfer, scaled by temperature. For a disorder-free spin chain we would expect a complete data collapse to the universal scaling function for a Tomonaga-Luttinger spin liquid (heavy solid line). Experimentally, the data collapse seems to work rather well for $T > 75$ K, but completely breaks down at low temperatures. In that regime, the spectral weight at low energies is suppressed, as the pseudogap emerges.

[1] F. Hammerath, *et al.*, Phys. Rev. Lett. **107**, 017203 (2011).
[2] I. Zaliznyak, *et al.*, Phys. Rev. Lett. **93**, 087202 (2004)

## 9.5 Cu(quinoxaline)($Cl_{1-x}Br_x$)$_2$ - a tuneable spin-ladder compound

W. EA. Lorenz, K. Yu. Povarov

In our quest to understanding the role of bond strength disorder on the properties and phase behavior of quantum spin liquids, we focused on the strong-rung spin-ladder compound Cu(quinoxaline)($Cl_{1-x}Br_x$)$_2$, CQX for short. Thermodynamic measurements were performed over the full range $x = 0 \ldots 1$. A sketch of the ladder is shown in fig. 9.2. Most direct insight into these compounds is obtained from measurements of the static susceptibility $\chi(T)$ and the magnetization $M(H)$. In the examined temperature range, $T \geq 2$ K we find, that our data are well described within spin-ladder models, with a modest shift of the exchange constants as a function of $x$. Our results support similar ones obtained in a recent, less detailed study [1]. Our data were taken on carefully field oriented powders of CQX in a commercial Quantum Design VSM. The susceptibility data $\chi(T)$ are fitted coherently with the $M(H)$ data. For $\chi(T)$ the high temperature ($T \geq 40$ K) part of the data sets is fitted using the high temperature expansion presented by Bühler *et al.* [2] while data at low temperature are modeled within Quantum Monte-Carlo simulations using the ALPS package. From the obtained exchange constants the gap between singlet and triplet state is calculated according to Johnston *et al.* [3], from which the dispersion of the triplet band and accordingly the magnetization $M(H)$ at finite temperature are calculated [3,4]. All our magnetization data are well described by this model with further inclusion of a term describing paramagnetic impurities. Representative data and fits are displayed in fig. 9.6.

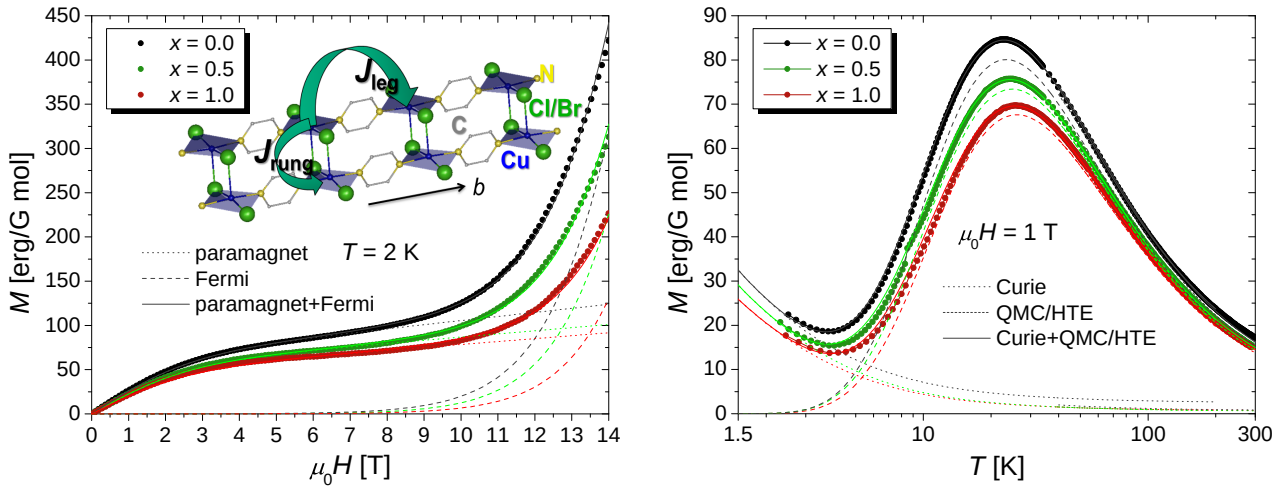


**Figure 9.6:** (left) Magnetization data $M(H)$ with respective fits (see text) display a weak shift of the gap with varying Cl/Br concentration. In the inset, a sketch of the structure of the spin-ladder is illustrated. (right) Magnetization data $M(T)$ for the same samples are fitted coherently with the $M(H)$ data shown left.

Our obtained exchange parameters contrast those obtained in [1], but are in good agreement with an inelastic neutron scattering study for $x = 1$ [5]. In summary, our data do not show any clear features that are to be related to disorder upon varying $x$, but are well explained by a continuous change of exchange constants. Further measurements, including specific heat and AC-susceptibility already indicate however, that contributions presently described as paramagnetic impurities are in fact more complex. Clear measure of disorder is expected from upcoming detailed experiments of specific heat in the quantum critical regime.

[1] B.C. Keith *et al.*, Polyhedron **30**, 3006 (2012).
[2] B. Bauer et al., J. Stat. Mech. P05001 (2011).
[3] D.C. Johnston et al. cond-mat/0001147 (2000).
[4] M. Reigrotzki et al., J. Phys. Condens. Matter 6, 9235 (1994).
[5] T. Hong *et al.*, Phys. Rev. B **74**, 094434 (2006).

## 9.6 Bond disorder in the $S = 1/2$ chain compound $K_2CuSO_4(Cl_{1-x}Br_x)_2$

M. Hälg and W. Lorenz

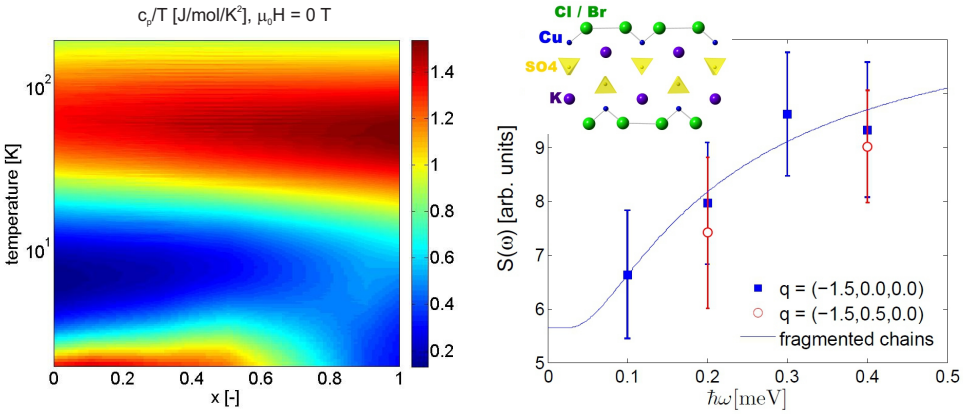


**Figure 9.7:** Left: Specific heat $c_p/T$ with respect to temperature $T$ and Br-concentration $x$. The phononic part at high temperatures gets a magnetic tail near 10 K. Right: The dynamic structure factor $S(\omega)$ shows a pseudogap for $x = 0.9$ (preliminary data). Inset: Exchange path between the Cu-ions of $K_2CuSO_4(Cl_{1-x}Br_x)_2$ via Cl- and Br-ions.

The copper salt $K_2CuSO_4Cl_2$ ($x = 0$) is a Heisenberg antiferromagnetic $S = 1/2$ chain compound. It consists of sheets of Cu-ions which are separated by sulfate groups [1]. Neutron experiments showed that the spins of the Cu-ions only interact along one direction where the exchange path runs via two Cl-ions (see inset in fig. 9.7). Furthermore, no ordering due to inter-chain coupling could be observed in specific heat data down to 90 mK. Its weak nearest neighbor coupling constant ($J_{x=0} = 0.25$ meV) makes it an ideal candidate for studying quantum phase transitions since it can be easily magnetized by experimentally accessible magnetic fields ($\mu_0 H_{sat} = 5$ T).

Exchanging chlorine by bromine in $K_2CuSO_4(Cl_{1-x}Br_x)_2$ tremendously affects the nearest neighbor coupling constant between two spins ($J_{x=1} = 1.8$ meV $\approx 7J_{x=0}$) and thus, even small Br-concentrations have a huge effect on properties of the compound like magnetization or specific heat (see fig. 9.7, left). The fact that the exchange path runs via two Cl-/Br-ions makes the system even more interesting since it enables a third kind of coupling constant $J_{\mathrm{Br-Cl}}$ in addition to $J_{\mathrm{Cl-Cl}} = J_{x=0}$ and $J_{\mathrm{Br-Br}} = J_{x=1}$, where the exchange path runs via one Cl- and one Br-ion. The interplay of the three different coupling constants and their impact on the spin chain properties still need to be studied.

Furthermore, one can discern two regimes depending on the predominant coupling constant: On the Cl-side ($0 < x << 0.5$), few stronger bonds are inserted into a chain with weak coupling. A ground state known as the random singlet phase [2, 3] is expected to emerge in this regime and characteristically affects the behavior of quantities like susceptibility or the dynamic structure factor. In contrast, on the Br-side ($0.5 << x < 1$) the chain is broken due to the very weak coupling via the introduced Cl-ions. Instead of one single spin chain one has to deal with several fragmented chains of different lengths for each of which an energy gap depending on the chain length is expected [4]. Indeed, preliminary neutron data shows a pseudogap in the $q$-integrated dynamic structure factor which is in agreement with this simplistic picture (see fig. 9.7, right). Further inelastic neutron experiments will provide more accurate insight into the behavior of fragmented chains. Moreover, a systematic study of the effect of static disorder on the bulk properties will follow.

[1] C. Giacovazzo *et al.*, Zeitschrift für Kristallographie **144**, 226-237 (1976).
[2] C. Dasgupta and S.-K. Ma, Phys. Rev. B **22**, 1305 (1980).
[3] D. S. Fisher, Phys. Rev. B **50**, 3799 (1994).
[4] S. Eggert and I. Affleck, Phys. Rev. B **46**, 10866 (1992).

## 9.7 Order parameter quantum critical exponents in disordered quantum magnets

E. Wulf

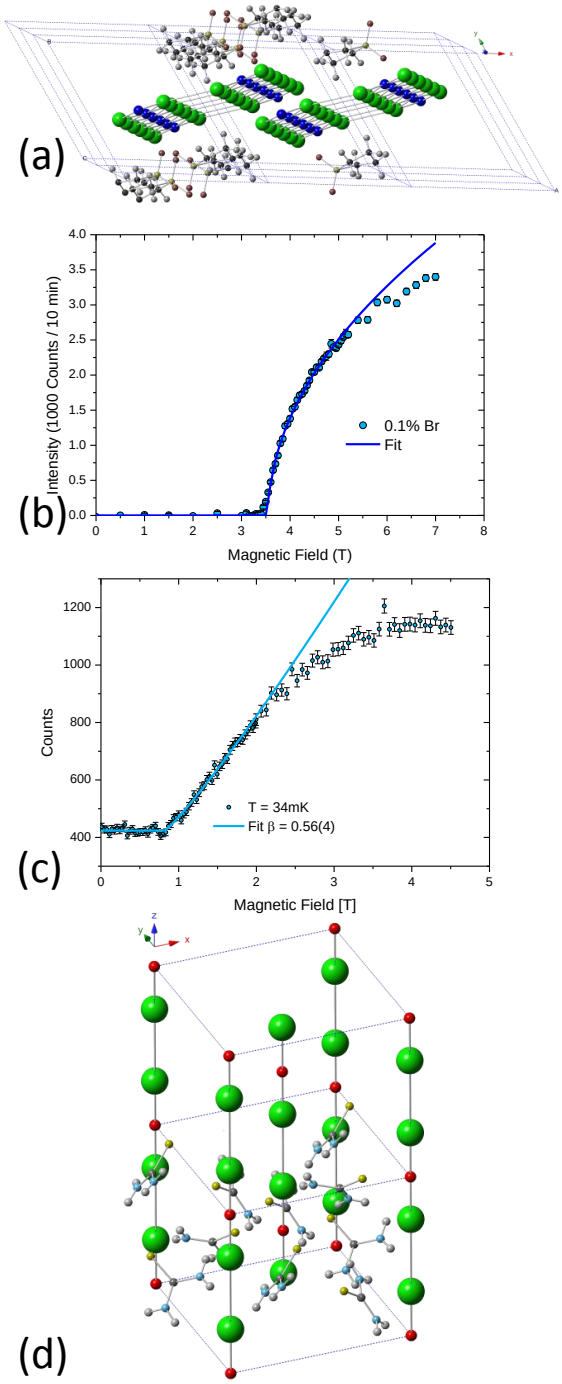


**Figure 9.8:** Crystallographic structure of Sul-$Cu_2(Cl_{1-x}Br_x)_4$ (a) and $Ni(Cl_{1-x}Br_x)_2{\cdot}4SC(NH_2)_2$ (d). Measured temperature dependencies of the magnetic Bragg pek intensities in Sul-$Cu_2(Cl_{1-x}Br_x)_4$ (b) and $Ni(Cl_{1-x}Br_x)_2{\cdot}4SC(NH_2)_2$ (c) (symbols). Lines are power law fits.

Randomness in gapped quantum spin liquids is expected to qualitatively alter the field-induced ordering transition in theses systems. Of a particular interest is the so-called Bose Glass (BG) to magnon Bose-Einstein Condensate (BEC) transition [1]. Recently, its critical exponents became a subject of a heated debate among theorists. On the experimental side, the order parameter critical index $\beta$ can only be probed with magnetic neutron diffraction. We have started a series of such experiments to study the transition in two rater different chemically disordered quantum spin liquids.

One of these materials is the highly frustrated spin ladder system Sul-$Cu_2(Cl_{1-x}Br_x)_4$ (Fig. 9.8a), where disorder is introduced by a chemical substitution on the halogen site. Due to frustration, beyond a field-induced quantum phase transition at $H_c \sim 3.75$ T, at low temperatures the parent material shows incommensurate long range order [2]. Our previous thermodynamic studies revealed that substitution ratios as low as $x = 1\%$ seem to entirely suppress this transition [3]. As a first step in the task of following the fate of the ordered phase, we performed neutron diffraction measurements on samples with very low impurity concentration. For $x = 0.1\%$, for instance, the measured field dependence of the magnetic Bragg intensity (Fig. 9.8b) is very similar to that in the parent material [2]. However, the much higher data quality allows us to discern a possible crossover to a different scaling regime in the field range $\delta H < 0.5$ T. Further measurements, in samples with a progressively increasing Br content, are in progress.

Our second target compound is a three dimensional system with convenient tetragonal symmetry: $Ni(Cl_{1-x}Br_x)_2{\cdot}\,4SC(NH_2)_2$ (see Fig. 9.8d). The ground state is a spin liquid due to a strong easy-plane anisotropy for the $S = 1$ $Ni^{2+}$ ions. The parent compound is believed to be *the* prototypical material where an externl magnetic field induces a BEC of magnons. The disordered system was investigated in experiment [4] and numrical methods [4,5], bringing strong support to a Bose Glass interpretation of it low-field ground state. The order parameter critical exponent was numerically estimated as $\beta = 0.95(10)$ [4,5]. Our first measurements on the $x = 13\%$ material are shown in Fig. 9.8c and cast doubt on this prediction. They suggest $\beta = 0.5$, while $\beta$ close to unity may be entirely excluded.

[1] M. P. A. Fisher *et al.*, Phys. Rev. B **40**, 546 (1989).
[2] V. Garlea *et al.*, Phys. Rev. B **79**, 60404 (2009).
[3] E. Wulf *et al.*, Phys. Rev. B **84**, 174414 (2011).
[4] R. Yu *et al.*, Nature **489**, 379 (2012).
[5] R. Yu *et al.*, Phys. Rev. B **86**, 134421 (2012).

## 9.8 Microscopically coexisting antiferromagnetic and spin glass states

S. Chillal, M. Thede

Coexistence of a long-range magnetic order with spinglass (SG) has long been a matter of controversies. Theory [2] and numerical studies [3] affirmatively suggest a SG freezing of spin components transverse to the long range order parameter [2] in both ferromagnetic (FM) and antiferromagnetic (AF) models. However, experimental evidences for this coexistence in Heisenberg system is absent.

PFN is a perovskite with $Fe^{3+}$ and $Nb^{5+}$ ions randomly occupying B-sites (fig. 9.9 (a)). Apart from showing a long range antiferromagnetic order below $T_N \sim 150$ K, a SG state is observed below $T_{SG} \sim 12$ K. A combined study of neutron scattering and Muon spectroscopy reveals that the long-range order persists even in the SG phase [4]. Report by Kleemann *et al.* [5] suggests that it is due to the clustering of magnetic $Fe^{3+}$ in the non-magnetic $Nb^{5+}$ neighborhood. In order to understand the magnetic ground state of PFN, we performed combined neutron scattering and Mössbauer spectroscopy studies.

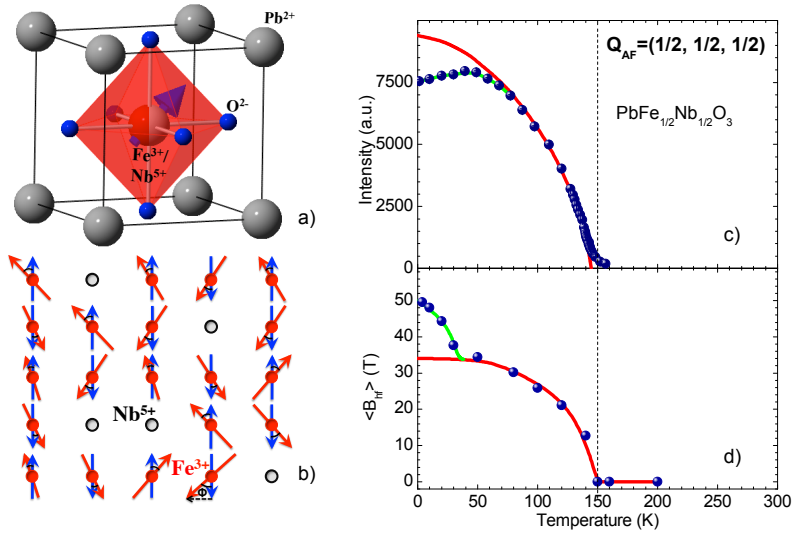


**Figure 9.9:** (a) Chemical structure of $PbFe_{1/2}Nb_{1/2}O_3$ (b) Arrangement of the magnetic moments in the ground state of $PbFe_{1/2}Nb_{1/2}O_3$ (c) The intensity of the antiferromagnetic Bragg peak taken at the wavevector (1/2,1/2,1/2) (d) Average hyperfine field at $Fe^{3+}$ ions probed by Mössbauer spectroscopy. The red and green lines are guide to the eye.

In paramagnetic state, Mössbauer spectra shows an isomer shift corresponding to $Fe^{3+}$ with a non-zero quadrupole splitting. In AF phase, a sextet appears due to the magnetic order in the sample while quadrupole splitting becomes zero. The observed sextet indicates two contributions to the hyperfine field at $Fe^{3+}$ whose mean is shown in Fig. 9.9(d). Two important features of this figure are: 1) The rapid increase in $<B_{hf}>$ below $\sim$ 50 K (Fig. 9.9(d)) which matches with that of reduced AF Bragg peak intensity at the same temperature (Fig. 9.9(c)). 2) $<B_{hf}>$ reaches full moment, as in other $Fe^{3+}$ containing materials, at the base temperature. It is known that the neutron scattering probes staggered magnetization of the long-range AF order. Therefore, reduced Bragg peak intensity (below $\sim$ 50 K ) suggests canting of the AF spins. In contrast, Mössbauer spectroscopy is a local-probe resonant method having excellent sensitivity to local environments. The increasing hyperfine field in PFN below $\sim$ 50 K indicates the increasing short-ranged correlations at $Fe^{3+}$ which eventually freeze below $T_{SG}$. With these approaches together, we can say that the PFN has a non-collinear AF phase in which SG contribution arises from the random fluctuations of $Fe^{3+}$ spins in transverse direction as depicted in fig. 9.9(b). Moreover, the two contributing hyperfine fields coincide at the base temperature and show a full moment confirming the homogeneity in the sample. This validaties the coexistence of AF and SG states on a microscopic level [6].

[1] M. Palassini, *et al.*, Phys. Rev. Lett. **82**, 5128 (1999). H.G. Ballesteros, *et al.*, Phys. Rev. B **62**, 14237 (2000).
[2] M. Gabay, *et al.*, Phys. Rev. Lett. **47**, 201 (1981). I.Ya. Korenblit, *et al.*, Zh. Eksp. Teor. Fiz. **93**, 1060 (1987).
[3] M. Nielsen, *et al.*, Phys. Rev. B **53**, 343 (1986).
[4] G.-M. Rotaru, *et al.*, Phys. Rev. B **79**, 184430 (2009).
[5] W. Kleemann, *et al.*, Phys. Rev. Lett **105**, 257202 (2010).
[6] S. Chillal, *et al.*, arXiv:1211.4203 (2012).

## 9.9 Phase transition in disordered uniaxial ferroelectric

D. Koulialias, S. Chillal

A large family of crystals with tetragonal tungsten bronze structure are uniaxial ferroelectrics. Due to the absence of a soft optic mode and the inherent disorder they are considered as unique electric charge realization of the Random-Field Ising model (RFIM). The phase transitions of variously doped model tungsten bronze $Sr_{0.61}Ba_{0.39}Nb_2O_6$ crystals are usually interpreted in this framework [1]. We have performed systematic neutron scattering experiments, showing that this approach primarily justified by previous bulk measurements, is actually not valid.

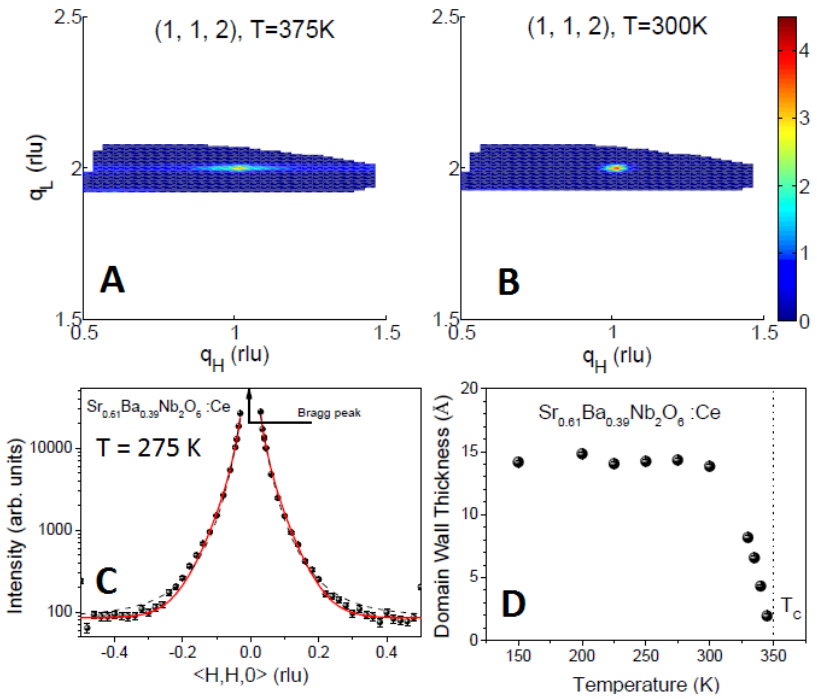


**Figure 9.10:** (A) Distribution of neutron DS around the (1,1,2) Bragg peak above $T_C$ (B) DS around the same Bragg peak but below $T_C$. (C) Typical scan through the (0,0,2) Bragg peak fitted using domain walls (red line) and RFIM (dashed black line) models. (D) Temperature dependence of the domain wall thickness. The arrow shows the center of the scan dominated by Bragg scattering.

We have studied the phase transition at $T_C$ = 350 K of a model $Sr_{0.61}Ba_{0.39}Nb_2O_6$ tungsten bronze crystal doped with 0.002 weight % of Ce, SBN:Ce. The experiments were performed at cold neutron 3-axis spectrometer TASP in the temperature range 150 K – 500 K. On cooling from $\sim$ 500 K, diffuse scattering (DS) occurs along the <H, H, 0> direction (see Fig. 1a). Above $T_C$ the DS is described by Lorentzian and is a signature of chain-like ionic correlations. Below $T_C$ the distribution of the DS changes drastically (cp. Fig. 1a & Fig. 1b). This is unusual, as the only symmetry element lost at $T_C$ is the inversion center, and this alone cannot affect the shape of the scattering. This finding indicates disorder-induced strong coupling of ferroelectric fluctuations to the phonons. Furthermore, the lineshape of the DS below $T_C$ is not Lorentzian-shaped. We have considered two approaches to treat this data: the RFIM model (Lorentzian raised to the power 1.5) and the ferroelectric domain-wall model. A typical fitted spectrum is shown in Fig. 1c. The spectra could be described by both models, however the RFIM fits lead to unphysical increase of the correlation length in ferroelectric phase to $\sim$ 100Å only; this value does not comply with macroscopic polarization detected in SBN:Ce [1]. We conclude that observed neutron DS is produced by the ferroelectric domain walls as opposite to the RFIM model. The domain wall thickness increases towards lower temperatures as shown in Fig. 1d and the values are similar to those obtained for pure SBN [2,3]. To summarize, we found no evidence that electric random-fields produce significant effects for the scattering properties of SBN:Ce, which contradicts the established framework for these materials.

[1] W. Kleemann et al., Phys. Rev. Lett. **97**, 065702 (2006); J. Banys et al., Phys. Rev. B **72**, 024106 (2005).
[2] F. Prokert et al., Physica Status Solidi **87**, 179 (1978)
[3] S. Gvasaliya et al., arXiv:1206.2012 (2012).

# Chapter 10

# Spin Physics and Imaging

(www.spin.ethz.ch/)

**Head**
Prof. Christian Degen

**Academic Staff**

| | | |
|---|---|---|
| Kevin Chang | Dr. Antoine Dussaux | Michael Loretz |
| Brad Moores | Dr. Paolo Navaretti | Tobias Rosskopf |
| Dr. Romana Schirhagl | Ye Tao | |

**Academic Guests**

| | | |
|---|---|---|
| Tobias Schoch | Demetra Perry | Kohei Ohashi |

**Technical Staff**

| | |
|---|---|
| Cecil Barengo | Julia Tamborini |

## 10.1 Spin Properties of Very Shallow Nitrogen Vacancy Defects in Diamond

K. Chang, M. Loretz, R. Schirhagl, Y. Tao, B. A. Moores, and C. L. Degen, in collaboration with B. K. Ofori-Okai (MIT), S. Pezzagna, K. Groot-Berning, J. Meijer (Bochum University).

Isolated defect spins in solids, such as phosphorus donors in silicon or the nitrogen-vacancy (NV) center in diamond, are considered important building blocks for future nanoscale devices, governed by quantum mechanics. In pure materials, defects can be so well-decoupled from their solid host that spin states approach a stability normally only found in dilute atomic vapors, including coherence times of milliseconds to seconds. Not surprisingly, atomic defects have over the last decade attracted increasing attention motivated by their potential for spin qubits in quantum information or for ultrasensitive magnetic detectors with nanometer spatial resolution.

The central challenge with many of these endeavors is to position the defect of interest in close proximity to other circuit elements while retaining their well-defined properties known from the bulk. On the one hand, close proximity is required for strong enough coupling. For example, for the direct coupling to nearby spin magnetic dipoles — which scales as $r^{-3}$, where $r$ is distance — efficient coupling is only achieved at nanometer separations. Furthermore, for scanning magnetometry applications $r$ directly sets the attainable spatial resolution. On the other hand, the coupling will almost always happen across a material interface and defects will have to be located within nanometers from a surface, potentially destabilizing the spin and limiting its usefulness.

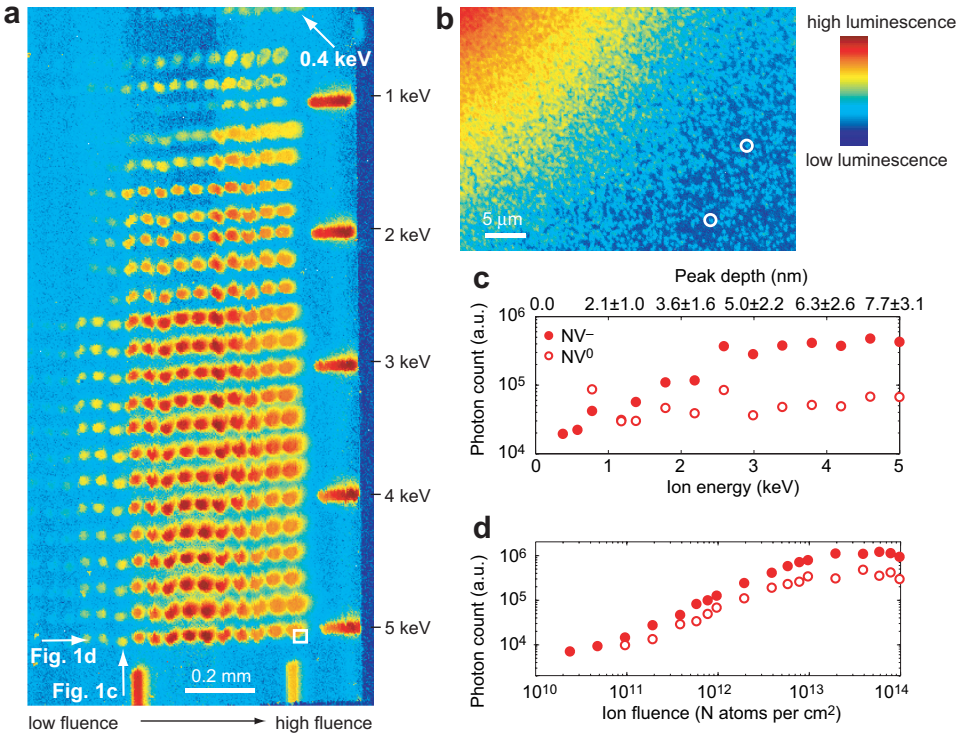


**Figure 10.1:** (a) Photoluminescence intensity map of an nitrogen-implanted diamond crystal, with implantation energies 0.4-5.0 keV (vertical direction) and fluence $10^{10} - 10^{14}$ ions per cm$^2$. Excitation wavelength was 532 nm and detection bandwidth 630-800 nm. Luminescence is entirely from NV centers. (b) Close up of an implantation spot at 5 keV (white square in (a)), resolving individual NV centers. (c) Concentration of NV$^-$ (full circles) and NV$^0$ (empty circles) centers as a function of ion energy, at a fluence of $8 \cdot 10^{11}$cm$^{-2}$. The relevant charge state for spin qubit experiments is NV$^-$. Luminescence intensity as a function of ion fluence at an energy of 5 keV.

In this project we have carried out a systematic study of the spin resonance properties of single NV centers at $\lesssim 10$ nm from the diamond surface. Defects were produced by low energy ion implantation (0.4-5 keV) and investigated by optically-detected magnetic resonance spectroscopy. As a first result, we found stable NV centers with a well-resolved electron spin resonance spectrum down to the lowest investigate implantation energy of 0.4 keV, corresponding to a mean defect depth of 1.1 nm. Second, we observed an extra line broadening for defects shallower than about 2 nm.

This broadening hints at the presence of an ubiquitous layer of magnetic surface states that fluctuate at a very fast correlation time, thus allowing the observation of spin resonance despite the close proximity to the surface. This observation of stable and well-behaved defects very close to the diamond surface is critical for single-spin sensors and devices requiring nanometer proximity to the target.

Literature Reference: B. K. Ofori-Okai et al., "Spin properties of very shallow nitrogen vacancy centers in diamond", Phys. Rev. **B 86**, 081406(R) (2012).

## 10.2 An RF spectrum analyzer using a single spin qubit as the sensor

M. Loretz, T. Rosskopf, C.L. Degen

Quantum systems have been recognized as extraordinarily sensitive detectors for weak magnetic and electric fields. Spin states in atomic vapors or flux states in superconducting quantum interference devices, for example, offer among the best sensitivities in magnetic field detection. Trapped ions or semiconductor quantum dots are investigated as ultrasensitive detectors for local electric fields. The tiny volume of single quantum systems, often at the level of atoms, furthermore offers interesting opportunities for ultrasensitive microscopies with nanometer spatial resolution.

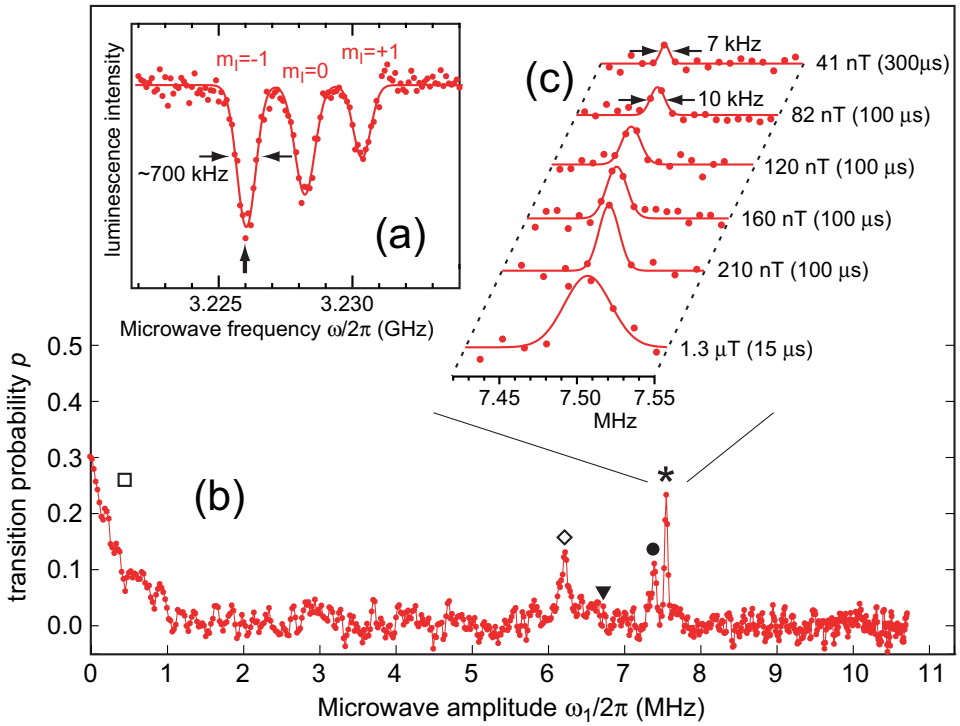


**Figure 10.2:** Example measurements on a single NV center in diamond. (a) Optically-detected electron spin resonance (ESR) spectrum of a single NV centers. Dots are data, solid lines are Gaussian fits. $m_I = \pm 1$, $m_I = 0$ indicate hyperfine lines ($a = 2.2$ MHz) associated with the $^{14}$N nuclear spin ($I = 1$). (b) RF magnetic noise spectrum recorded with a single NV center in the range 0-11 MHz. An artificial AC field of 7.5 MHz and $\sim 1.6\mu$T amplitude was purposely introduced to demonstrate the sensing capability (feature $\star$). Spin evolution time for field sensing was $\tau = 15\mu$s. (c) High-resolution spectra of the main peak ($\star$) for longer evolution times and weaker AC test fields. Dots are data, solid lines are Gaussian fits. Linewidths are full width at half maximum. Numbers indicate magnitude of AC field and spin evolution time $\tau$. A magnetic field of 41 nT was successfully detected at a spectral resolution of 7 kHz. Baseline noise corresponds to 8 nT at an integration time of 840 s.

In this project we have used the spin of a single, molecular "ion" trapped in a solid – a nitrogen-vacancy impurity (NV center) in a diamond crystal – as an atomic-sized magnetic field sensor. In particular, we have developed a simple

and robust spin manipulation protocol for the detection of weak radio-frequency magnetic fields. The method relies on spin locking, where the Rabi frequency of the spin is adjusted to match the MHz signal frequency. In a proof-of-principle experiment we detected a 7.5 MHz magnetic probe field of $\sim 40$ nT amplitude with $< 10$ kHz spectral resolution. The further prospect is to use rotating-frame magnetometry for performing high-resolution spectroscopy of nanoscale volumes of nuclear spin signals, eventually at the level of indidual nuclei.

Literature Reference: M. Loretz, T. Rosskopf, and C. L. Degen, "Radio-frequency magnetometry using a single electron spin", Phys. Rev. Lett. **110**, 017602 (2013).

## 10.3 Single-crystal diamond nanomechanical resonators with quality factors exceeding one million

Y. Tao, C.L. Degen

Diamond has gained a reputation as a uniquely versatile material, yet one that is intricate to grow and process. Resonating nanostructures made of single-crystal diamond are expected to possess excellent mechanical properties, including high quality factors and low dissipation. Our group has explored new approaches to batch fabricate single-crystal diamond cantilevers from ultrapure, low-doping starting material.

Single crystal diamond cantilevers fabricated had thickness down to 85 nm, thickness uniformity better than 20 nm, and lateral dimensions up to 240 $\mu$m. Measurements of mechanical properties between 0.1-300 K showed that these cantilevers can have exceptionally high quality factors. In particular, Q factors exceeding one million are found at room temperature, surpassing those of state-of-the-art single-crystal silicon cantilevers of similar dimensions by roughly an order of magnitude. Force sensitivities of a few hundred zeptonewtons ($10^{-21}$N) have resulted for the best cantilevers at millikelvin temperatures. Single-crystal diamond could thus directly improve existing force and mass sensors by a simple substitution of resonator material. The methods developed could be easily adapted for fabrication of high-end nanoelectromechanical systems (NEMS), optomechanical resonators, or nanophotonic devices with new applications in classical and quantum science.

Literature Reference: Y. Tao, J. M. Boss, B. A. Moores, and C. L. Degen, "Single crystal diamond nanomechanical resonators with quality factors exceeding one million", arXiv:1212.1347 (2012).

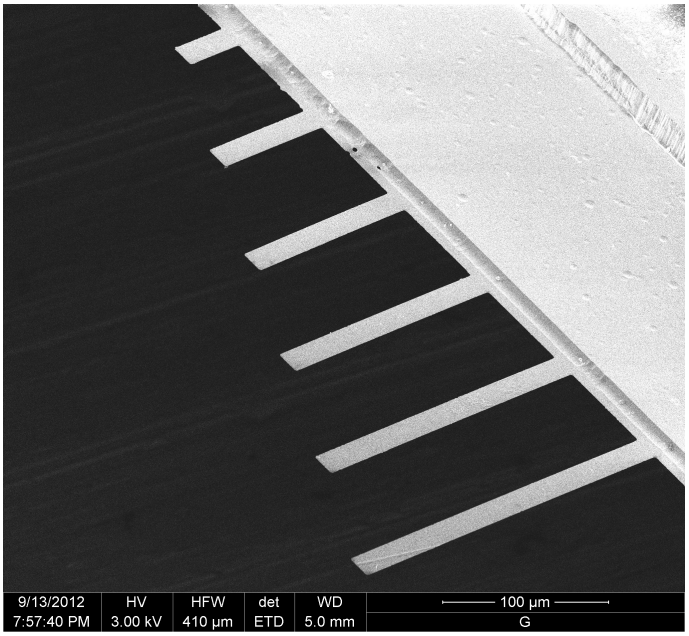


**Figure 10.3:** 100-nm-thick single crystal diamond cantilevers fabricated in our laboratory, in collaboration with FIRSTlab and Applied Diamond Inc.

# Chapter 11

# Publications


M. Baur, A. Fedorov, L. Steffen, S. Filipp, M.P. da Silva, and A. Wallraff
Benchmarking a Quantum Teleportation Protocol in Superconducting Circuits Using Tomography and an Entanglement Witness
Phys. Rev. Lett. **108**, 040502 (2012)

S. Berger, M. Pechal, S. Pugnetti, A.A. Abdumalikov Jr., L. Steffen, A. Fedorov, A. Wallraff, and S. Filipp
Geometric phases in superconducting qubits beyond the two-level-approximation
Phys. Rev. B **85**, 220502(R) (2012)

D. Bischoff, T. Krähenmann, S. Dröscher, M. A. Gruner, C. Barraud, T. Ihn, and K. Ensslin
Etched Graphene Nanoribbons on Hexagonal Boron Nitride Substrate
Appl. Phys. Lett. **101**, 203103 (2012)

A. Blachowski, K. Ruebenbauer, J. Zukrowski, Z. Bukowski, and J. Karpinski
Interplay Between Spin Density Wave and Superconductivity in '122' Iron Pnictides: Fe-57 Mossbauer Study
Acta Physica Polonica A **121**, 726-729 (2012)

A. A. Bush, V. N. Glazkov, M. Hagiwara, T. Kashiwagi, S. Kimura, K. Omura, L. A. Prozorova, L. E. Svistov, A. M. Vasiliev, and A. Zheludev
Magnetic phase diagram of the frustrated S=1/2 chain magnet $LiCu_2O_2$
Phys. Rev. B **85**, 054421 (2012)

M. Calamiotou, D. Lampakis, E. Siranidi, J. Karpinski, N.D. Zhigadlo, and E. Liarokapis
Pressure and doping dependent anisotropic compressibility of the $SmFeAsO_{1-x}F_x$ (x = 0.0-0.17) system
Physica C **483** ,136-139 (2012)

A. Calloni, R. Ferragut, A. Dupasquier, H. von Känel, A. Guiller, A. Rutz, L. Ravelli, and W. Egger
Characterization of vacancy-type defects in heteroepitaxial GaN grown by low-energy plasma-enhanced vapor phase epitaxy
Journal of Applied Physics **112**, 024510 (2012)

F. Casola, T. Shiroka, V. Glazkov, A. Feiguin, G. Dhalenne, A. Revcolevschi, A. Zheludev, H.-R. Ott, and J. Mesot
Dimensional crossover of spin chains in a transverse staggered field: an NMR study
Phys. Rev. B **86**, 165111 (2012)

J. Chang, E. Blackburn, A.T. Holmes, N.B. Christensen, J. Larsen, J. Mesot, R. Liang, D.A. Bonn, W.N. Hardy,

A. Watenphul, M. v. Zimmermann, E.M. Forgan, and S.M. Hayden
Direct observation of competition between superconductivity and charge density wave order in $YBa_2Cu_3O_y$
Nature Physics **8**, 871 (2012)

J. Chang, J.S. White, M. Laver, C.J. Bowell, S.P. Brown, A.T. Holmes, L. Maechler, S. Streassle, R. Gilardi, S. Gerber, T. Kurosawa, N. Momono, M. Oda, M. Ido, O.J. Lipscombe, S.M. Hayden, C.D. Dewhurst, R. Vavrin, J. Gavilano, J. Kohlbrecher, E.M. Forgan, and J. Mesot
Spin density wave induced disordering of the vortex lattice in superconducting $La_{2-x}Sr_xCuO_4$
Phys. Rev. B **85**, 134520 (2012)

K. Chen, W. Wang, J. Wu, D. Schuh, W. Wegscheider, T. Korn, and T. Lai
Transmission-grating-photomasked Transient Spin Grating and its Application to Measurement of Electron-spin Ambipolar Diffusion in (110) GaAs Quantum Wells
Optics Express **20**, 8192 (2012)

T. Choi, T. Ihn, S. Schön, and K. Ensslin
Counting Statistics in an InAs Nanowire Quantum Dot with a vertically coupled Charge Detector
Appl. Phys. Lett. **100**, 072110 (2012)

P. Das, C. Rastovski, T.R. O'Brien, K.J. Schlesinger, C.D. Dewhurst, L. De Beer-Schmitt, N. D. Zhigadlo, J. Karpinski, and M.R. Eskildsen
Observation of Well-Ordered Metastable Vortex Lattice Phases in Superconducting $MgB_2$ Using Small-Angle Neutron Scattering
Phys. Rev. Lett. **108**, 167001 (2012)

S. Dröscher, C. Barraud, K. Watanabe, T. Taniguchi, T. Ihn and K. Ensslin
Electron flow in split-gated bilayer graphene
New. J. Phys. **14**, 103007 (2012)

S. Dröscher, J. Güttinger, T. Mathis, B. Batlogg, T. Ihn, and K. Ensslin
High-frequency gate manipulation of a bilayer graphene quantum dot
Appl. Phys. Lett. **101**, 043107 (2012)

S. Dröscher, P. Roulleau, F. Molitor, P. Studerus, C. Stampfer, K. Ensslin, and T. Ihn
Quantum capacitance and density of states of graphene
Phys. Scr. T **146**, 014069 (2012), Proceedings of the Nobel Symposium on Graphene

S. Dröscher, J. Güttinger, T. Mathis, B. Batlogg, T. Ihn, and K. Ensslin
High-frequency gate manipulation of a bilayer graphene quantum dot
Appl. Phys. Lett. **101**, 043107 (2012)

A. Dusza, A. Lucarelli, A. Sanna, S. Massidda, J.-H. Chu, I.R. Fisher and L. Degiorgi
Anisotropic in-plane optical conductivity in detwinned $Ba(Fe_{1-x}Co_x)_2As_2$
New J. Phys. **14**, 023020 (2012)

C. Eichler, D. Bozyigit, and A. Wallraff
Characterizing quantum microwave radiation and its entanglement with superconducting qubits using linear detectors
Phys. Rev. A **86**, 032106 (2012)

C. Eichler, and A. Wallraff
Tomography schemes for characterizing itinerant microwave photon fields
Lecture notes for the Les Houches summer school 2011, to be published in Oxford university press (2012)

C. Eichler, C. Lang, J.M. Fink, J. Govenius, S. Filipp, and A. Wallraff
Observation of Entanglement between Itinerant Microwave Photons and a Superconducting Qubit
Phys. Rev. Lett. **109**, 240501 (2012)

C.V. Falub, H. von Känel, F. Isa, R. Bergamaschini, A. Marzegalli, D. Chrastina, G. Isella, E. Müller, P. Niedermann, and L. Miglio
Scaling hetero-epitaxy from layers to three-dimensional crystals
Science **335**, 1330 (2012)

A. Fedorov, L. Steffen, M. Baur, M.P. da Silva, and A. Wallraff
Implementation of a Toffoli gate with superconducting circuits
Nature **481**, 170-172 (2012)

A. Fognini, T. U. Michlmayr, T. Bähler, C. Wetli, A. Vateraus, and Y. Acremann
Magnetic pulser and sample holder for time and spin-resolved photoemission spectroscopy on magnetic materials
Review of Scientific Instruments **83**, 063906 (2012).

T. Frey, P. J. Leek, M. Beck, J. Faist, M. Büttiker, A. Wallraff, K. Ensslin, and T. Ihn
Quantum dot admittance probed at microwave frequencies with an on-chip resonator
Phys. Rev. B **86**, 115303 (2012)

T. Frey, P. J. Leek, A. Blais, M. Beck, T. Ihn, K. Ensslin, and A. Wallraff
Dipole-coupling of a double quantum dot to a microwave resonator
Phys. Rev. Lett. **108**, 046807 (2012)

J. Güttinger, F. Molitor, C. Stampfer, S. Schnez, A. Jacobsen, S. Dröscher, T. Ihn and K. Ensslin
Transport through graphene quantum dots
Rep. Prog. Phys. **75**, 126502 (2012)

V. N. Glazkov, T. S. Yankova, J. Sichelschmidt, D. Hüvonen, and A. Zheludev
Electron spin resonance study of anisotropic interactions in a two-dimensional spin gap magnet PHCC
Phys. Rev. B **85**, 054415 (2012)

R. S. Gonnelli, M. Tortello, D. Daghero, R.K. Kremer, Z. Bukowski, N.D. Zhigadlo, and J. Karpinski
Point-contact spectroscopy in Co-doped $CaFe_2As_2$: nodal superconductivity and topological Fermi surface transition
Superconductor Science & Technology **25**, 065007 (2012)

G. Granger, D. Taubert, C.E. Young, L. Gaudreau, A. Kam, S.A. Studenikin, P. Zawadzki, D. Harbusch, D. Schuh, W. Wegscheider, Z.R. Wasilewski, A.A. Clerk, S. Ludwig, and A.S. Sachrajda
Quantum Interference and Phonon-mediated Back-action in Lateral Quantum-dot Circuits
Nature Phyics **8**, 522 (2012)

M. Griesbeck, M.M. Glazov, A.Y. Sherman, D. Schuh, W. Wegscheider, C. Schüller, and T. Korn
Strongly Anisotropic Spin Relaxation Revealed by Resonant Spin Amplification in (110)GaAs Quantum Wells
Phys. Rev. B **85**, 085313 (2012)

Z. Guguchia, A. Shengelaya, A. Maisuradze, L. Howald, Z. Bukowski, M. Chikovani, H. Luetkens, S. Katrych, J.

Karpinski, and H. Keller
Muon-Spin Rotation and Magnetization Studies of Chemical and Hydrostatic Pressure Effects in $EuFe_2(As_{1-x}P_x)_2$
J. Supercond. Nov. Magn. **26**, 285-295 (2012)

J. Gutierrez, B. Raes, A.V. Silhanek, L.J. Li, N.D. Zhigadlo, J. Karpinski, J. Tempere, and V.V. Moshchalkov
Scanning Hall probe microscopy of unconventional vortex patterns in the two-gap $MgB_2$ superconductor
Phys. Rev. B **85**, 094511 (2012)

R. Hauert, C.V. Falub, G. Thorwarth, K. Thorwarth, C. Affolter, M. Stiefel, L.E. Podleska, and G. Taeger
Retrospective lifetime estimation of failed and explanted diamond-like carbon coated hip joint balls
Acta Biomaterialia **8**, 3170 (2012)

R. Hauert, G. Thorwarth, U. Mueller, M. Stiefel, C.V. Falub, K. Thorwarth, and T.J. Joyce
Analysis of the in-vivo failure of the adhesive interlayer for a DLC coated articulating metatarsophalangeal joint
Diamond and Related Materials **25**, 34 (2012)

S. Hellmüller, M. Pikulski, T. Müller, B. Küng, G. Puebla-Hellmann, A. Wallraff, M. Beck, K. Ensslin, and T. Ihn
Optimization of sample chip design for stub-matched radio-frequency reflectometry measurements
Applied Physics Letters **101**, 042112 (2012)

S.D. Hogan, J.A. Agner, F. Merkt, T. Thiele, S. Filipp, and A. Wallraff
Driving Rydberg-Rydberg Transitions from a Coplanar Microwave Waveguide
Phys. Rev. Lett. **108**, 063004 (2012)

P-A. Huynh, F. Portier, H. le Sueur, G. Faini, U. Gennser, D. Mailly, F. Pierre, W. Wegscheider, and P. Roche
Quantum Coherence Engineering in the Integer Quantum Hall Regime
Phys. Rev. Lett. **108**, 256802 (2012)

D. Hüvonen, S. Zhao, G. Ehlers, M. Månsson, S. N. Gvasaliya, and A. Zheludev
Excitations in a quantum spin liquid with random bonds
Phys. Rev. B **86** 214408 (2012)

D. Hüvonen, S. Zhao, M. Månsson, T. Yankova, E. Ressouche, C. Niedermayer, M. Laver, S. N. Gvasaliya, and A. Zheludev
Field-induced criticality in a gapped quantum magnet with bond disorder
Phys. Rev. B **85**, 100410(R) (2012)

T. Ihn, S. Dröscher, S. Schnez, H. Knowles, J. G üttinger, M. Huefner, C. Stampfer, Y. Meir, and K. Ensslin
Electronic transport in graphene nanostructures on $SiO_2$
Solid State Commun. **152**, 1306 (2012)

H. Ishiwata, Y. Acremann, A. Scholl, E. Rotenberg, O. Hellwig, E. Dobisz, A. Doran, B. Tkachenko, A. Fokin, P. Schreiner, J. Dahl, R. Carlson, N. Melosh, Z. Shen, and H. Ohldag
Diamondoid coating enables disruptive approach for chemical and magnetic imaging with 10 nm spatial resolution
Appl. Phys. Lett. **101**, 163101 (2012)

A. Jacobsen, P. Simonet, K. Ensslin and T. Ihn
Transport in a three-terminal graphene quantum dot in the multi-level regime
New. J. Phys. **14**, 023052 (2012)

B. Küng, C. Rössler, M. Beck, J. Faist, T. Ihn, K. Ensslin
Quantum dot occupation and electron dwell time in the cotunneling regime
New. J. Phys. **14**, 083003 (2012)

B. Küng, C. Rössler, M. Beck, M. Marthaler, D.S. Golubev, Y. Utsumi, T. Ihn, K. Ensslin
Irreversibility on the Level of Single-Electron Tunneling
Phys. Rev. X **2**, 011001 (2012)

J. Karpinski
High pressure in the synthesis and crystal growth of superconductors and III-N semiconductors
Philosophical Magazine **92**, 2662, (2012)

J. Kehl, G. Schiltz, A. Reinhardt, and T. Korner,
"Innovate Teaching". Studierende mit einem Ideenwettbewerb an der Lehrinnovation beteiligen
Digitale Medien - Werkzeuge für exzellente Forschung und Lehre (2012)

K. Kowalik-Seidl, X.P. Vögele, B.N. Rimpfl, G.J. Schinner, D. Schuh, W. Wegscheider, A.W. Holleitner, and J.P. Kotthaus
Tunable Photoemission from an Excitonic Antitrap
Nanoletters **12**, 326 (2012)

O. Krupin, Y. Acremann *et al.*
Temporal cross-correlation of x-ray free electron and optical lasers using soft x-ray pulse induced transient reflectivity
Optics express **20**, 11396 (2012)

G. Lamura, T. Shiroka, S. Cahen, H. Rida, N. Emery, J.-F. Marêché, P. Lagrange, and C. Hérold
The zero-field magnetic ground state of $EuC_6$ investigated by muon spectroscopy
Carbon **50**, 3995 (2012)

M. Lavagnini, F. Pfuner, R. Monnier, L. Degiorgi, H.-M. Eiter, L. Tassini, B. Muschler, R. Hackl, J.-H. Chu, N. Ru, K.Y. Shin and I.R. Fisher
Infrared and Raman investigation of the charge-density-wave state in rare-earth tri-telluride compounds
Physica B **407**, 1864 (2012)

W.J. Legerstee, J. de Roode, A. Anastasopol, C.V. Falub, and S.W.H. Eijt
In-situ hydrogen sorption 2D-ACAR facility for the study of metal hydrides for hydrogen storage
Physics Procedia **35**, 22 - 27 (2012)

J.C. Loudon, C.J. Bowell, N.D. Zhigadlo, J. Karpinski, and P.A. Midgley
Imaging flux vortices in $MgB_2$ using transmission electron microscopy
Physica C: Superconductivity **474**, 18-20 (2012)

T. Müller, J. Güttinger, D. Bischoff, S. Hellmüller, K. Ensslin, and T. Ihn
Fast detection of single-charge tunneling to a graphene quantum dot in a multi-level regime
Appl. Phys. Lett. **101**, 012104 (2012)

C. Marini, D. Chermisi, M. Lavagnini, D. Di Castro, C. Petrillo, L. Degiorgi, S. Scandolo and P. Postorino
High-pressure phases of crystalline tellurium: a combined Raman and ab initio study
Phys. Rev. B **86**, 064103 (2012)

T. Mathis, K. Mattenberger, P.J.W. Moll, and B. Batlogg
Tetrathiofulvalene and tetracyanoquinodimethane crystals: Conducting surface versus interface
Appl. Phys. Lett. **101**, 023302 (2012)

J.A. Mlynek, A.A. Abdumalikov, J.M. Fink, L. Steffen, M. Baur, C. Lang, A.F. van Loo, and A. Wallraff
Demonstrating $W$-type entanglement of Dicke states in resonant cavity quantum electrodynamics
Phys. Rev. A **86**, 053838 (2012)

P.J.W. Moll, L. Balicas, V. Geshkenbein, G. Blatter, J. Karpinski, N.D. Zhigadlo, and B. Batlogg
Transition from slow Abrikosov- to fast moving Josephson-vortices in iron pnictide superconductors
Nature Materials **12**, 134-138 (2013)

S. Mühlbauer, S. Gvasaliya, E. Pomjakushina, and A. Zheludev
Phase Diagram of the Dzyaloshinskii-Moriya Helimagnet $Ba_2CuGe_2O_7$ in Canted Magnetic Fields
Phys. Rev. B **86**, 024417 (2012)

B.K. Ofori-Okai, S. Pezzagna, K. Chang, M. Loretz, R. Schirhagl, Y. Tao, B.A. Moores, K. Groot-Berning, J. Meijer, and C. L. Degen
Spin properties of very shallow nitrogen vacancy centers in diamond
Phys. Rev. Lett. **102**, 081406 (2012)

N. Pascher, D. Bischoff, T. Ihn, and K. Ensslin
Scanning gate microscopy on a graphene nanoribbon
Appl. Phys. Lett. **101**, 063101 (2012)

M. Pechal, S. Berger, A.A. Abdumalikov Jr., A. Wallraff, and S. Filipp
Geometric phase and non-adiabatic effects in an electronic harmonic oscillator
Phys. Rev. Lett. **108**, 170401 (2012)

F. Pfuner, S.N. Gvasaliya, O. Zaharko, L. Keller, J. Mesot, V. Pomjakushin, J.-H. Chu, I.R. Fisher and L. Degiorgi
Incommensurate magnetic order in $TbTe_3$
J. Phys.: Condens. Matter **24**, 036001 (2012)

L. Prechtel, L. Song, D. Schuh, P. Ajayan, W. Wegscheider, and A.W. Holleitner
Time-resolved Ultrafast Photocurrents and Terahertz Generation in Freely Suspended Graphene
Nature Communications **3**, 646 (2012)

G. Puebla-Hellmann, and A. Wallraff
Realization of GHz-frequency impedance matching circuits for nano-scale devices
Applied Physics Letters **101**, 053108 (2012)

D. L. Quintero-Castro, B. Lake, A. T. M. N. Islam, E. M. Wheeler, C. Balz, M. Mansson, K. C. Rule, S. Gvasaliya, and A. Zheludev
Asymmetric Thermal Lineshape Broadening in a Gapped 3-Dimensional Antiferromagnet - Evidence for Strong Correlations at Finite Temperature
Phys. Rev. Lett. **109**, 127206 (2012)

A.N. Ramanayaka, R.G. Mani, J.I. Inarrea, and W. Wegscheider
Effect of Rotation of the Polarization of Linearly Polarized Microwaves on the Radiation-induced Magnetoresistance

Ocillations
Phys. Rev. B **85**, 205315 (2012)

E. Razzoli, M. Kobayashi, V. N. Strocov, B. Delley, Z. Bukowski, J. Karpinski, N.C. Plumb, M. Radovic, J. Chang, T. Schmitt, L. Patthey, J. Mesot, and M. Shi
Bulk Electronic Structure of Superconducting $LaRu_2P_2$ Single Crystals Measured by Soft-X-Ray Angle-Resolved Photoemission Spectroscopy
Phys. Rev. Lett. **108**, 257005 (2012)

J. M. Ripalda, A.M. Sanchez, A.G. Taboada, A. Rivera, B. Alén, Y. González, L. González, F. Briones, T. J. Rotter, and G. Balakrishnan
Relaxation dynamics and residual strain in metamorphic AlSb on GaAs
Appl. Phys. Lett. **100**, 012103 (2012)

G. Scalari, C. Maissen, D. Turcinkova, D. Hagenmüller, S. De Liberato, C. Ciuti, C. Reichl, D. Schuh, W. Wegscheider, M. Beck, and J. Faist
Ultrastrong Coupling of the Cyclotron Transition of a 2D Electron Gas to a THz Metamaterial
Science **335**, 1323 (2012)

G. Schiltz, and B. Volk
Coupling local and central support structures. A model to ensure teaching support and quality assurance in research universities
9th ICED Conference 2012: Across the Globe Higher Education Learning and Teaching (2012)

D. Schmidiger, P. Bouillot, S. Mühlbauer, S. Gvasaliya, C. Kollath, T. Giamarchi, and A. Zheludev
Spectral and thermodynamic properties of a strong-leg quantum spin ladder
Phys. Rev. Lett. **108**, 167201 (2012)

S. Schnez, J. G üttinger, F. Molitor, C. Stampfer, M. Huefner, T. Ihn and K. Ensslin
Graphene quantum dots: transport experiments and local imaging
Chapter in Book on "Quantum dots: optics, electron transport and future applications", Cambridge University Press 2012, p. 296, Ed. A. Tartakovskii

J. Shiogai, M. Ciorga, M. Utz, D. Schuh, T. Arakawa, M. Kohda, K. Kobayashi, T. Ono, W. Wegscheider, D. Weiss, and J. Nitta
Dynamic Nuclear Spin Polarization in an All-semiconductor Spin Injection Device with (Ga,Mn)As/n-GaAs Spin Esaki Diode
App. Phys. Lett. **101**, 212402 (2012)

T. Shiroka, R. Fittipaldi, M. Cuoco, R. De Renzi, Y. Maeno, R.J. Lycett, S. Ramos, E.M. Forgan, C. Baines, A. Rost, V. Granata, and A. Secchione
$\mu$SR studies of superconductivity in eutectically grown mixed ruthenates
Physical Review B **85**, 134527 (2012)

T. Shiroka, F. Casola, J. Mesot, W. Bachmann, and H.-R. Ott
A two-axis goniometer for low-temperature NMR measurements on single crystals
Rev. Sci. Instrum. **83**, 093901 (2012)

T. Shiroka, F. Casola, V. Glazkov, A. Zheludev, A. Revcolevschi, G. Dhalenne, K. Prša, H.-R. Ott, and J. Mesot
Experimental investigation of the low-temperature features of a random Heisenberg spin chain
J. Phys.: Conf. Series **400**, 032089 (2012)

M. Stallhofer, Ch. Kastl, M. Braendlein, Ch. Karnetzky, D. Schuh, W. Wegscheider, and A.W. Holleitner
Propagation Length of Mesoscopic Photocurrents in a Two-dimensional Electron Gas
Phys. Rev. B. **86**, 115313 (2012)

L. Steffen, M.P. da Silva, A. Fedorov, M. Baur, and A. Wallraff
Experimental Monte Carlo Quantum Process Certification
Phys. Rev. Lett. **108**, 260506 (2012)

V.M. Stojanovic, A. Fedorov, A. Wallraff, and C. Bruder
Quantum-control approach to realizing a Toffoli gate in circuit QED
Phys. Rev. B **85**, 054504 (2012)

M. Thede, F. Xiao, Ch. Baines, C. Landee, E. Morenzoni, and A. Zheludev
Ordering in weakly coupled random singlet spin chains
Phys. Rev. B **86**, 180407 (2012)

P.H. Tobash, F. Ronning, J.D. Thompson, B.L. Scott, P.J.W Moll, B. Batlogg, and E.D. Bauer
Single crystal study of the heavy-fermion antiferromagnet $CePt_2In_7$
J. Phys.: Condens. Matter **24**, 015601 (2012)

M. Tortello, D. Daghero, G.A. Ummarino, V.A. Stepanov, N.D. Zhigadlo, J. Karpinski, J. Jiang and R.S. Gonnelli
Point-Contact Andreev-Reflection Spectroscopy in Fe-Based Superconductors: Multigap Superconductivity and Strong Electron-Boson Interaction
Journal of Superconductivity and Novel Magnetism **25**, 1297-1301 (2012)

H. Von Känel
Merging incompatible materials
Europhysics News **43**, 4 (2012)

P. Wachter
Physical Properties of stoichiometric GdN single crystals
Results in Physics **2**, 90 (2012)

P. Wachter, and B. Bucher
Exciton condensation and its influence on the specific heat
Physica B **408**, 51-57 (2012)

C. Wagner, A. Vaterlaus
Promoting formative assessment in high school teaching of physics
Latin-American journal of physics education **6**, 410 (2012)

M.P. Walser, U. Siegenthaler, V. Lechner, D. Schuh, S.D. Ganichev, W. Wegscheider, and G. Salis
Dependence of the Dresselhaus Spin-orbit Interaction on the Quantum Well Width
Phys. Rev. B **86**, 195309 (2012)

M.P. Walser, C. Reichl, W. Wegscheider, and G. Salis
Direct Mapping of the Formation of a Persistent Spin Helix
Nature Physics **8**, 757 (2012)

T. Wang, A. Fognini, Y. Acremann *et al.*
Femtosecond single-shot imaging of nanoscale ferromagnetic order in Co/Pd multilayers using resonant x-ray holography
Phys. Rev. Lett **108**, 267403 (2012)

T. Yankova, D. Hüvonen, S. Mühlbauer, D. Schmidiger, E. Wulf, S. Zhao, A. Zheludev, T. Hong, V. O. Garlea, R. Custelcean, and G. Ehlers
Crystals for neutron scattering studies of quantum magnetism
Philosophical Magazine **92**, 2629 (2012)

I. A. Zaliznyak, Z. J. Xu, J. S. Wen, J. M. Tranquada, G. D. Gu, V. Solovyov, V. N. Glazkov, A. I. Zheludev, V. O. Garlea, and M. B. Stone
Continuous magnetic and structural phase transitions in $Fe_{1+y}Te$
Phys. Rev. B **85**, 085105 (2012)

N.D. Zhigadlo, S. Weyeneth, S. Katrych, P.J.W. Moll, K. Rogacki, S. Bosma, R. Puzniak, J. Karpinski, and B. Batlogg
High-pressure flux growth, structural, and superconducting properties of LnFeAsO (Ln = Pr, Nd, Sm) single crystals
Phys. Rev. B **86**, 21 214509, 1-13 (2012)

T. Zimmerling, K. Mattenberger, M. Doebeli, M.J. Simon, and B. Batlogg
Deep trap states in rubrene single crystals induced by ion radiation
Phys. Rev. B **85**, 134101 (2012)

# Chapter 12

# Presentations

**(⋆ = invited talk)**

***=eingeladen**

## 12.1 Talks

⋆ Acremann, Y
Towards a direct ultrafast measurement of the magnetization
Science at FELs, DESY, Hamburg, 17.07.2012

⋆ Acremann, Y
Magnetization dynamics seen by x-rays (invited)
SPIE Optics + Photonics, San Diego, California United States, 14.08.2012

Baer, S.
Quantum dots in the quantum Hall regime
Workshop on Quantum Systems and Technology, Monte Verita, Ascona, Switzerland, 18.06.2012

Baer, S.
Quantum dots in the quantum Hall regime
31st International Conference on the Physics of Semiconductors, Zurich, Switzerland, 29.07.2012

Barraud, C.
Transport in BN/graphene heterostructures
Quantum Innovator Workshop, Waterloo, Canada, 06.09.2012

Barraud, C.
Split-gates on bilayer graphene
ISGD 2012, Saclay, France, 05.11.2012

Barraud, C.
Split-gates in bilayer graphene devices
3rd International Symposium on Graphene Devices, Saint Aubin, France, 5.11.2012

⋆ Basset, J.
Dipole coupling of a double quantum dot to a microwave resonator
The Science of Nanostructures: New Frontiers in the Physics of Quantum Dots, Chernogolovka, Russia, 10.09.2012

⋆ Batlogg, B.
Research Integrity
Int. Workshop on Novel Materials and Superconductors, Planneralm, Austria, 13.02.2012

⋆ Batlogg, B.
Wieviel Technik brauchen wir?
Kantonsschule St. Gallen, Schweiz. Akad. Wissenschaften/Engineering, St. Gallen, Switzerland, 12.03.2012

⋆ Batlogg, B.
Quasiparticle mass enhancement and band width renormalization: comparing Ru- and Fe-pnictides
Technical University Stockholm, Stockholm, Sweden, 03.04.2012

⋆ Batlogg, B.
Organic semiconductor research: basic science and applications
Chinese Academy of Sciences, Ningbo Institute of Materials Technology and Engineering (NIMTE), Ningbo, China, 04.06.2012

⋆ Batlogg, B.
Critical currents and vortex phase transition in Fe-based superconductors
Institute of Physics, Chinese Academy of Sciences, Beijing, China, 06.06.2012

⋆ Batlogg, B.
Improved Organic FETs through Charge Trap Analysis and Reduction
Annual World Congress of Advanced Materials-2012, Beijing, China, 07.06.2012

⋆ Batlogg, B.
Fe-based and related superconductors in high magnetic fields: mass renormalization, critical fields and critical currents
Condensed Matter Colloquium, Los Alamos National Laboratory, NM, USA, 22.08.2012

⋆ Batlogg, B.
Charge transport and charge traps in PDIF-CN2 : a n-type semiconductor in three modifications compared to p-type organic semiconductors
Int. Workshop ”Multifunctional Hybrids And Organics”, Ischia, Italy, 23.10.2012

⋆ Batlogg, B.
Charge trapping and gate-bias stress: comparing n-type and p-type organic semiconductors
Int. Symposium on Organic Transistors and Functional Interfaces OFET 2012, Princeton, USA, 27.10.2012

⋆ Batlogg, B.
Charge Transport and Charge Trapping in n- and p-type Organic Semiconductors
MRS Materials Research Society Conference, Boston, USA, 23.11.2012

Berger, S.
Geometric Phases, Noise and Non-adiabatic Effects in Multi-level Superconducting Systems
APS March Meeting, Boston, USA, 28.02.2012

Berger, S.
Geometric phases beyond the two level-approximation
QSIT Junior Meeting, Passugg, Switzerland, 03.07.2012

Bischoff, D.
Electrical transport through graphene nanoribbons characterized with static and movable gates
17th International Winterschool on New Developments in Solid State Physics, Mauterndorf, Austria, 12.02.2012

Bischoff, D.
Etched graphene nanoribbons on hexagonal boron nitride
Graphene week, Delft, 04.06.2012

Bischoff, D.
Graphene nanoribbons on BN substrates
31st International Conference on the Physics of Semiconductors, Zurich, Switzerland, 29.07.2012

Cabrera, H.
Electrostatic characterization of Near-Field-Emission SEM
APS March Meeting, Boston, USA, 28.02.2012

Cabrera, H.
Electrostatic characterization of Near Field-Emission Scanning Electron Microscopy
SPG-Jahrestagung in Zürich, 21.06.2012

⋆ Casola, F.
Site-Disorder and Frustration: a Case Study of Quantum Domain Walls in 1D Magnetic Insulators
EuroMagnet II User Meeting, Grenoble, France, 14.06.2012

Casola, F.
Stability of Incommensurate Field-Induced Magnetic Order Upon Site-Disorder
19th International Conference on Magnetism (ICM), Busan, South Korea, 12.07.2012

Chillal, S.
Investigation of magnetic phase transitions in B-site disordered $PbB_xB'_{1-x}O_3$ (B = Fe, Co and B' = Nb, Ta)
APS March Meeting 2012, Boston, USA, 27.02.2012

Choi, T.
Counting statistics of single electron transport in nanowire quantum dots
Industry day, ETH Zurich, Switzerland, 7.09.2012

Choi, T.
Counting Statistics in an InAs Nanowire Quantum Dot with a vertically coupled Charge Detector
31st International Conference on the Physics of Semiconductors, Zurich, Switzerland, 29.07.2012

De Pietro, L.
Chemical Contrast in Near-Field-Emission SEM
APS March Meeting 2012, Boston, USA, 28.02.2012

⋆ De Pietro, L.
Festkörper - Was verstehen die Physiker darunter?
Seminar 18.04.12, Gmür & Geschwentner Architekten AG, 18.04.2012

De Pietro, L.
New Developments in Near Field-Emission Scanning Electron Microscopy
SPS Annual Meeting 2012, 21.06.2012

De Pietro, L.
Near Field-Emission Scanning Electron Microscopy
SPS Annual Meeting 2012, 21.06.2012

⋆ Degen, C.
Workshop on the Composition and Structure of Small Volumes, Eugene OR, USA, 17.09.2012

⋆ Degen, C.
Seminar for Biomedical Engineering, ETH Zurich, Switzerland, 31.05.2012

⋆ Degen, C.
QuASAR meeting, Harvard Univeristy, Cambridge, USA, 02.02.2012

⋆ Degiorgi, L.
Anisotropic charge dynamics in iron-pnictide superconductors
International Workshop on Superconductivity in iron-based compounds, Munich, Germany, March 21-23 2012

Degiorgi, L.
Spectroscopic investigations of the broken symmetry ground states in rare-earth tritellurides
Spring Meeting of the Materials Research Society, San Francisco, U.S.A., April 9-13 2012

⋆ Degiorgi, L.
The charge dynamics of iron-pnictide superconductors
Spring Meeting of the Materials Research Society, San Francisco, U.S.A., April 9-13 2012

⋆ Degiorgi, L.
Anisotropic charge dynamics in detwinned $Ba(Co_xFe_{1-x})_2As_2$
International Conference on Superconductivity and Magnetism (ICSM2012), Istanbul, Turkey, April 29- May 4 2012

⋆ Degiorgi, L.
Anisotropic charge dynamics in detwinned $Ba(Co_xFe_{1-x})_2As_2$
International School of Solid State Physics, Phase separation and superstripes in high temperature superconductors and related materials, Erice, Italy, July 11-17 2012

⋆ Degiorgi, L.
Anisotropic in-plane optical conductivity in detwinned iron-pnictides
International Conference on Low Energy Electrodynamics in Solids (LEES), Napa, USA, July 22-27 2012

⋆ Degiorgi, L.
Anisotropic in-plane optical conductivity in detwinned iron-pnictides
$24^{th}$ General Conference of the Condensed Matter Division of the European Physical Society, Edinburgh, Scotland, September 3-7 2012

⋆ Degiorgi, L.
Anisotropic charge dynamics in detwinned $Ba(Co_xFe_{1-x})_2As_2$
Conference on Electronic States and Phases Induced by Electric or Optical Impacts, Orsay-Paris, France, September

10-14 2012

⋆ Eichler, C.
Observation of Entanglement between a superconducting Qubit and an Itinerant Microwave Field
QSIT conference, Centro Stefano Franscini, Monte VeritÃ , Switzerland, 17.06.2012

Eichler, C.
Observation of Entanglement between a superconducting Qubit and an Itinerant Microwave Field
Walther Meissner Institut Munich, Germany, 29.06.2012

⋆ Ensslin, K.
Transport through three-terminal graphene quantum structures
Conference on ”The Physics of Graphene”, Kavli Institute for Theoretical Physics, University of California, Santa Barbara, USA, 9.01.2012

⋆ Ensslin, K.
Dipole coupling of a quantum dot to a microwave resonator
CNSI seminar, University of California, Santa Barbara, USA, 13.01.2012

⋆ Ensslin, K.
Graphene Quantum Circuits
International Physics School, Fundamentals of Nanoelectronics, Tenerife, Spain, 12.02.2012

⋆ Ensslin, K.
Keynote lecture: Quantum Science and Technology
First ETH-Japan Symposium for Academic Exchanges, ETH Zurich, Switzerland, 07.03.2012

⋆ Ensslin, K.
Graphene quantum structures
Workshop on ”Exploring the Potential of Graphene”, Swiss Academy of Sciences, Bern, 08.03.2012

⋆ Ensslin, K.
Irreversibility in single-electron tunneling
Microkelvin 2012 Workshop, Smolenice, Slovakia, 18.03.2012

⋆ Ensslin, K.
Irreversibility in single-electron tunneling
Workshop on ”Nonequilibrium Transport in Low-Dimensional Systems”, Kfar Blum, Israel, 29.04.2012

⋆ Ensslin, K.
Time-dependent single-electron transport: irreversibility and out-of-equilibrium properties
Physics Colloquium, KIT Karlsruhe, Germany, 11.05.2012

⋆ Ensslin, K.
Quantenphysik auf einem Chip
Physikalische Gesellschaft Zürich, Switzerland, 24.05.2012

⋆ Ensslin, K.
Graphene quantum structures
4th International Conference ”Smart Materials, Structures and Systems”, Montecatini, Italy, 10.06.2012

⋆ Ensslin, K.
Time-dependent single-electron transport: Irreversibility and out-of-equilibrium properties
Physics Colloquium, RWTH Aachen, Germany, 25.06.2012

⋆ Ensslin, K.
Waren Sie schon einmal an zwei Orten gleichzeitig? Quantenphysik und Informationsverarbeitung
Volkshochschule Zurich, Switzerland, 27.06.2012

⋆ Ensslin, K.
Time-dependent single-electron transport: irreversibility and out-of-equilibrium properties
Colloquium, Institute for Quantum Computing, Waterloo, Canada, 27.08.2012

⋆ Ensslin, K.
Microwave excitation of semiconductor quantum dots
NRC Ottawa, Canada, 28.08.2012

⋆ Ensslin, K.
Dipole-coupling of a double quantum dot to a microwave resonator
International Workshop on ”Quantum Noise and Measurement in Engineered Electronic Systems”, Dresden, Germany, 8.10.2012

⋆ Ensslin, K.
Dipole-coupling of a double quantum dot to a microwave resonator
Symposium on ”Quantum Coherent Structures”, Leipzig, Germany, 04.10.2012

⋆ Ensslin, K.
Electron counting in semiconductor quantum structures
EMPA PhD Students Symposium 2012, Dübendorf, Switzerland, 13.11.2012

⋆ Ensslin, K.
Electron counting in semiconductor quantum structures
Physics Colloquium, Univ. of Würzburg, Germany, 17.12.2012

⋆ Ensslin, K
Time-dependent single-electron transport: irreversibility and out-of-equilibrium properties
Quantum Lunch, McGill University, Montreal, Canada, 29.08.2012

⋆ Erbudak, M.
Crystal formations on quasicrystal surfaces
Cukurova Uni, Adana, Turkey, 12. 03. 2012

⋆ Erbudak, M.
Efficinet packing of natural particles and quasicrystals
Hacettepe University, Ankara, Turkey, 20.03.2012

⋆ Erbudak, M.
Ordered film growth on quasicrystal surfaces
Hacettepe University, Ankara, Turkey, 21.03.2012

⋆ Erbudak, M.
Stable and facetting quasicrystal surfaces
Hacettepe University, Ankara, Turkey, 22.03.2012

Erbudak, M.
Real-space observation of inclined planes in the decagonal quasicrystal AI70Co 15Nil 5
3rd Turkish Crystallographic Meeting, Izmir, Turkey, 8.06.2012

⋆ Erbudak, M.
Use of electrons vs photons in surface spectroscopy
Istanbul Technical Uni., Istanbul, Turkey, 18.12.2012

⋆ Erbudak, M.
Ethic in science
Science Academy, Istanbul, Turkey, 22.12.2012

Falub, C.V.
Space-filling Arrays of Three-Dimensional Epitaxial Ge and $Si_{1-x}Ge_x$ Crystals
International Silicon-Germanium Technology and Device Meeting, Berkeley, CA, USA, 04.06.2012

Falub, C.V.
Space-filling arrays of three-dimensional epitaxial crystals
31. Int. Conference on the Physics of Semiconductors (ICPS 2012), ETH Zurich, Switzerland, 29.07.2012

⋆ Falub, C.V.
Three-Dimensional Heteroepitaxy: A New Path for Monolithically Integrating Mismatched Materials with Silicon
35th International Semiconductor Conference (CAS-2012), Sinaia, Romania, 15.10.2012

⋆ Falub, C.V.
Is Silicon Age Coming to an End?
The INNOLEC Lectures "Advanced Methods in Semiconductor Technology", Masaryk University, Brno, Czech Republic, 05.12.2012

⋆ Falub, C.V.
Marrying Incompatible Couples: Mismatched Materials
The INNOLEC Lectures "Advanced Methods in Semiconductor Technology", Masaryk University, Brno, Czech Republic, 06.12.2012

⋆ Fedorov, A.
Implementation of the Toffoli gate in circuit QED architecture
SOLID Topical Workshop on Josephson Junction Circuits: Coherence, Control, Correction, and Communication, Delft University of Technology, Delft, Netherlands, 16.01.2012

⋆ Fedorov, A.
Multi-qubit gates in circuit QED
2nd international SOLID workshop, Phelma Polygone, Grenoble, France, 20.02.2012

Fedorov, A.
Implementation of a Toffoli Gate with Superconducting Circuits
APS March Meeting, Boston, USA, 27.02.2012

⋆ Fedorov, A.
Multi-Qubit Gates and Multi-Qubit Cooperative Effects in Circuit QED
Institut für Theoretische Festkörperphysik Universität Karlsruhe, Germany, 10.04.2012

Feil, T.
Raman spectroscopy of quantum Hall electronic excitations
2nd NCCR QSIT General Meeting, Arosa, Switzerland, 1.2.2012

⋆ Filipp, S.
Hybrid Cavity QED with Rydberg Atoms
SOLID Topical Workshop on Josephson Junction Circuits: Coherence, Control, Correction, and Communication, Delft University of Technology, Delft, Netherlands, 16.01.2012

Filipp, S.
Hybrid Cavity QED with Rydberg Atoms and Circuits
SOLID Topical Workshop on Josephson Junction Circuits: Coherence, Control, Correction, and Communication, Delft University of Technology, Delft, Netherlands, 17.01.2012

Filipp, S.
Observation of the Geometric Phase of a Harmonic Oscillator in Circuit Quantum Electrodynamics
76. Jahrestagung der DPG und DPG-Frühjahrstagung, Berlin, Germany, 26.03.2012

⋆ Filipp, S.
Geometric phases in circuit Quantum Electrodynamics
Workshop on the Quantum Physics of Phase, Stockholm, Sweden, 23.04.2012

⋆ Filipp, S.
Measurement of Geometric Phases in Circuit Quantum Electrodynamics
Quantum Chemistry Seminar, invited by E. Sjöqvist, Uppsala University, Sweden, 27.04.2012

Filipp, S.
Collective States in Circuit QED
Workshop on the dynamics and asymptotics in the Dicke model and quantum networks, Matrahaza, Hungary, 03.05.2012

⋆ Filipp, S.
Abelian and Non-Abelian Geometric Phases in Circuit Quantum Electrodynamics
Hong Kong Quantum Information Workshop, Hongkong, China, 18.06.2012

Filipp, S.
Simulating the influence of noise on the geometric phase in circuit QED
Workshop on Quantum Simulations, Universidad del Pais Vasco UPV/EHU, Bilbao, Spain, 22.10.2012

⋆ Filipp, S.
Geometric phases and gates in circuit QED
CEA Saclay, France, 11.12.2012

⋆ Fink, J.
Cavity QED with Microwave Photons and Superconducting Electronic Circuits
Kavli Nanoscience Institute, Caltech, Pasadena, USA, 17.01.2012

Frey, T.
Measurement of quantum dot properties with an on chip microwave resonator
ICPS, Zurich, Switzerland, 2.08.2012

Frey, T.
Measurement of quantum dot properties with an on chip microwave resonator
2nd NCCR QSIT evaluation, ETH Zurich, 29.11.2012

Frey, T.
Measurement of quantum dot properties with an on chip microwave resonator
ICPS, Zurich, Switzerland, 02.08.2012

Gvasaliya S.N.
Raman spectra and lattice dynamics of disordered complex perovskite $BaMg_{1/3}Ta_{2/3}O_3$
APS March Meeting 2012, Boston, USA, 27.02.2012

Häusermann, R.
From Organic Single Crystals to Solution Processed Thin-Films: Charge Transport and Trapping with Varying Degree of Order
International Conference on Flexible and Printed electronics, Tokyo, Japan, 06.09.2012

Hellmüller, S.
Optimization of sample and radio-frequency matching circuit design for time-resolved charge detection
31st International Conference on the Physics of Semiconductors, Zurich, Switzerland, 29.07.2012

Hellmüller, S.
Optimization of sample and radio-frequency matching circuit design for time-resolved charge detection
Workshop on Nonequilibrium Transport in Low-Dimensional Systems, Kfar Blum, Israel, 29.04.2012

Hüvonen, D.
Disorder a two-dimensional quantum spin liquid
APS March Meeting 2012, Boston, USA, 27.02.2012

Hüvonen, D.
Neutron diffraction and spectroscopy of bond disordered quantum magnets
Triple Axis Spectroscopy Workshop, Helmoltz Zentrum Berlin, Germany, 11.12.2012

⋆ Ihn, T.
Quantum Dot-Photon Coupling Using a Microwave Resonator
17th International Winterschool on New Developments in Solid State Physics, Mauterndorf, Austria, 13.02.2012

⋆ Ihn, T.
Charge sensing and real-time electron counting in quantum dots
APS March Meeting, Boston, USA, 01.03.2012

Ihn, T.
Recent results on counting individual electrons
Talk in Prof. Schönenberger's group, Basel, Switzerland, 14.05.2012

Ihn, T.
Multilevel transport in a three-terminal graphene quantum dot
Graphene Week, Delft, 05.06.2012

⋆ Ihn, T.
Dipole Coupling a Double Quantum Dot to a Microwave Resonator
Workshop on Quantum Transport in Correlated Systems, Seoul, Korea, 28.08.2012

⋆ Ihn, T.
Transport in graphene nanostructures - achievements and challenges
24th Conference of the EPS Condensed Matter Division (CMD-24), Edinburgh, UK, 4.09.2012

⋆ Ihn, T.
Nanostructures on ultra-clean two-dimensional electron gases
Int. Conference on The Science of Nanostructures: New Frontiers in the Physics of Quantum Dots, Chernogolovka, Russia, 11.09.2012

Ihn, T.
Graphene Nanostructures
Talk at the Paul Drude Institute, Berlin, Germany, 16.11.2012

Jacobsen, A.
Multilevel transport in a three-terminal graphene quantum dot
31st International Conference on the Physics of Semiconductors, Zurich, Switzerland, 29.07.2012

Jacobsen, A.
Multilevel transport in a three-terminal graphene quantum dot
Graphene week, Delft, 04.06.2012

⋆ v. Känel, H.
9. Int. Workshop ”Epitaxial semiconductors on patterned substrates and novel index surfaces” (ESPS-NIS), Eindhoven, The Netherlands, 07.05.2012

Komijani, Y.
Counting statistics of hole transport in a p-type GaAs quantum dot with dense spectra
31st International Conference on the Physics of Semiconductors, Zurich, Switzerland, 29.07.2012

Kozikov, A.
Imaging the Transmission of Nanostructures in an Ultra High-mobility GaAs heterostructure using Scanning Gate Microscopy
3rd International Workshop on Advanced Atomic Force Microscopy Techniques, Karlsruhe, Germany, 05.03.2012

Kozikov, A.
Probing quantum nature of electrons in backscattering through nanostructures in a GaAs heterostructure
31st International Conference on the Physics of Semiconductors, Zurich, Switzerland, 29.07.2012

Kraehenmann, T.
Conditional measurements of semiconductor quantum dots
QSIT Junior Meeting, Passugg, Switzerland, 03.06.2012

⋆ Lang, C.
Observation of Photon Blockade in Circuit QED using Correlation Function Measurement
Microkelvin Workshop 2012, Smolenice, Slovakia, 19.03.2012

Loretz, M..
A quantum sensor for radio frequency magnetic fields
2nd Annual Swiss MRFM meeting, Basel, Switzerland, 02.11.2012

Mattias, B.
Benchmarking a Teleportation Protocol realized in Circuit QED
APS March Meeting, Boston, USA, 27.02.2012

⋆ Mesot, J.
Forschung als Generationenvertrag
Workshop Lions-Club Baden, Baden, Switzerland, 21.02.2012

⋆ Mesot, J.
Beitrag des ETH-Bereichs zur Neustrukturierung des Energiesystems
Parlementarieranlass, Bern, Switzerland, 29.02.2012

⋆ Mesot, J.
Beiträge der akademischen Forschung zu innovativen Lösungen im Bereich Cleantech
Cleantec City, Bern, Switzerland, 15.03.2012

⋆ Mesot, J.
Introduction of PSI and related energy research
Meeting with Permanent Secretary of National Research and Development Singapore, Zurich, Switzerland, 28.06.2012

⋆ Mesot, J.
From Basic Energy Research to Applications
Workshop mit der Russischen Energie-Agentur (REA), Moscow, Russia, 09.07.2012

⋆ Mesot, J.
Strongly correlated materials research at PSI large-scale facilities: muons, neutrons and photons
UICr, The Sagamore XVII, Hokkaido, Japan, 15.07.2012

Michaels, Th.
Thermal fluctuations and domain walls in ultra-thin magnetic nanowires
XVII Convegno Nazionale di Fisica Statistica e dei Sistemi Complessi, Universita di Parma, Italy, 20.06.2012

⋆ Milan, A.
Visualizing electronic nematicity and Cooper pairing in iron-based superconductors
SFB 608 Colloquium, University of Cologne, Germany, 28.11.2012

⋆ Milan, A.
Visualizing electronic nematicity and Cooper pairing in iron-based superconductors
25th International Symposium on Superconductivity, Tokyo, Japan, 03.12.2012

Mlynek, J.
Observing Resonant Entanglement Dynamics in Circuit QED
APS March Meeting, Boston, USA, 28.02.2012

Moll, P.J.W.
Highly mobile in-plane vortex arrangement in SmFeAs(O,F) and LaFeAs(O,F)
APS March Meeting 2012, Boston, USA, 28.2.2012

⋆ Moll, P.J.W.
Slow Abrikosov- to fast moving Josephson vortex transition in iron-pnictide superconductors
Los Alamos Pulsed Field Facility (LANL-PFF) Colloquium, Los Alamos, NM, USA, 20.08.2012

Moll, P.J.W.
Mass renormalization in Fe-pnictides and related compounds
Planneralm, Austria, 13.02.2012

Moll, P.J.W.
Transition from slow Abrikosov- to fast moving Josephson-vortices in iron-pnictide superconductors
”Strongly Correlated Electron systems” (SCES) conference, Busan, Korea, 10.07.2012

⋆ Navaretti, P.
Nano-resonators for MRFM
Swiss MRFM meeting, Basel, Switzerland, 02.11.2012

Nichele, F.
P-type GaAs rings with strong spin-orbit interaction
2nd NCCR QSIT General Meeting, Arosa, Switzerland, 01.02.2012

Nichele, F.
Aharonov-Bohm oscillations in p-type GaAs rings with strong spin-orbit interaction: the role of sample-specific features
31st International Conference on the Physics of Semiconductors, Zurich, Switzerland, 29.07.2012

⋆ Ott, H.-R.
Field-induced magnetic order in frustrated and disordered S = 1/2 spin ladders
NCCR MaNEP workshop on magnetism and competing interactions in bulk material, Neuchatel, Switzerland, 10.01.2012

⋆ Ott, H.-R.
Goniometer for low-temperature NMR experiments
NCCR MaNEP forum meeting, Neuchatel, Switzerland, 11.01.2012

⋆ Ott, H.-R.
Exploring the potential of graphene, panelist in round-table discussion

Pascher, N.
Imaging electron transport through grapheme-and GaAS-based nano structures
2nd NCCR QSIT General Meeting, Arosa, Switzerland, 01.02.2012

Pascher, N.
Electrical transport through graphene nanoribbons characterized with static and movable gates
17th International Winterschool on New Developments in Solid State Physics, Mauterndorf, Austria, 12.02.2012

Pascher, N.
Scanning gate experiments on graphene nanoribbons
Meeting of the Swiss Physical Society, ETH Zurich, Switzerland, 21.06.2012

Pascher, N.
Scanning gate experiments on graphene nanoribbons
31st International Conference on the Physics of Semiconductors, Zurich, Switzerland, 29.07.2012

Pascher, N.
Scanning gate microscopy on graphene nanoribbons
QNET meeting, Helsinki, Finland, 11.1.2012

Pascher, N.
Scanning gate microscopy on graphene nanoribbons
Annual meeting of the Swiss Physical Society, ETH Zurich, 21.6.2012

Pechal, M.
Observing the geometric phase of a superconducting harmonic oscillator
APS March Meeting, Boston, USA, 28.02.2012

⋆ Pescia D.
Fundamental aspects of Near Tip Scanning Electron Microscopy
BITs 2nd Annual World Congress of Nano-S&T, Qingdao China, 26.10.2012

Pescia, D.
Was B. Franklin the first Nanophysicist?
SPG-Jahrestagung in Zürich, 21.06.2012

Ramsperger, U.
Near Field Emission Scanning Electron Microscopy
6th MPA Meeting, Alvor Portugal, 02.07.2012

Ramsperger, U.
Near Field Emission Scanning Electron Microscopy
BITs 2nd Annual World Congress of Nano-S&T, Qingdao China, 26.10.2012

Reichl, C.
How to observe the 5/2 Fractional Quantum Hall State - The Growth Sid
ETH-MPI Mini-Symposium on the ny = 5/2 State, MPI, Stuttgart, Germany, 19.4.2012

Reichl, C.
MBE-Growth of High-quality GaAs/AlGaAs-heterostructures to observe the 5/2 FQHS
QSIT evaluation Board, ETH Zürich, Germany, 29.11.2012

⋆ Roessler, C.
Quantum devices in ultra clean electron systems
NCCR QSIT, Arosa, Switzerland, 01.02.2012

⋆ Roessler, C.
Quantum devices in ultra clean electron systems
DPG Fruehjahrstagung, Berlin, Germany, 27.02.2012

⋆ Roessler, C.
Quantum devices in ultra clean electron systems
Meso-2012, Chernogolovka, Russia, 17.06.2012

Roessler, C.
Quantum devices in ultra clean electron systems
HMF 20, Chamonix, France, 22.07.2012

Roessler, C.
Quantum structures on ultraclean electron gases
17th International Winterschool on New Developments in Solid State Physics, Mauterndorf, Austria, 12.02.2012

⋆ Schiltz, G
Innovate Teaching! - Studierende mit einem Ideenwettbewerb an der Lehrinnovation beteiligen
Jahrestagung der Gesellschaft für Medien in der Wissenschaft (GMW 2012), Wien, 13.09.2012

⋆ Schiltz, G
Coupling local and central support structures: a model to ensure teaching support and quality assurance in research universities
9th ICED Conference 2012, Bangkok, Thailand, 24.07.2012

⋆ Schiltz, G
”Innovate Teaching”: A Student Competition
SWITCH eduhub days 2012, Murten, Switzerland, 02.04.2012

⋆ Schirhagl, R.
Magnetic Resonance Imaging and Microfluidics for Biomedical Applications
Groningen, Netherlands

⋆ Schirhagl, R.
Surface Imprinting - What else can be done?
Vienna, Austria, January 2012

Schmidiger, D.
The strong-leg spin ladder DIMPY
APS March Meeting 2012, Boston, USA, 28.2.2012

Schmidiger, D.
The strong-leg spin ladder DIMPY: Excitations in zero and applied magnetic fields
SPS Annual Meeting 2012, Zürich, Switzerland, 21.12.2012

⋆ Shiroka, T.
Competing orders in iron-based superconductors
3rd International Conference on Superconductivity and Magnetism, Istanbul, Turkey, 30.04.2012

⋆ Shiroka, T.
Basics of muon spectroscopy: Probing matter with elementary particles
Deutsche Forschungsgemeinschaft (DFG) School on Iron-Pnictides, Achatswies, Germany, 30.07.2012

⋆ Shiroka, T.
Investigating competing orders in Fe-based superconductors via $\mu$SR
Deutsche Forschungsgemeinschaft (DFG) School on Iron-Pnictides, Achatswies, Germany, 31.07.2012

Shiroka, T.
Influence of frustration, disorder and high magnetic fields in a S = 1/2 spin ladder
Joint European Magnetic Symposia (JEMS2012), Parma, Italy, 13.09.2012

Simonet, P.
Multilevel transport in a three-terminal graphene quantum dot
Meeting of the Swiss Physical Society, ETH Zurich, Switzerland, 21.06.2012

Simonet, P.
Graphene nanostructures on BN substrates
17th International Winterschool on New Developments in Solid State Physics, Mauterndorf, Austria, 12.02.2012

Steffen, L.
Experimental Monte Carlo Quantum Process Certification
APS March Meeting, Boston, USA, 27.02.2012

Tao, Y.
Fabrication of High Quality Single-Crystal Diamond Cantilevers
4th NanoMRI conference, Monte Verita, Ascona, Switzerland, 23.07.2012

⋆ Tao, Y.
Ultra-High Quality Factor Single-Crystal Diamond Nanoresonator
QSIT Lunch Seminar, ETH Zurich, Switzerland, 06.09.2012

Van Loo, A.
Cooperative Effects for Qubits in a Transmission Line: Experiment
APS March Meeting, Boston, USA, 28.02.2012

Varlet, A.
Improving graphene quality using Boron-Nitride substrates
International Physics School, Fundamentals of Nanoelectronics, Tenerife, Spain, 12.02.2012

Varlet, A.
Improving Graphene Quality using Boron-Nitride substrates
31st International Conference on the Physics of Semiconductors, Zurich, Switzerland, 29.07.2012

⋆ Vaterlaus, A
Wer hat Erfolg im Studium, basale Kompetenzen und Studierfähigkeit
Tagung der SMK, Universität Luzern, Luzern, 09.11.2012

⋆ Vaterlaus, A
Rastertunnelmikroskopie, moderne Physik an Mittelschulen
Jahrestagung der Schweizerischen Physikalischen Gesellschaft, Zürich, 22.06.2012

Vindigni, A.
Domain walls in ultrathin magnetic films and nanowires at finite temperatures
The 21st International Colloquium on Magnetic Films and Surfaces, Shanghai, 24.09.2012

Vindigni, A.
Magnetic domain walls in ultrathin films and magnetic nanowires at finite temperatures
Magnetic Single Nano-Object Workshop and School (M-SNOW 2012), Les Houches, 05.02.2012

⋆ Wachter, P.
Cu, Pu and Fe high $T_c$ superconductors: all the same mechanism
18th International Conference on Solid Compounds of Transition Elements (SCTE 2012), Lissabon, Portugal, 03.04.2012

⋆ Wagner, C
The Misconception-Concept Transition
WCPE Istanbul, Turkey, 05.06.2012

⋆ Wagner, C
Projekte im kompetenzorientierten Unterricht
Weiterbildungshalbtag Pädagogische Hochschule St. Gallen, Switzerland, 25.04.2012

⋆ Wagner, C
Kompetenzen, Kompetenzorientierung, Kompetenzkultur - Projektunterricht an der Kantonsschule Romanshorn
Pädagogische Hochschule Thurgau, Switzerland, 29.05.2012

⋆ Wagner, C
Interdisziplinäre Projekte der Matura KiK
Weiterbildungstag Kantonsschule Aarau 2012, Switzerland, 01.11.2012

⋆ Wallraff, A.
Overview of Activities at ETH Zurich
SOLID Topical Workshop on Josephson Junction Circuits: Coherence, Control, Correction, and Communication, Delft University of Technology, Delft, Netherlands, 16.01.2012

⋆ Wallraff, A.
Benchmarking a Teleportation Protocol with Superconducting Circuits
SOLID Topical Workshop on Josephson Junction Circuits: Coherence, Control, Correction, and Communication, Delft University of Technology, Delft, Netherlands, 17.01.2012

⋆ Wallraff, A.
Hybrid Quantum Systems using Microwave Frequency On-Chip Resonators as a Coupling Bus
SOLID Topical Workshop on Josephson Junction Circuits: Coherence, Control, Correction, and Communication, Delft University of Technology, Delft, Netherlands, 17.01.2012

⋆ Wallraff, A.
Quantum Optics with Superconducting Circuits: Exploring Propagating Microwave Photons
International Conference on Quantum Optics, Obergurgl, Tirol, Austria, 12.02.2012

Wallraff, A.
Circuit Quantum Electrodynamics with Semiconductor Quantum Dots
APS March Meeting, Boston, USA, 29.02.2012

⋆ Wallraff, A.
Quantum Information Processing with Superconducting Circuits
QISW 2012: Quantum Information Sciences Workshop, Oxford Department of Computer Science, Oxford, UK, 26.03.2012

⋆ Wallraff, A.
Exploring Quantum Properties of Propagating Microwaves with Superconducting Circuits
Continuous Variable Quantum Information Processing 2012 (CVQIP'12), Frederiksdal, Denmark, 27.04.2012

Wallraff, A.
Tomography and correlation function measurements of propagating microwave photons
Highlights of Quantum Optics, 500. Wilhelm und Else Heraeus-Seminar, Physikzentrum Bad Honnef, Germany, 07.05.2012

⋆ Wallraff, A.
Observation of Entanglement Between a Superconducting Qubit and Itinerant Microwave Photons
SPEC seminar talk, CEA Saclay, France, 06.07.2012

⋆ Wallraff, A.
Quantum Information Processing and Communication with Microwave Photons
Materials, Devices and Technologies for new Computation Paradigms, IBM Research - Zurich, Rüschlikon, Switzerland, 06.08.2012

⋆ Wallraff, A.
Quantum Optics with Superconducting Circuits
NIST Seminar, National Institute of Standards and Technology (NIST), Gaithersburg, MD, USA, 10.08.2012

⋆ Wallraff, A.
Exploring Microwave Photon Correlations in Experiments with Superconducting Circuits
Quantum Science, Gordon Research Conference on Stonehill College Easton, MA, USA 12.08.2012

⋆ Wallraff, A.
Exploring Microwave Photon Correlations in Experiments with Superconducting Circuits NIST/JILA
Seminar, JILA and National Institute of Standards and Technology (NIST), Boulder, CO, USA, 20.08.2012

⋆ Wallraff, A.
Exploring Quantum Properties of Propagating Microwave Photons
Summer School on Quantum and Non-Linear Optics (QNLO), Sandbjerg Estate, Denmark, 26.08.2012

⋆ Wallraff, A.
Exploring Quantum Properties of Propagating Microwave Photons
Summer School on Quantum and Non-Linear Optics (QNLO), Sandbjerg Estate, Denmark, 30.08.2012

⋆ Wallraff, A.
Sources and Signatures of Quantum Enhancements in Technology: Superconducting Circuits
Sources and signatures of quantum enhancements in technology, Royal Society International Scientific Seminar, Oxford, UK., 13.09.2012

⋆ Wallraff, A.
Observing Entanglement between Propagating Photons and Qubits in the Microwave Domain
Quantum Nanoscience Seminar, invited by Leo DiCarlo, TU Delft, Netherlands, 03.10.2012

⋆ Wallraff, A.
Quantum optics with superconducting circuits: Exploring propagating microwave photons
Quantum noise and measurement in engineered electronic systems, Max Planck Institute for the Physics of Complex Systems (MPIPKS) in Dresden, Germany, 08.10.2012

⋆ Wallraff, A.
Creating and Probing Quantum Microwave Fields in Superconducting Circuits
Workshop on Quantum Simulations, Universidad del Pais Vasco UPV/EHU, Bilbao, Spain, 22.10.2012

Wallraff, A.
Observing Entanglement between Propagating Microwave Photons and Qubits
CUA Seminar, Harvard University and MIT Center for Ultracold Atoms (CUA), Boston, MA, USA, 13.11.2012

⋆ Wallraff, A.
Circuit Quantum Electrodynamics with Semiconductor Double Quantum Dots
WE Heraeus Seminar, Hybrid Quantum Systems, Bad Honnef, Germany, 26.11.2012

⋆ Wallraff, A.
Exploring the Quantum Properties of Microwave Photons emitted from Solid State Circuits
Physics Colloquium, Faculty of Physics, Weizmann Institute of Science, Rehovot, Israel, 06.12.2012

⋆ Wallraff, A.
Realizing a Deterministic Teleportation Protocol in Superconducting Circuits
Topical Research Meetings on Physics: Quantum technologies: taking concepts through to implementations, Institute of Physics, London, UK, 17.12.2012

Wulf, E.
Field driven ordering in a frustrated spin ladder with bond randomness
DPG Frühjahrstagung, Berlin, Germany, 25.03.2012

Zanin, D.A.
Primary electron beam generation in Near-Field-Emission SEM
APS March Meeting 2012, Boston, USA, 28.02.2012

Zanin, D.A.
Progress in electron beam generation for Near Field-Emission Scanning Electron Microscopy
SPS Annual Meeting 2012, ETH Zürich, Switzerland, 21.06.2012

Zanin, D.A.
Near Field-Emission SEM: Primary electron beam generation and comparison with STM
25th IVNC, Jeju, Korea, 12.07.2012

Zheludev, A.
The perfect quantum spin ladder
Workshop on Synchrotron and Neutron Applications of High Magnetic Fields, SYNEMAG 2012 Grenoble, France, 17.10.2012

Zheludev, A.
Disorder in ordered quantum magnets
17th Sagamore conference on Charge, Spin and Momentum Densities, Hokkaido, Japan, 20.07.2012

Zheludev, A.
Disorder in ordered quantum magnets
Workshop on Mott Physics Beyond the Heisenberg Model, Lausanne, Switzerland, 06.06.2012

Zheludev, A.
The end of the quantum spin ladder problem
3rd International Conference on Superconductivity and Magnetism, (ICSM2012), Istanbul, Turkey, 29.04.2012

Zheludev, A.
The end of the quantum spin ladder problem
The 19th International Conference on Magnetism, Busan, Korea, 10.07.2012

⋆ Zheludev, A.
The quantum spin ladder
Seminar, ISSP, IFW-Dresden, Dresden, Germany, 14.12.2012

⋆ Zheludev, A.
It's half time in quantum magnetism
Seminar, Physics Dept., Brookhaven Natl Laboratory, Upton/NY, USA, 10.09.2012

⋆ Zheludev, A.
Disorder in quantum magnets
Seminar, Institute for Solid State Physics, University of Tokyo, Japan, 18.07.2012

⋆ Zheludev, A.
Magnetizing non-magnetic magnets
Colloquium, ENS de Lyon, France, 11.04.2012

Zhigadlo, N.
Improved high pressure flux growth, structural, and superconducting properties of LnFeAsO (Ln = Pr, Nd, Sm) single crystals
MaNEP Internal Workshop 2012 at Hotel Beaulac in Neuchatel, Switzerland, 12.01.2012

Zhigadlo, N.
Improved high pressure flux growth, structural, and superconducting properties of LnFeAsO (Ln = Pr, Nd, Sm) single crystals
18th International Conference on Solid Compounds of Transition Elements (SCTE-2012), Lisboa, Portugal, 31.03.2012

⋆ Zhigadlo, N.
High pressure crystal growth, structural, and superconducting properties of iron-based pnictides
Talk at the Institute of Low Temperature and Structure Research of Polish Academy of Sciences, Wroclaw, Poland,

07.06.2012

⋆ Zhigadlo, N.
Crystal growth and structure-property relationships in iron-based oxypnictide superconductors
”Phase Separation and Superstripes in High Temperature Superconductors and Related Materials” (Superstripes 2012), Erice-Sicily, Italy, 11.07.2012

## 12.2 Posters

Basset, J.
Using high frequencies to probe semiconducting nanostructures
NCCR QSIT Meeting, Arosa, Switzerland, 1.02.2012

Basset, J.
Coupling of a semiconductor double quantum dot to a microwave resonator
Workshop on Quantum Noise and Measurement in Engineered Electronic Systems, Dresden, Germany, 8.10.2012

Bischoff, D.
Etched Graphene Nanoribbons on Hexagonal Boron Nitride
Graphene Week, Delft, The Netherlands, 04.06.2012

Bischoff, D.
Etched Graphene Nanoribbons on Hexagonal Boron Nitride
Enrico Fermi School, Varenna, Italy, 19.06.2012

Bischoff, D.
Etched Graphene Nanoribbons on Hexagonal Boron Nitride
ICPS 2012, Zurich, 29.07.2012

Charpentier, C.
Molecular Beam Epitaxy of InAs/AlGaSb Heterostructures
ICPS 2012, Zürich, Switzerland, 31.7.2012

Chillal, S.
Magnetic properties of complex perovskites $PbFe_{1/2}Ta_{1/2}O_3$
Swiss Physical Society meeting, ETH Zürich, 21.06.2012

Choi, T.
Counting Statistics in an InAs Nanowire Quantum Dot with a vertically coupled Charge Detector
ICPS Conference, Zurich, Switzerland, 30.07.2012

Choi, T.
Counting Statistics in an InAs Nanowire Quantum Dot with a vertically coupled Charge Detector
Industry Day 2012, ETH Zurich, 7.9.2012

Dussaux, A.
Spin transfer induced magnetic vortex oscillations
4th Nano MRI Conference, Monte Verita, Ascona, Switzerland, 17.07.2012

Eichler, C.
Characterization of quantum microwave radiation and its entanglement with a superconducting qubit
Quantum noise and measurement in engineered electronic systems, Max Planck Institute for the Physics of Complex Systems (MPIPKS) in Dresden, Germany, 08.10.2012

Filipp, S.
Interfacing Microwave Photons with Rydberg Atoms on a Superconducting Chip
11th Int. Conference on Quantum Communication, Measurement and Computing, Vienna, Austria, 30.07.2012

Frey, T.
Measurement of quantum dot properties with an on chip microwave resonator
NI Summer School on "FPGA and High Performance Computing Technologies", Munich, Germany, 10.09.2012

Hellmueller, S.
Using High Frequencies to Probe Semiconducting Nanostructures
NCCR QSIT Meeting 2012, Arosa, Switzerland, 30.01.2013

Hellmueller, S.
Optimization of sample and radio-frequency matching circuit design for time-resolved charge detection
Workshop on Nonequilibrium Transport in Low-Dimensional Systems, Kfar Blum, Israel, 29.4.2012

Hüvonen, D.
Excitations in a bond disordered two-dimensional quantum spin liquid
SPS Annual Meeting 2012, Zürich, Switzerland, 21.06.2012

Kreiliger, T.
Towards a Ge X-Ray detector monolithically integrated on a Si CMOS chip
Nano-Tera Annual Plenary Meeting, Zurich, Switzerland, 24.04.2012

Lang, C.
Observation of Photon Blockade in Circuit QED using Correlation
NCCR-QSIT Meeting 2012, Arosa, Switzerland, 01.02.2012

Lorenz W. E. A.
Tunable spin ladder compound Cu(quinoxaline)($Cl_{1-x}Br_x$)$_2$
2012 Swiss Physical Society - MaNEP meeting, ETH Zürich, 22.06.2012

Loretz, M.
A quantum sensor for radio frequency magnetic fields
NCCR QSIT Evaluation, ETH Zurich, Switzerland, 28.11.2012

Loretz, M.
Spin lock decoupling of NV centers in diamond
NanoMRI conference, Monte Verita, Ascona, Switzerland, 22.07.2012

Michlmayr, T.
Demagnetization dynamics observed by spin-resolved ultrafast x-ray photoemission
ICM2012, Busan, South Korea, 12.07.2012

Mlynek, J.
Time resolved collective entanglement dynamics in circuit QED
NCCR-QSIT Meeting 2012, Arosa, Switzerland, 01.02.2012

Mlynek, J.
Time Resolved Collective Entanglement Dynamics in Cavity Quantum Electrodynamic
Highlights of Quantum Optics, 500. Wilhelm und Else Heraeus-Seminar, Physikzentrum Bad Honnef, Germany, 07.05.2012

Moll, P.J.W.
Mass renormalization in isostructural Ru- and Fe-pnictides
”Strongly Correlated Electron systems” (SCES) conference, Busan, Korea, 10.07.2012

Navaretti, P.
Nanoresonators for magnetic resonance force microscopy
NanoMRI conference, Monte Verita, Ascona, Switzerland, 23.07.2012

Navaretti, P.
Fabrication of Next-Generation Ultrasensitive Mechanical Resonators
NNCR QSIT site visit, ETH Zurich, Switzerland, 29.11.2012

Pascher, N.
Imaging electron transport through graphene and GaAs-based nanostructures
NCCR QSIT Meeting, Arosa, 1.2.2012

Pascher, N.
Electrical transport through graphene nanoribbons characterized with static and movable gates
Winter school, Mauterndorf, Austria, 12.2.2012

Pascher, N.
Scanning gate experiments on graphene nanoribbons
ICPS, Zurich, 29.7.2012

Pascher, N.
Scanning gate experiments on semiconductor quantum structures
NCCR QSIT evaluation, ETH Zurich, 29.11.2012

Pechal, M.
Geometric phases in superconducting circuits
NCCR-QSIT Meeting 2012, Arosa, Switzerland, 02.02.2012

Puebla-Hellmann, G.
Single molecule devices and photons
NCCR-QSIT Meeting 2012, Arosa, Switzerland, 01.02.2012

Reichl, C.
Advanced semiconductor materials for topological quantum computing
SPS, Zürich, Switzerland, 1.6.2012

Reichl, C.
Doping schemes in AlGaAs heterostructures: Correlations to fractional quantized Hall states
ICPS 2012, Zürich, 31.7.2012

Reim, K.
Rydberg atoms and superconducting qubits - a hybrid cavity QED interface
Quantum Systems and Technology, Centro Stefano Franscini, Monte Verita, Switzerland, 18.06.2012

Roessler, C.
Quantum devices in ultra clean electron systems
Winterschool 2012, Mauterndorf, Austria, 12.02.2013

Schiltz, G
Multimedia enhanced physics lecture experiments (ePhEx)
World Conference on Physics Education, Istanbul, Turkey, 03.07.2012

Schiltz, G
Don't bother about technology: Flashcards as a teaser for peer instruction
1st Conference on Peer Instruction, Beijing, China, 15.12.2012

Schirhagl, R.
Atom Probe Tomography of Diamond
5th Nano-MRI conference, Monte Verita, Ascona, Switzerland, 23.07.2012

Schirhagl, R.
Nano-MRI of Single Virus Particles
NCCR Structural Biology Meeting, Zurich, Switzerland, 29.08.2012

Schirhagl, R.
Single Quantum Emitter attached to an AFM-tip
NCCR QSIT Conference, Arosa, Switzerland, 01.02.2012

Shiroka, T.
MuSR studies of superconductivity in eutectically-grown mixed ruthenates
Joint European Magnetic Symposia (JEMS2012), Parma, Italy, 13.09.2012

Shiroka, T.
Disordered spin ladders at high magnetic fields: An NMR perspective
Strongly Correlated Electron Systems in High Magnetic Fields (SCEF 2012), Les Houches, France, 21.05.2012

Shiroka, T.
Frustration and disorder in a 1D spin ladder at high magnetic fields

Stammeier, M.
Rydberg atoms and superconducting qubits - a hybrid cavity QED interface
NI Summer School on "FPGA and High Performance Computing Technologies", Munich, Germany, 10.09.2012

Steffen, L.
Implementation of a Toffoli Gate with Superconducting Circuits
SOLID Topical Workshop on Josephson Junction Circuits: Coherence, Control, Correction, and Communication, Delft University of Technology, Delft, Netherlands, 16.01.2012

Steffen, L.
Efficient multi-qubit gates and quantum teleportation in circuit QED
NCCR-QSIT Meeting 2012, Arosa, Switzerland, 02.02.2012

Thede, M.
Ordering in weakly coupled random singlet spin chains
Swiss Physical Society, ETH Zürich, 21.06.2012

Thede, M.
Ordering in weakly coupled random singlet spin chains
Joint European Magnetic Symposia, Parma, Italy, 10.09.2012

Wüster, W.
Excitions and Trions in high-mobility 2DEGs
QSIT evaluation Board, ETH Zürich, Switzerland, 29.11.12

Willa, K.
Charge transport and trap DOS in solution processed TFT's: comparison with crystalline devices
Int. Symposium on Organic Transistors and Functional Interfaces OFET 2012, Princeton, USA, 27.10.2012

Wulf, E.
A frustrated spin ladder with bond randomness
SPG Jahrestagung, Zürich, Switzerland, 21.06.2012

Zhigadlo, N.
High pressure flux growth, structural and superconducting properties of LnFePnO (Ln: lanthanide, Pn: pnictogen) single crystals
International Conference "Materials and Mechanisms of Superconductivity" (M2S), Washington D.C., USA, 29.07.2012